Doctoraatsproefschrift nr. 914 aan de faculteit Bio-ingenieurswetenschappen van de K.U.Leuven

REVERSIBLE NO_X STORAGE OVER RU ZEOLITES

Sylvia SMEEKENS

Promotor:
Prof. J. A. Martens, K.U.Leuven

Leden van de examencommissie:
Prof. R. Schoonheydt, K.U.Leuven, Voorzitter
Prof. P. Jacobs, K.U.Leuven
Prof. C. E. A. Kirschhock, K.U.Leuven
Prof. M. Seo, K.U.Leuven
Prof. M. Tromp, University of Southampton
Prof. I. Vankelecom, K.U.Leuven

Proefschrift voorgedragen tot het
behalen van de graad
van Doctor in de
Bio-Ingenieurswetenschappen

Juni 2010

D/ 2010/11.109/32

Dankwoord

Vier en een half jaar onderzoek voeren, het is voorbij gevlogen. Tijd om een paar welgemeende dank u wels te zeggen:

Professor Martens, Johan, bedankt voor de kans die je mij gegeven hebt om een doctoraat te starten, bedankt voor de motiverende woorden als 'dat ruthenium' weer eens ambetant deed, ik kwam altijd terug met een glimlach uit uw bureau. Bedankt dat ik altijd op u kon rekenen. Ik heb zoveel van u geleerd en ik zou nog zoveel meer van u kunnen leren. En het is niet alleen deze intellectuele kant die ik wist te appreciëren, ook uw menselijke aanpak waardeerde ik enorm! Werken met vrouwen is nu eenmaal niet altijd even makkelijk. Ik denk dat ik ook voor heel 'team Martens' mag spreken als ik zeg dat de teambuilding avonden geweldig plezant waren! Bedankt voor alles!

Ook mijn juryleden, professoren Pierre Jacobs, Christine Kirschhock, Moniek Tromp, Maria Seo en Ivo Vankelecom, zou ik willen bedanken voor het nalezen van mijn doctoraat, voor de nuttige tips en de terechte kritische opmerkingen.
Christine, bedankt voor je grote bijdrage aan dit doctoraat. Het was niet altijd even gemakkelijk, maar hey, we hebben 'het beest' in de zeoliet uiteindelijk dan toch getemd!
Moniek, bedankt voor je hulp voor en na de EXAFS metingen. Bedankt voor de week Southampton waar ik onder uw toeziend oog (en de afleidende ogen van Ewa, Michal en Sergio) het fitten van EXAFS data mocht leren.
Maria, bedankt voor de TEM metingen.

Professor DeMarco, Mike, thank you very much for the Mössbauer experiments. I really enjoyed my stay at your home in Buffalo, walking the dogs every day, meeting the (famous) locals in the martini-bar,… oh! and getting a ticket at the Niagara Falls! You and Nancy are the most pleasant Americans I know.

Kristof, bedankt voor de NMR metingen en je deskundige uitleg! Kenneth Villani en David Habermacher, bedankt voor de bijdrage van experimentele data! Pieter en Bernard bedankt om mij te vergezellen naar Grenoble voor de EXAFS metingen en zo het werk wat te verlichten/verluchten.

En dan mijn 3 thesisstudenten: Wim, Steven H. en Nikki. Alle 3 totaal verschillend en toch 1 ding gemeen: genoeg prettig gestoord om in katalyse te komen werken! Bedankt voor jullie bijdrage, ik had me geen betere “slaafjes” kunnen inbeelden, ik heb er enorm van genoten!

Als mijne reactor in frut lag kon ik altijd rekenen op de eerste hulp van Johan, Stef en Werner. Bedankt heren voor jullie technische bijdrage en uitleg maar ook voor jullie geheel vrijwillige bijdrage aan de ‘vettige praat’ in de 02.96 en de grote interesse in mijn gemoedstoestand op maandagmorgen na een nederlaag van Racing Genk.

De dames van het secretariaat: Ines, Lieve P., Hilda, Inge, Birgit en Chris. Bedankt om mij te helpen met allerlei administratieve dingen en bedankt om er voor te zorgen dat ik steeds een zitje had in het vliegtuig en een bed in een hotel.
Lieve L. en Mia, bedankt voor jullie altijd vrolijke ‘goeiemorgen’ en de altijd vriendelijke glimlach. Hugo, bedankt voor de hulp bij de ICP metingen en om steeds mijn kapotte U-buizen vakkundig te laten maken.

Ons Gina, mijn grote steun en toeverlaat. Waar zal ik beginnen... . We hebben in ons klein bureauke toch nogal veel plezier gehad. Ook al zaten we een beetje verstopt in het labo, het was bij ons steeds de zoete inval. En ook al moesten we soms de harde hand bovenhalen om de rust te laten wederkeren, het hielp niet echt é. Gina, bedankt voor alles! Bedankt voor het luisterend oor, bedankt voor de babbels, bedankt voor de wijze raad, bedankt om het altijd voor me op te nemen als ik onderdrukt werd door enkele individuen (hun namen volgen nog), bedankt voor de cakejes, de soep, de koekskes,... . Ik heb Steven H. zo goed mogelijk proberen op te leiden, dus ik denk dat ik voor een volwaardige opvolger heb gezorgd. Maar toch, ik ga u missen!!!

En dan, de harde kern van Al-Katalyse: Slof en Bompi; hoofdzetel: de stoel van Gina. Ge zijt 2 sjarels èn kletswijven èn ramptoeristen! Maar toch, jullie aanwezigheid in Katalyse heeft het werk meer dan aangenaam gemaakt. En ik geef toe, van plagen en pesterijen kon ik ook wat van, dus we stonden altijd wel snel quitte. Ik zou jullie niet alleen willen bedanken voor de fijne momenten en de hulp op het lab, maar ook al de evenementen daarbuiten: de etentjes (we hebben er nog een paar te goed), de kotfeestjes (ge ging altijd met meer buiten dan dat ge oorspronkelijk bijhad), de cocktails, de kwisavonden (we zijn helaas nooit als eerste geëindigd), trouwfeesten (dansen met een piano), de badmintonavonden (‘dat was niet met opzet’) en de bijhorende cafetariabezoeken (wéél voetbal op dat scherm), de ... . Waar 1 van ons 3 was, waren de andere 2 ook meestal. Bedankt dames!

Ook de vroegere crew van de 03.73 zou ik willen bedanken om mij te adopteren tijdens hun bureau-activiteiten. Bedankt Ive, Bart, Bernard en Joris. Het was altijd plezant bij jullie, ook al moest ik dikwijls mijn plaats kennen!

Rob, Jan, Jasper, Michaël, Beau, Boris, Roosje: bedankt om me op tijd en stond mee te nemen naar de Alma, ook al was het soms met fysiek geweld. Bedankt voor de altijd appetijtelijke gespreksonderwerpen aan tafel, in de wandelgangen en op de badminton.

Leen, Lana en Anouschka, bedankt voor de 'vrouwenklap' en de vriendschap!
Sabina, zot zijn doet geen zeer!! Merci voor al de leuke momenten, de onnozele maar ook de serieuze babbels. En ja, op een dag zal de rust wederkeren en zullen de puzzelstukken op de juiste plaats vallen.

En dan zijn er nog een hele boel collega's die elk op hun manier de dagen op het COK onvergetelijk maakten. Ik denk daarbij aan Luc, Metin, Csaba, Pieter S., Filip, Kerlijne, Randy, Caroline, Sree, May, Kaz, ... en nog heel veel anderen! Bedankt allemaal!

Mijn vroegere kotgenoten mag ik ook zeker niet vergeten. Ik denk daarbij dan vooral aan Anouck, Lies en Nele. In de keuken (en ook daarbuiten) stond onze 'tetter' nooit stil. Onze jaren samen in Prins DeLigne waren onvergetelijk! Ik ben blij dat we elkaar nog niet uit het oog zijn verloren. Bedankt voor al dat plezier!

De vrienden van het thuisfront: Nele, Jolien, Tamara, Chris, Pieter-Jan & Katrien, Gert en Karl & Ann. Ja, ik ben nu eindelijk 'afgedoctoreerd'! Bedankt voor de afleiding gedurende de weekends!

Joris, bedankt om er altijd voor mij te zijn. Bedankt dat ik lief en leed met jou mocht delen.

Tot slot zou ik mijn familie willen bedanken. Paul en Tony, bedankt dat ik altijd op jullie een beroep mocht en kon doen.
Mama en papa, bedankt voor de goede zorgen tijdens het weekend, bedankt dat ik altijd op jullie kon rekenen, bedankt dat jullie er altijd voor me waren. Het was altijd een fijn thuiskomen. Bedankt!

Sylvia

ABSTRACT

Exhaust gases from internal combustion engines powering transportation vehicles are an important source of environmental pollution. Environmental concern led to the introduction of engines with improved fuel economy in combination with exhaust gas purification systems. The reduction of NO_x into harmless N_2 in exhaust gas from a lean burn combustion engine is an important scientific and technologic challenge. The challenge is to achieve chemical reduction in net oxidizing environment. The aim of the present research was to develop new NO_x adsorbents for implementation in future NO_x abatement concepts.

NO_x formation in an internal combustion proces depends on the engine type. Exhaust gas composition and temperature in conventional and lean-burn gasoline and diesel engines are different and necessitate the development of dedicated exhaust gas aftertreatment systems. The most promising aftertreatment technology for lean-burn gasoline and diesel engines is based on the concept of NO_x storage and reduction (NSR). This concept is already being commercialized and shows a high efficiency in reducing NO_x from exhaust of lean-burn gasoline and diesel engines. However, a main drawback of this technology is the drastic loss of NO_x storage capacity due to sulfur poisoning. Even low sulfur diesel and gasoline fuel contain organic sulfur compounds which after oxidation in the engine are converted into SO_x, poisioning catalysts and adsorbents. The barium based NO_x adsorbents, trapping NO_x as nitrate, show high adsorption capacity but are gradually poisoned through sulfate formation. Regeneration of such sulfur poisoned NO_x trap is possible through chemical reduction and sulfur dioxide formation, leading to a significant fuel penalty and implementation

of additional units coping with the hydrogen sulfide emission. This handicap of the present De-NO_x systems triggered research after sulfur tolerant NO_x adsorbents. Zeolites have been reported as possible NO_x adsorbents. Na-Y zeolite exhibits a reversible NO_x adsorption-desorption behavior and shows insensitivity to sulfur poisoning. Unfortunately, the Na-Y zeolite suffers from a low adsorption capacity and relatively slow NO_x desorption during regeneration. Moreover, the zeolite co-adsorbs NO and NO_2 from the exhaust gas to form N_2O_3 molecules, while NO_x in raw exhaust is composed of NO mainly.

In this work, an attempt was made to overcome these shortcomings of Na-Y zeolite. NO_x adsorption on Na-Y is critically dependent on NO into NO_2 oxidation. Out of a comparative study of noble metals, ruthenium was discovered to be a superior NO_x oxidation function in combination with Na-Y zeolite. The Ru/Na-Y exhibited a remarkable NO_x adsorption behavior characterized by trapping of pure NO and accelerated desorption kinetics. The Ru/Na-Y zeolite was characterized using EXAFS, ^{23}Na MAS NMR, ^{99}Ru Mössbauer spectroscopy, TEM, XRD and Rietveld refinement in combination with analysis of difference electron density charts. Extraneous ruthenium particles performed the oxidation of NO into NO_2. A small amount of Ru atoms in the framework cavities was found to undergo reversible oxidation and reduction causing dramatic sodium cation migration. During NO_x adsorption, oxidized ruthenium atoms are located inside the hexagonal prisms, pushing sodium cations into the supercages and generating NO_x adsorption sites in complex sodium-water networks. During regeneration in reducing conditions, ruthenium migrates to the sodalite cages, causing sodium cations to regain their positions on the framework and eliminating in this way the adsorption site for NO_x, resulting in a fast NO_x release. The presence of SO_2 in the gas composition had no influence on the NO_x adsorption-desorption nor on the NO_x adsorption capacity. However, the NO_x adsorption capacity of the Ru/Na-Y zeolite was still rather low compared to state-of-the-art barium-based NO_x adsorbents. The Na-Y zeolite was partially cation exchanged with barium. Ba,Na-Y zeolites were observed to have high NO_x adsorption capacity, but the material adsorbs selectively the NO_2 through nitrate formation and was difficult to regenerate. Introduction of a small amount of ruthenium in the Ba,Na-Y zeolite dramatically altered the behavior. The Ru/Ba,Na-Y adsorbent combined all of the desired properties: it traps NO as well as NO_2, can be

regenerated through pressure swing, and showed NO_x adsorption capacity comparable to state-of-the-art barium systems. A characterization of regenerated and NO_x saturated adsorbent using ^{23}Na MAS NMR, XRD and Rietveld refinement in combination with analysis of difference electron density charts revealed the unique role of ruthenium also in this material.

Like in Ru/Na-Y zeolite, NO_x was trapped as N_2O_3 in the supercages. The barium cations are located preferentially in the sodalite cages. The reduced number of Na^+ cations present in the supercages generates severely fragmented sodium-water networks. Ruthenium exerts the two functions already discovered in Ru/Na-Y, viz, NO oxidation over extraneous particles. Redox cycles of individual Ru atoms at specific positions trigger cation migrations and NO_x adsorption and release. This unique organization of cations improves the NO_x adsorption capacity as well as the reversibility of the adsorption process. The unique performances make Ru/Ba,Na-Y zeolite a potential candidates for future De-NO_x systems.

SAMENVATTING

Uitlaatgassen afkomstig uit interne verbrandingsmotoren van mobiele bronnen zoals het wegverkeer, het vliegverkeer en de scheepvaart vormen een belangrijke bron van milieuverontreiniging. De groeiende interesse in deze problematiek leidde tot de invoering van zuinige bezine- en dieselmotoren in combinatie met zuiveringssystemen voor uitlaatgassen. De reductie van NO_x tot onschadelijk N_2 in het zuurstofrijke uitlaatgas van zuinige benzine- en dieselmotoren vormt een belangrijke wetenschappelijke en technologische uitdaging. Het doel van dit onderzoek was de ontwikkeling van nieuwe NO_x adsorbenten voor toekomstige NO_x verwijderingsconcepten.

NO_x vorming in een intern verbrandingsproces is afhankelijk van het type motor. De samenstelling en de temperatuur van het uitlaatgas is verschillend voor conventionele, lean-burn benzine- en dieselmotoren waardoor de ontwikkeling van specifieke uitlaatgasnabehandelingssystemen noodzakelijk is.

De meest belovende techniek voor het verwijderen van NO_x uit uitlaatgassen van zuinige benzine- en dieselmotoren is via NO_x opslag in zuurstofrijke condities gevolgd door reductie in zuurstofarme periodes. Deze NO_x opslag en reductie (NSR) technologie is reeds gecommercialiseerd en vertoont een hoge efficiëntie. Een nadeel van deze technologie is echter het verlies aan NO_x opslagcapaciteit door zwavelvergiftiging. Zwavel arme diesel en benzine bevatten nog steeds kleine hoeveelheden organische zwavel. Deze worden in de motor geoxideerd tot SO_x en vergiftigen vervolgens het adsorbent en de katalysator. De op barium gebaseerde NO_x adsorbenten adsorberen NO_x als nitraten en vertonen een hoge opslagcapaciteit. Deze

capaciteit neemt echter geleidelijk af door zwavelvergifting. Regeneratie van deze vergiftigde NO_x adsorbenten is mogelijk met behulp van chemische reductie. Dit leidt weliswaar tot een verhoogd brandstofverbruik en de invoering van bijkomende systemen die het gevormde en stinkende H_2S bestrijden. Dit nadeel van de huidige De-NO_x systemen bracht een zoektocht naar zwaveltolerante NO_x opslagmaterialen teweeg. Zeolieten worden beschouwd als potentiële NO_x adsorbenten. Zeoliet Na-Y vertoont een reversibel NO_x adsorptie-desorptie gedrag en is daarenboven ongevoelig voor zwavelvergiftiging. Deze zeoliet adsorbeert NO_x als N_2O_3. Nadelen zijn echter de trage NO_x vrijgave tijdens regeneratie van het adsorbent, de lage NO_x adsorptiecapaciteit en de noodzaak aan gelijke molaire hoeveelheden NO en NO_2 in het uitlaatgasmengsel tijdens NO_x adsorptie.

In dit werk werd het potentieel van Na-Y zeoliet als NO_x adsorbent verder onderzocht en werd getracht de bovengenoemde tekortkomingen te overwinnen. Aangezien NO de hoofdcomponent is in het NO_x mengsel afkomstig uit verbrandingsgassen, is de adsorptie van NO_x in Na-Y zeoliet primair afhankelijk van de oxidatie van NO tot NO_2. In het eerste deel van dit werk werd een vergelijkende studie van edelmetalen uitgevoerd. Ruthenium vertoonde een superieure NO_x oxidatiefunctie na ionenuitwisseling in Na-Y. Daarnaast vertoonde deze Ru/Na-Y zeoliet een opmerkelijk adsorptie-desorptie gedrag: NO_x opslag gebeurde uit een gasflow die enkel NO als NO_x component bevatte en een versnelde NO_x vrijgave tijdens regeneratie werd geobserveerd. Karakterisatie van deze Ru/Na-Y zeoliet gebeurde via EXAFS, ^{23}Na MAS NMR, ^{99}Ru Mössbauer spectroscopie, TEM, XRD en Rietveld structuurverfijning. Ruthenium partikels aan de buitenkant van de zeoliet vervulden de rol van oxidatie functie. Een kleine hoeveelheid ruthenium atomen bevond zich in de kooien van de Na-Y zeoliet en kon afwisselend geoxideerd en gereduceerd worden. Dit oxidoreductie gedrag veroorzaakte een ingrijpende migratie van natrium kationen in de zeoliet. Tijdens NO_x adsorptie bevonden de geoxideerde rutheniumatomen zich in de hexagonale prisma's van de zeoliet. Hierdoor werden natrium kationen gedwongen om plaats te nemen in de superkooien waar ze een NO_x adsorptiesite genereerden in een complex natrium-water netwerk. Tijdens regeneratie in reducerende omstandigheden migreerden de ruthenium atomen naar de sodalietkooien. Dit gaf de natriumkationen in de superkooien de mogelijkheid om een positie in te nemen meer in de nabijheid van het zeolietrooster. Op deze manier werd

de NO_x adsorptiesite geëlimineerd wat resulteerde in een snelle NO_x vrijgave. Daarenboven had de aanwezigheid van SO_x in de gascompositie geen invloed op het NO_x adsorptie-desorptie gedrag noch op de NO_x adsorptiecapaciteit.

In vergelijking met state-of-the-art NO_x adsorbenten vertoonde de Ru/Na-Y zeoliet een eerder lage NO_x adsorptiecapaciteit. Door het inbrengen van barium in de zeoliet werd getracht deze NO_x adsorptiecapaciteit te verhogen. Van Ba,Na-Y zeolieten is immers geweten dat ze een hoge affiniteit vertonen voor NO_2. Rietveld structuurverfijning van een met NO_x verzadigde Ba,Na-Y zeoliet onthulde de aanwezigheid van planaire nitraat species in een stabiele positie tussen de natriumkationen in de superkooien. Regeneratie van dit met NO_x verzadigde adsorbent was enkel mogelijk door het te verwarmen tot op een temperatuur van 450 °C. Het inbrengen van een kleine hoeveelheid ruthenium in deze Ba,Na-Y zeoliet veroorzaakte een totaal ander NO_x adsorptiemechanisme. Deze Ru/Ba,Na-Y zeoliet combineerde alle gewenste eigenschappen: NO_x adsorptie uit een gasflow die enkel NO bevatte, snelle regeneratie tijdens zuurstofarme periodes en een NO_x adsorptiecapaciteit vergelijkbaar met de huidige op Ba gebaseerde adsorbenten. Karakterisatie van deze Ru/Ba,Na-Y zeoliet gebeurde met behulp van ^{23}Na MAS NMR, XRD en Rietveld structuurverfijning en bracht ook hier de unieke rol van ruthenium aan het licht. Net zoals in de Ru/Na-Y zeoliet gebeurde NO_x adsorptie als N_2O_3 in de superkooien van de zeoliet. Barium cationen positioneerde zich bij voorkeur in de sodalietkooien. De verminderde hoeveelheid natrium kationen in de eenheidscel van de Ru/Ba,Na-Y zeoliet veroorzaakte een sterk gefragmenteerd natrium-water netwerk. Dit gefragmenteerde netwerk vertoonde een verbeterde toegankelijkheid voor NO_x moleculen en een hogere flexibiliteit waardoor de NO_x adsorptiecapaciteit van de zeoliet aanzienlijk verhoogd werd. Ruthenium vervulde ook hier de 2 functies die eerder werden ontdekt in Ru/Na-Y: NO oxidatie door ruthenium partikels aan de buitenkant van de zeoliet en een oxidoreductie gedrag van ruthenium atomen in de zeoliet dewelke een ingrijpende migratie van natrium kationen in de zeoliet veroorzaakt en op deze manier NO_x adsorptiesites kan creëren en vernietingen. Deze unieke organisatie van kationen resulteerde in een reversibel NO_x adsorptieproces en een verhoogde adsorptiecapaciteit. Deze prestaties maken daaarom van Ru/Ba,Na-Y zeoliet een potentiële kandidaat voor toekomstige De-NO_x systemen.

.

LIST OF SYMBOLS AND ABBREVIATIONS

A/F ratio	Air/Fuel ratio
CEC	Cation Exchange Capacity
CLD	Chemiluminescence Detector
CO	Carbon monoxide
CO_2	Carbon dioxide
DDC	Detroit Diesel Corporation
EGO-sensor	Exhaust Gas Oxygen sensor
EGR	Exhaust Gas Recirculation
EPA	Environmental Protection Agency
ESRF	European Synchrotron Radiation Facility
EU	European Union
EXAFS	Extended X-ray Absorption Fine Structure
FAU	Faujasite
FER	Ferrierite
FWHM	Full Width at Half Maximum
HC	Hydrocarbons
HPA's	Heteropolyacids
HPW	12-tungstophosphoric acid hexahydrate ($H_3PW_{12}O_{40}.6H_2O$)
IC	Internal Combustion
ICP-AES	Inductively Coupled Plasma-Atomic Emission Spectroscopy

IZA	International Zeolite Association
MAS NMR	Magic Angle Spinning Nuclear Magnet Resonance
MFC	Mass Flow Controller
MOR	Mordenite
NEC	National Emission Ceilings
NO_x	Nitrogen Oxides
NSR	NO_x Storage and Reduction
ppm	parts per million
PM	Particulate Matter
SCR	Selective Catalytic Reduction
SNR	Selective NO_x Recirculation
SO_x	Sulfur Oxides
STP	Standard Temperature and Pressure
TEM	Transmission Electron Microscopy
TWC	Three-Way Catalyst
UV	Ultra-Violet
VHSV	Volumetric Hourly Space Velocity
VOC's	Volatile Organic Compunds
wt.-%	Weight percent
XRD	X-Ray Diffraction
λ	lambda factor

TABLE OF CONTENTS

CHAPTER 1

1. Literature Overview

1.1. Introduction

Historically, motor vehicles have contributed to the emission of air pollutants and especially of carbon monoxide (CO), carbon dioxide (CO_2), hydrocarbons (HC), nitrogen oxides (NO_x), sulfur oxides (SO_x) and fine particles (PM). The negative impact of these toxic and hazardous emissions on the environment, on human health and on the climate resulted in increasingly stringent emissions regulations for transportation vehicles. Greenhouse gas emissions, such as CO_2, are also under increasing scrutiny as is increasing engine fuel economy. One way to reduce CO_2 emissions, while coincidentally improving overall fuel economy, is through the use of lean-burn gasoline and diesel engines. Although CO_2 emissions are reduced and fuel economies improved using lean-burn gasoline and diesel engines, the legislation also requires significant reductions in NO_x and particulate matter emissions. Due to the excess of oxygen in lean-burn and diesel exhausts, NO_x reduction by conventional Three-Way Catalysts (TWC) requiring reducing conditions is difficult and new aftertreatment technologies are required. Besides selective catalytic reduction with hydrocarbons (HC-SCR) or ammonia (NH_3-SCR), a promising technology is based on the concept of NO_x storage and reduction (NSR).

In this chapter an overview is given of the NO_x formation during combustion processes, the concerns associated with these harmful emissions, the trends in regulations and the approaches developed for their reduction.

1.2. NO_x formation in internal combustion processes

NO_x molecules are formed in combustion processes and can be classified into 3 groups, depending on their origin: thermal, prompt and fuel NO_x.[1-8]

Thermal NO_x

Thermal nitrogen oxides are the most significant and are formed by heating oxygen and nitrogen in a flame or some other external heating.[2,5,8] Thermal NO_x formation mechanism begins when the temperature is about 1500 °C.[8] The reactions for producing NO and NO_2 in flames are:

$$N_2 + O_2 \leftrightarrow 2NO \quad (1)$$

$$NO + 0.5O_2 \leftrightarrow NO_2 \quad (2)$$

These reactions proceed by means of intermediate steps involving free radicals like $O^{\bullet}$, $N^{\bullet}$, $OH^{\bullet}$, $H^{\bullet}$ and hydrocarbons that have lost one or more hydrogens. These radicals exist only at high temperatures. The most widely accepted mechanism for the thermal NO formation reaction is that of Zeldovich and assumes that $O^{\bullet}$ radicals attack N_2 molecules by[6]

$$O^{\bullet} + N_2 \leftrightarrow NO + N^{\bullet} \quad (3)$$

and that $N^{\bullet}$ radicals can form NO by

$$N^{\bullet} + O_2 \leftrightarrow NO + O^{\bullet} \quad (4)$$

Reaction (3) has high activation energy due to the strong triple bond in the N_2 molecule. Therefore, this is the rate limiting step in the thermal NO_x formation.[8] This

reaction is sufficiently fast only at high temperatures. The critical period for thermal NO formation in an engine is when the temperatures of the burned gases are at a maximum.[2]

Because equations (1) and (2) are equilibrium reactions, they do not go to completion. Therefore it is possible to calculate the equilibrium concentrations of NO and NO_2. At 4% oxygen, representative of combustion gases of diesel engines, the NO and NO_2 concentrations at 1727 °C are respectively 3580 ppm and 2.5 ppm.[1] In combustion gases the NO_x concentration seldom reaches the concentration reflecting the thermodynamic equilibrium because of kinetic effects. In Figure 1 the calculated NO concentration in a gas containing 78% N_2 and 4% O_2 is represented as a function of time and temperature according to a simplified form of the Zeldovich mechanism. The gas heats from 20 °C to 1727 °C in 0.5 s with a linear temperature increase and then cools back to 20 °C with a linear temperature decrease. Upon cooling of the exhaust gas, the NO_x concentration is frozen at the level achieved at the highest temperatures. For kinetic reasons after cooling, the NO_x concentration remains at a level exceeded the composition at thermodynamic equilibrium.

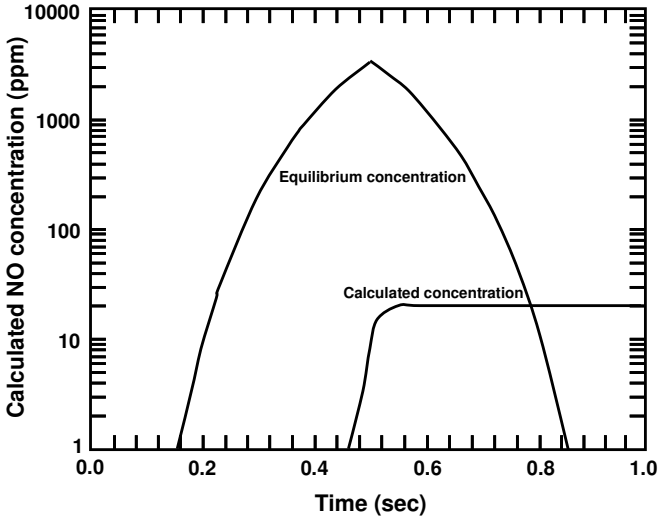

Figure 1: Calculated and equilibrium concentration of NO in a gas containing 78% N_2 and 4% O_2 as function of time according to the simplified form of the Zeldovich mechanism.[1]

Prompt NO_x (Fenimore NO)

During combustion of hydrocarbons, NO formation in the flame front is a much faster process than thermal NO_x formation.[7] This mechanism was first identified by Fenimore and involves carbon-bearing radicals ($CX^{\bullet}$) abundantly occurring in the oxidation zone of a flame.[1-3,7,8] These radicals are more reactive than the oxygen radical (Eq. (3)) and activate the triple bound of the N_2 molecule more easily. The most important of these reactions is:

$$CH^{\bullet} + N_2 \leftrightarrow HCN + N^{\bullet} \quad (5)$$

The $N^{\bullet}$ radical reacts with O_2 (Eq. (4)) leading to NO formation. The HCN formed in equation (5) enters the pool of amines and cyano compounds. They will react with NO producing N_2 or else when exposed to an oxygen rich environment produce NO. It is rather difficult to predict the prompt NO formation. There is no simple theoretical model. In flames below 1400°C, prompt NO_x formation dominates over thermal NO_x. Therefore, prompt NO_x is a low temperature phenomenon.

Fuel NO_x

Most gaseous and liquid fuels contain little organic nitrogen compounds. The contribution of that nitrogen to the total NO formation in the combustion products is minimal. N_2 from the intake air of the engine provides the majority of N atoms for NO_x formation. Fuel nitrogen typically is converted in the flame to HCN which then converts to NH or NH_2 under reducing conditions.[1-5,8] The NH and NH_2 can react with oxygen to produce NO and H_2O or they can react with NO to produce N_2 and H_2O.[8] The fraction of the fuel nitrogen that leaves the flame as NO is dependent of the NO/O_2 ratio in the flame zone. Keeping the oxygen content of the gases in the high-temperature part of the flame low is a means to lower the fraction of the fuel nitrogen converted to NO.

The formation and conversion processes of thermal, prompt and fuel NO are interlinked as shown in Figure 2.

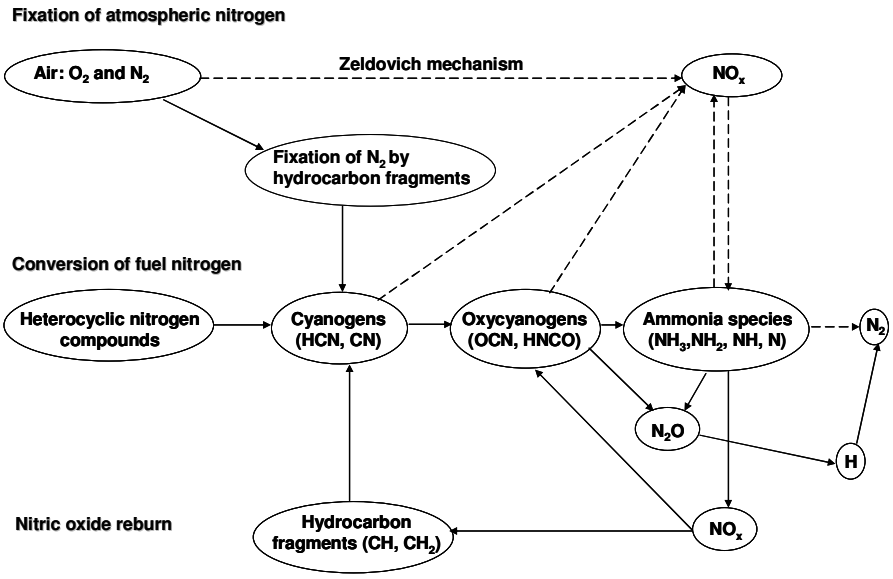

Figure 2: Nitrogen oxide formation during combustion. Reactions represented with a dotted arrow (-->) occur in oxidizing atmosphere. The other reactions (→) occur in reducing atmosphere.[1]

1.3. Influence of NO_x on the environment and human health

After World War II, people became more and more conscious of the influence of air pollutants such as NO_x on the environment as well as on human health. NO is a colorless gas that has some harmful effects on health. However, the toxicity is substantially lower than those of an equivalent amount of NO_2. The brown NO_2 gas is a respiratory irritant which can lead to a deterioration of the lung function, acute lung complaints and damage of the lung tissue. These harmful effects appear after short exposure to high concentrations or after long exposure to low concentrations.[9]

NO_2 is formed slowly via reaction of NO with O_2. However, in practice this reaction is insignificant unless the concentration of NO rises beyond 500 ppm, a condition which fortunately does nowhere occur in open air. Most of the NO_2 in the atmosphere is formed by reaction between NO and O_3:

$$NO + O_3 \rightarrow NO_2 + O_2 \qquad (6)$$

The formed NO_2 molecule is decomposed by a UV light photon to produce NO and an oxygen radical $O^{\bullet}$. That radical will react with O_2 to form O_3 which will then react with NO to form NO_2 and an O_2 molecule, in a cycle shown in Figure 3.[10]

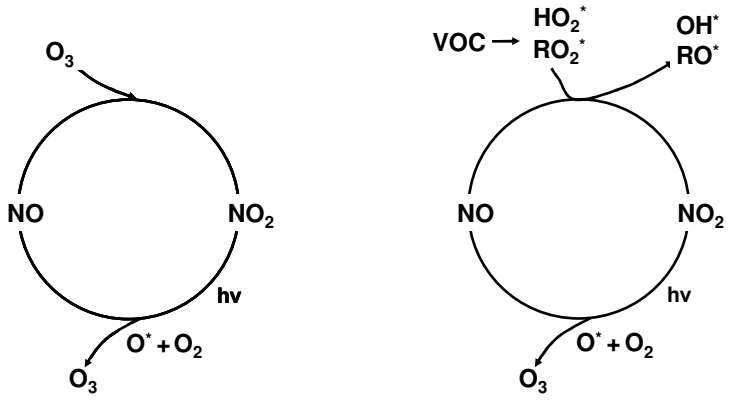

Figure 3: Schematics of the reactions involved in NO to NO_2 conversion and O_3 formation in absence (left) and presence (right) of volatile organic compounds.[10]

In the absence of volatile organic compounds (VOC's) this will lead to a dynamic equilibrium between NO, NO_2 and O_3 molecules that is dependent on the intensity of the solar radiation. However, when VOC's are present in the atmosphere, the chemistry is different.[10,11] VOC's molecules upon reaction with radicals from the air will be converted into alkylperoxy radicals ($RO_2^{\bullet}$) and hydroperoxy radicals ($HO_2^{\bullet}$) which will react with NO causing NO_2 formation without involving O_3. Ozone is formed through photochemical reaction of NO_2 with O_2. Thus, nitrogen oxides contribute to the formation and accumulation of O_3 which is one of the principal constituents of urban summer eye- and nose-irritating smog.[1,4,10,11] The overall reaction corresponds to:

$$NO + HC + O_2 + \text{sunlight} \rightarrow NO_2 + O_3 \qquad (7)$$

SO_x and NO_x are acid oxides that are responsible for degradation of materials. The gases can be carried on dust particles and smoke and deposited together with particulate matter.[11,12] These oxides are precursors of the acid rain.[1,13] Acid rain occurs when these gases react in the atmosphere with water and oxygen to form a solution of sulfuric acid and nitric acid in rain, fog and snow.

1.4. Vehicle emissions legislation

In 2007, the total NO_x emission in Flanders was around 177 925 ton.[14] Note that in quantification of the concentration NO_x is always considered as NO_2. Figure 4 represents the contribution of the different sectors in Flanders to NO_x emission. Motor vehicles are the biggest contributors. The traffic is responsible for 61% of the total NO_x emission. The other big NO_x polluters are the electricity producers (9%) and the ensemble of industrial activities (14%). This distribution of NO_x sources is representative for industrialized countries in general.[15]

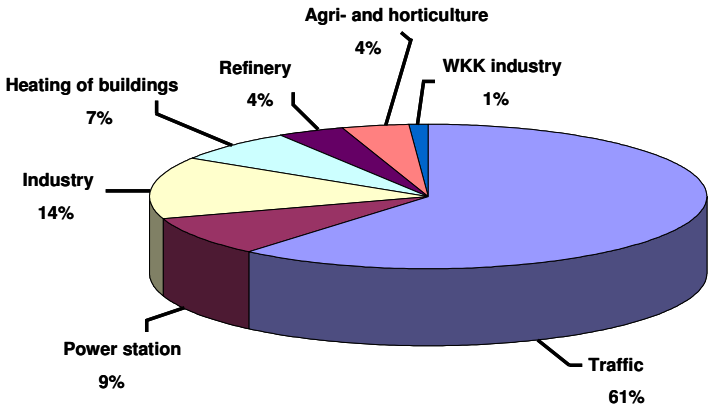

Figure 4: Contribution of the different sectors in Flanders to atmospheric NO_x emission in 2007.[14]

The presence of dense traffic explains why the largest NO_x emissions are present around the harbor of Antwerp, the arterial road between Antwerp and Brussels and some parts of the ring road around Brussels. The emission of ship engines adds to the pollution by road traffic. Although there is a significant reduction of the emissions in the last 20 years, Flanders and the Netherlands unfortunately remain hotspots of NO_x emission in Europe.

The EU is well aware of the NO_x pollution problem and took political action. Guideline 2001/81/EG, prescribed in 2001 and known as the NEC-guideline (NEC: national emission ceilings), imposes for every country in the European Union a restriction for total NO_x emission.[15,16] These regulations are very strict and have to be

obeyed by 2010. For Belgium, the maximum tolerated NO_x emission is 176 kton/year.[16]

Concerning human health, limiting values for exposure to NO_2 in ambient air were formulated in guideline 2008/50/EG, which also needs to be reached in 2010.[17] These regulations prescribe an hourly exposure limit value (max. 200 µg NO_2/m^3 which may not be exceeded more than 18 times each year) and a yearly exposure limit value (max. 40 µg NO_2/m^3).[15]

Because motor vehicles are the biggest NO_x polluters, specific norms were necessary. Introduction of emission control standards was started in the 1960's in the USA.[1,18] In Europe, the first regulations were introduced in the 1970's. Initially regulation was concerned with gasoline engines and related to CO and unburned hydrocarbons emission rather than NO_x. They were complemented in later regulations for diesel engines specifying limiting values for NO_x and particulate matter. Europe like other countries had lived a succession of each time more stringent regulations.[19] In 1992, the EURO standards were introduced for passenger cars, light-duty and heavy-duty trucks.[19] An overview of these standards for passenger cars and their implementation dates is given in Table 1. In other parts of the world, similar standards are set.[20]

Table 1: Emission standards for passenger cars (g/km).[15,19,20]

Compression Ignition (Diesel)

	Date	CO	HC	HC + NO_x	NO_x	PM
Euro 1	1992.07	2.72	-	0.97	-	0.14
Euro 2, IDI	1996.01	1.0	-	0.70	-	0.08
Euro 2, DI	1996.01	1.0	-	0.9	-	0.1
Euro 3	2000.01	0.64	-	0.56	0.50	0.05
Euro 4	2005.01	0.50	-	0.30	0.25	0.025
Euro 5	2009.09	0.50	-	0.23	0.18	0.005
Euro 6	2014.09	0.50	-	0.17	0.08	0.005

Positive Ignition (Gasoline)

	Date	CO	HC	HC + NO_x	NO_x	PM
Euro 1	1992.07	2.72	-	0.97	-	-
Euro 2	1996.01	2.2	-	0.50	-	-
Euro 3	2000.01	2.3	0.2	-	0.15	-
Euro 4	2005.01	1.0	0.1	-	0.08	-
Euro 5	2009.01	1.0	0.1	-	0.06	0.005
Euro 6	2014.09	1.0	0.1	-	0.06	0.005

1.5. Emissions from lean-burn gasoline and diesel engines

Before different emission control technologies are discussed, it is important to recall the difference between a conventional gasoline and a diesel or lean-burn gasoline engine.

Gasoline engines use a four stroke combustion cycle, also known as the Otto cycle, to convert gasoline into motion.[21-24] The four strokes are the intake, the compression, the combustion and the exhaust stroke. During the intake stroke, the intake valve opens and the piston moves down to let the engine take in a cylinder full of air and gasoline mixture. Then the piston moves back up to compress this air/fuel mixture. The compression makes the explosion later on more powerful. When the piston reaches the top of the stroke, the spark plug emits a spark to ignite the gasoline. The gasoline charge in the cylinder explodes driving the piston down. Once the piston is at the bottom of its stroke, the exhaust valve opens and the exhaust leaves the cylinder to go out the tailpipe. Now the engine is ready for the next cycle initiated by intake of another charge of air and gas.

The Otto cycle was invented in 1867 and the gasoline engine patented in 1876.[23] However, in its early stage, the gasoline engine was not very efficient and other major methods of transportation such as the steam engine fared poorly as well. Only about 10% of the fuel used in these types of engines actually efficiently moved the vehicle. The rest of the fuel simply produced useless heat. This inspired Rudolf Diesel to create an engine with a higher efficiency. By 1892 Diesel had obtained a patent for what we now call the diesel engine.[23] In theory, diesel and gasoline engines are quite similar. They are internal combustion engines, using a four stroke combustion cycle, designed to convert chemical energy available in the fuel into mechanical energy through a series of controlled explosions or combustions. The major difference between a diesel and a conventional gasoline engine is the way these explosions happen. In a gasoline engine, fuel is mixed with air, compressed by pistons and ignited by sparks from spark plugs, as discussed before. In a diesel engine, however, the air is compressed first and then the fuel is injected (direct injection).[23,25] Because air heats up when it is compressed, the fuel ignites.

Rudolf Diesel theorized that higher compression leads to higher efficiency and more power. A gasoline engine compresses at an air/fuel ratio of 8:1 to 12:1 while

a diesel engine compresses at a ratio of 14:1 to 40:1.[23] The compression of the air/fuel mixture in a gasoline engine limits the compression ratio of the engine. If it compresses the air too much, the air/fuel mixture spontaneously ignites and causes knocking.[22] Because this phenomenon causes excessive heat, knocking can damage the engine.

Mechanics are not the only difference between diesel and gasoline engines. There is also the issue of the fuel itself. When oil is refined at refineries, it can be separated into several kinds of fuel including gasoline, jet fuel, kerosene and diesel. When diesel fuel is compared with gasoline, it will be noticed that diesel is heavier and oilier. Diesel has a higher boiling point than gasoline and evaporates much more slowly. It has also a higher energy density. On average, 3.8 liter of diesel fuel contains approximately $155*10^6$ Joules while the same amount of gasoline contains only $132*10^6$ Joules. This combined with the improved efficiency of diesel engines explains why diesel engines get better mileage than equivalent gasoline engines.[23,26,27] However, not only the energy efficiency and the industrial costs have to be taken into account when evaluating fuel system technologies. The impact of polluting emissions like CO, NO_x, CO_2, SO_x and particulate matter are also an important issue. This well-to-wheel analysis is catching more and more attention now the search to new energy sources and alternative fuels has been started.[26,27]

Because most air pollutants are created and/or released in processes involving combustion, a rudimentary understanding of combustion will be presented here. The complete combustion of the air/fuel mixture in the combustion chamber can be represented as[1]

$$C_xH_y + (x + y/4)\ O_2 \rightarrow xCO_2 + (y/2)\ H_2O \qquad (8)$$

In addition, it will contain nitrogen and moisture that came in with the combustion air. In practice however, combustion to form H_2O and CO_2 is not a stoichiometric reaction which means that exhaust gases also contain unburned and partly burned hydrocarbons (HC) and carbon monoxide (CO).[1] In engines NO_x is formed out of N_2 and O_2 due to the high temperatures in the combustion chamber as mentioned earlier.[1-3] The concentrations of these pollutants in the exhaust gas are to a large extent determined by the air to fuel ratio in the combustion chamber. When gasoline is

represented with an average formula of C_8H_{17}, the stoichiometric A/F ratio can be calculated:

$$(A/F)_{stoichiometric} = [x + (y/4)]\ (32 + 3.76 * 28) / 12x + 1y \quad (9)$$

where 32 and 28 are the molecular weights of O_2 and N_2 (3.76 = 0.79/0.21) and 12 and 1 are the atomic weights of C and H respectively. Substituting x and y gives a $(A/F)_{stoichiometric}$ value of 14.88. This A/F ratio is often normalized and represented in literature as the excess air factor (λ-factor):

$$\lambda = (A/F)/(A/F)_{stoichiometric} \quad (10)$$

When running an engine under stoichiometric conditions, λ is 1. When $\lambda < 1$, there is not enough air to burn up all the fuel. The car is running under fuel-rich conditions. When $\lambda > 1$ however, the fuel supply is less than that which would react with the available air. This situation is called lean conditions. Figure 5 reproduces the emissions and fuel consumption for a typical IC engine in steady operation for different normalized air-fuel ratios.

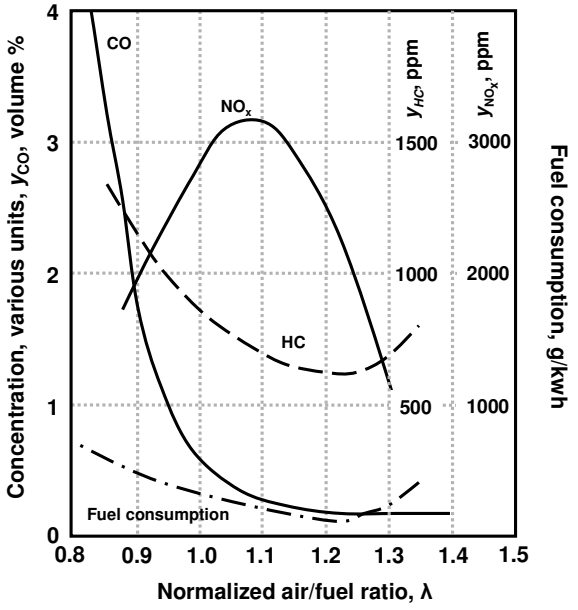

Figure 5: Emission and fuel consumption for a typical internal combustion engine in steady operation for different normalized air/fuel ratios.[1]

The fuel consumption is at its minimum and the emissions of HC and CO are at their lowest value when the engine is working under lean-burn conditions (excess air). The NO_x formation however is at its maximum because the temperature in the combustion chamber is the highest when only a small excess O_2 is present, favoring thermal NO formation.[1] Diesel and lean-burn engines operate under such conditions. It is a challenge to find the best compromise. When there is an air deficiency, the combustion will be not complete, resulting in HC and CO emission. The lower temperature in the combustion chamber however, minimizes thermal NO formation. Fuel consumption is unacceptably high. Stoichiometric combustion is the compromise that for decades was applied in the gasoline engine. Nowadays, driven by the lower fuel consumption target, the latest gasoline engines are run lean.[27] The excessive NO_x formation problem in the engine has became independent of the type of fuel.

1.6. Catalytic exhaust gas aftertreatment systems

There are always two approaches to abate NO_x emission from a vehicle with an internal combustion engine. The first one is minimize NO_x formation in the engine by modifying the combustion process. The key to preventing the formation of NO is lowering the temperature in the combustion chamber. The favorable effect of external recirculation of exhaust gas (EGR) involving cooling is based on this principle. The second approach is to eliminate the NO_x from the exhaust gas leaving the combustion chamber. Meeting the even more stringent emission standards at a minimum fuel penalty is a drive for innovation of engines as well as exhaust gas aftertreatment systems.

This thesis is related to NO_x elimination systems. The most popular practical approaches of NO_x elimination systems in exhaust gas aftertreatment are such as the Three-Way Catalyst (TWC), Selective Catalytic Reduction (SCR) and the NO_x Storage and Reduction (NSR) concept. There exist theoretical solutions such as Selective NO_x Recirculation (SNR) and Catalytic NO_x Decomposition which are not yet applied. All these approaches will be explained in the next section.

1.6.1. Non-practical applied approaches

1.6.1.1. Catalytic decomposition

Direct decomposition of NO is thermodynamically favorable at temperatures below 900°C (ΔG = -175 kJ/mol):[4,28,29]

$$NO \rightarrow \frac{1}{2} N_2 + \frac{1}{2} O_2 \quad (11)$$

This approach seems obvious and very attractive because no reducing agent is required and N_2 and O_2 are the only products formed. Owing to the electronic configuration of the NO molecule, this reaction is spin-forbidden. Many researchers have attempted to design a catalyst to lower the high activation energy of 300 kJ mol^{-1}. Iwamoto *et al.* discovered in 1986 the remarkable activity of Cu/ZSM-5 in NO decomposition.[30] The most important limitations of Cu/ZSM-5 for practical application are a too low activity (10 to 100 times on weight basis) and the poisoning of the activity by H_2O vapor and SO_2.[31,32]

Alternative cupper exchanged zeolites such as X, Y and mordenite are lower in activity than Cu/ZSM-5.[21] Much research has been done on modifications of Cu/ZSM-5 in order to increase the activity and stability and much research has been dedicated to the identification of the active sites in Cu/ZSM-5.[34-39] Although some interesting results were obtained, Goralski *et al.* concluded that lean-burn NO_x control for automotive application based on NO_x decomposition because of the slow reaction kinetics will be difficult to achieve.[40]

1.6.1.2. Selective NO_x Recirculation (SNR)

The SNR technique is a NO_x aftertreatment system for lean-burn gasoline and diesel engines comprising 2 exhaust lines, each containing a NO_x adsorber unit.[41-43] While one unit is adsorbing NO_x, the 2nd one is regenerated with air or exhaust gas, depending on the characteristics of the adsorber material, causing the release of NO_x. The desorbed NO_x is selective recirculated to the engine and decomposed in the

combustion process. Three types of materials containing Ba element have been shown to adsorb selectively NO_2 and store it as nitrate/nitrite species.[44] During regeneration upon increasing the temperature, decomposition of these nitrate/nitrite species takes place. The main advantages of this technique are the lack of formation of by-products or secondary emissions and the fact that the system works without the need to manage the engine operation.[43] The major obstacles for this technology to make it to practical realization are the NO_x adsorption capacity of the adsorbents and the long regeneration time required. The general problem of sulfur poisoning of the adsorbent is also encountered here.[42,44]

1.6.2. Practical applied approaches

1.6.2.1. Exhaust gas recirculation (EGR)

The exhaust gas recirculation system was introduced in the early 1970's. A fraction of the exhaust gas (max 20%) is recirculated to the engine and introduced together with intake air. This is a means to decrease the oxygen content and increase the water content of the intake air.[45-48] The main effect is the lowering of the peak combustion temperature resulting in an overall reduction of NO_x output. However, recirculation of NO_x to the engine reduces the power output of the engine and it requires extremely good control of the carburetion process and the air/fuel mixture distribution. During low engine speeds and warm-up, EGR is unnecessary because of the low temperature in the engine. Adding exhaust gases would adversely affect the engine operating efficiency. EGR is most effective during cruising and mid-range acceleration, when combustion temperatures are typically very high. The operation of EGR is very critical and presents a compromise between NO_x control and good engine performance. The Detroit Diesel Corporation (DDC) applied exhaust gas recirculation on its heavy-duty engines to meet the Environmental Protection Agency (EPA) 2007 emission standards.[49]

1.6.2.2. Non-Selective Catalytic Reduction (NSCR): Three-Way Catalyst (TWC)

The TWC catalyst simultaneous removes the three main air pollutants, viz. CO, HC and NO_x from the exhaust gases when an engine is running under stoichiometric conditions as shown in Figure 6.[50] Such stoichiometric combustion is encountered in gasoline engines.

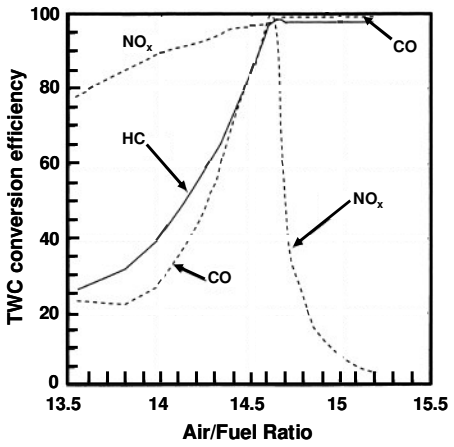

Figure 6: Typical TWC catalyst efficiency plot vs. air/fuel ratio in gasoline engines.[9]

The strategy is to remove first CO and HC by reaction with O_2. The remaining gas mixture with low oxygen content makes it possible to reduce NO via the reaction with the reductants (CO, HC).[51-54] The basic reactions for CO and HC in the TWC are oxidation reactions, generating CO_2 and H_2O while NO_x is reduced to N_2 and H_2O. Reaction stoichiometries are:

Oxidation:

$$C_xH_y + (x + y/4)\ O_2 \rightarrow xCO_2 + (y/2)\ H_2O \quad (12)$$

$$CO + ½\ O_2 \rightarrow CO_2 \quad (13)$$

$$CO + H_2O \rightarrow CO_2 + H_2 \quad (14)$$

Reduction:

$$NO\ (\text{or}\ NO_2) + CO \rightarrow ½\ N_2 + CO_2 \quad (15)$$

$$NO\ (or\ NO_2) + H_2 \rightarrow \tfrac{1}{2}\ N_2 + H_2O \qquad (16)$$

$$(2x + y/2)\ NO\ (or\ NO_2) + C_xH_y \rightarrow (x + y/4)\ N_2 + xCO_2 + y/2\ H_2O \qquad (17)$$

A typical Three-Way Catalyst is composed of mixtures of op to three metals comprising platinum, palladium and rhodium on an alumina washcoat supported by a ceramic honeycomb (Figure 7).[1,9,55-58]

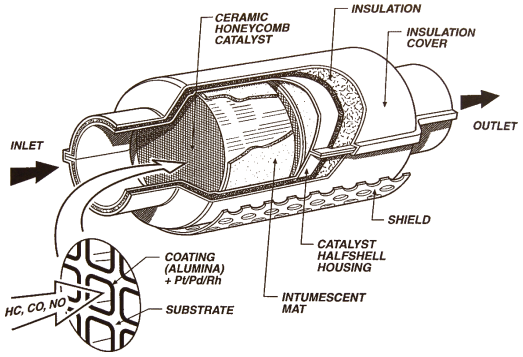

Figure 7: A typical TWC catalyst for the removal of CO, HC and NO_x from the exhaust gas of an internal combustion engine.[50]

Platinum and palladium catalyze the oxidation reactions, while rhodium is an excellent NO_x reduction catalyst.[51-58] The catalyst has a volume of about 1 liter and a noble metal content of about 1.5 g (0.1-0.15% of the total weight).

Because this TWC system is working under stoichiometric conditions, a perfect air/fuel control system is necessary. An exhaust gas oxygen sensor (EGO) often called lambda sensor is mounted upstream of the catalytic converter to monitor the O_2 content in the exhaust.[9,58] Having this information, the engine computer can adjust the concentration of O_2 in the exhaust by adjusting the air/fuel ratio, which allows effective removal of NO_x, HC and CO while the engine is running close to the stoichiometric point. The oxygen sensor is an oxygen conducting ZrO_2 crystal coated on both sides with a porous platinum film.

The alumina washcoat often is doped with cerium oxides. The cerium is oxidized to the oxidation state +4 under oxidative conditions and reduced to +3 under reducing conditions. Under rich conditions, CO is oxidized into CO_2 while ceria is reduced. Under lean conditions, Ce_2O_3 is oxidized into CeO_2 eliminating O_2 from the gas mixture. Thus the Ce(III)/Ce(IV) redox couple levels the lean or rich excesses that

temporarily may arise.[40,41] Especially in combination with Rh, the ceria enhances the NO reduction by CO.[59-62] Rh undergoes a strong deactivating interaction with alumina at temperatures of ca. 600 °C and above.[56] The incorporation of ceria inhibits these sintering reactions. Modifications in the adsorption properties of the metal as well as the creation of new catalytic active sites have also been suggested to explain the enhancement of catalytic behaviour of ceria modified catalysts in the reactions involved on TWC's.[59,62]

One of the shortcomings of a catalytic converter is that it does not work below a threshold temperature. Heat is provided by the exhaust gases. After cold start until the 'light off' temperature is reached, the catalyst is inactive. The cold start presents a situation with high emission of hydrocarbons and NO_x.[9,56,57] To accelerate heating, catalytic converters sometimes are positioned closer to the engine. However, this will reduce the lifetime of the converter exposed to very high temperatures once the engine is hot. Most cars have their converter positioned underfloor under the front passenger seat and use preheating to solve the problem of cold start.

Another potential problem is poisoning of the converter by sulfur. Sulfur, present in the fuel as organosulfur compounds are oxidized in the combustion to sulfur dioxide and subsequently on the catalyst to trioxide which can poison noble metal catalysts and also react with basic aluminum and cerium catalyst compounds that are converted to aluminum and cerium sulphates.[50,61,63-65] These sulfates can be reduced during rich conditions to hydrogen sulfide, having a smell. To reduce these H_2S emissions, trapping agents such as iron, nickel and manganese are added to the catalyst formulation.[9] The sulfur is trapped as sulfide species and released as odourless SO_2 under oxidizing conditions.

The TWC provides excellent results in conventional gasoline cars running under stoichiometric conditions. Therefore, since 1993 every new car with a conventional gasoline engine has been equipped with a TWC. However, due to the growing interest in improved fuel-efficient vehicles, lean-burn gasoline and diesel engines are becoming more and more popular. These engines work under higher air/fuel ratios, far away from stoichiometric point. In exhaust gas from lean burn gasoline and diesel engines, a TWC catalyzes oxidation of hydrocarbons and carbon monoxide but fails to reduce NO_x.efficiently.

1.6.2.3. Selective Catalytic Reduction (SCR)

The SCR technology is considered a proven technology to selectively reduce NO_x in flue gas from stationary sources.[66,67] The reductans most often used are CO, HC, NH_3 and urea (NH_2-CO-NH_2). More recently, SCR was introduced in automotive applications. Adaptation of the technology was needed to cope with volumetric limitation, operation under dynamic conditions, and widening of the catalytic activity window. Especially the realization of $DeNO_x$ activity at low temperatures constitutes a main challenge since the working conditions for mobile applications are typically much colder than in stationary installations. Several automobile manufacturers companies commercialized the NH_3-SCR technology for heavy-duty diesel vehicles.[68,69]

The NH_3-SCR process is based on the reaction between NO_x and NH_3 according to:

$$2NH_3 + 2NO + ½O_2 \rightarrow 2N_2 + 3H_2O \quad (18)$$

$$2NH_3 + NO + NO_2 \rightarrow 2N_2 + 3H_2O \quad (19)$$

These reactions are commonly referred to as the standard and the fast SCR reaction respectively.[70] Because the standard reaction contributes little at low temperatures compared to the fast SCR reaction and because NO represents typically 90% of the NO_x in exhaust gas, an NO oxidation catalyst or a non-thermal plasma technique was installed upstream of the SCR converter.[71-75] The first generation of commercial SCR catalysts for mobile applications were extruded honeycomb monoliths made of TiO_2 anatase carrier supporting the active V_2O_5 component and the WO_3 promoter.[76,77] Recent research is oriented towards hydrogen and iron exchanged zeolites. Zeolites had already been introduced for NO_x abatement in stationary installations as well.[78-82]

The major difficulties when using NH_3-SCR technology in the automotive application are the safe storage of NH_3, NH_3 corrosion and NH_3 slip. To overcome these difficulties aqueous urea solution is currently being used as an alternative reducing agent.[83] Urea is safer and will generate NH_3 by hydrolysis at about 200 °C according to:

$$CO(NH_2)_2 + H_2O \rightarrow CO_2 + 2NH_3 \quad (20)$$

When the urea solution is injected into the hot exhaust gas, the droplets are heated and water evaporates first. Urea molecules will then be thermally decomposed into NH_3 and HNCO. Isocyanic acid can readily undergo hydrolysis on the catalyst surface to produce one more molecule of NH_3.[84]

In presence of a suitable catalyst, the reduction of NO_x by NH_3 is reaching conversions of between 80-90%. On V_2O_5 catalysts the optimum operation temperature is 200-300 °C. At lower temperatures a Pt catalyst shows higher activity, while at temperatures exceeding 300 °C, the use of metal-exchanged zeolites is advised.[77,79]

The commercial name of the carbamide solution (32.5 wt.-%) used as reducing agent is called AdBlue.[85] This solution is provided via a storage tank in addition to the fuel tank. AdBlue consumption represents 1-3% of the diesel consumption. The volume of the tank is such that it only needs to be refilled during regular service and maintenance checkups. This technology is called BLUETEC® and registrated by DaimlerChrysler. Passenger cars equipped with this SCR technology were introduced into the market in the USA in 2006 and in Europe in 2008.[85]

Another principle strategy for performing SCR is trough in-situ generation of ammonia. Ammonia can be synthesized from NO_x and H_2 produced by the engine.[86] However, because the emitted H_2 in lean-burn gasoline and diesel engines is limited, it is difficult to produce sufficient ammonia to reduce all NO_x.

The amount of hydrocarbons in a typical exhaust gas composition is roughly 0.05-0.1% and should be sufficient to reduce all NO_x, provided that hydrocarbons are not oxidized.[87] Iwamoto *et al.* and Held *et al.* were the first to report SCR by hydrocarbons under lean conditions over a Cu/ZSM-5 catalyst.[88,89] This led to a comprehensive study of hydrocarbon-SCR over three different catalytic systems: metal oxides, ion-exchanged zeolites and noble metal catalysts. Metal oxide catalysts have attracted attention due to their high activity and hydrothermal stability. Elements like Co, Cu, Ag, Ga, In and Sn mostly supported on alumina were reported to be active for reduction of NO_x.[90-97]

Research on zeolite-based hydrocarbon SCR has been concerned with zeolite framework types of FER, MFI and MOR and introduced elements including Na, Ce, Pd, Pt, Sn, Ag, Fe, In, Ga, Mn and Co. An overview of catalysts, achievements and a

general reaction scheme were provided by Brosius *et al.* and Traa *et al.*.[98,99] The problem of oxidation of the hydrocarbons limiting their availability for NO_x reduction was circumvented by exploiting molecular sieving in zeolites.[98] A small pore zeolite was physical mixed with a large pore zeolite and each zeolite was loaded with a dedicated metal, e.g. Pt and Ag respectively. The pores of the first zeolite were too small for the hydrocarbons to reach the Pt oxidation sites, while NO and O_2 molecules had access. The actual HC-SCR reaction was catalyzed by silver in the large pore zeolite.

Recently plasma-assisted catalytic reduction of NO_x has been investigated.[75, 100-102] Na- and Ba-exchanged Y zeolite catalysts in particular have shown high activity when combined with plasma. The most important reactions in the plasma are the oxidation of NO to NO_2 and the partial oxidation of hydrocarbons. Over the catalyst bed, the NO_2 undergoes reduction by the partially oxidized hydrocarbons through conventional SCR chemistry. Plasma combined with a Na-Y catalyst achieved ca. 70% NO_x reduction in simulated lean-burn exhaust gas. Plasma assisted SCR for automotive application is a viable solution provided the energy input for the operation of the gas discharge does not present a major fuel penalty. Multistep plasma catalysis can be a solution but makes the design of the aftertreatment system more complex.[74]

Besides plasma, microwave radiation technology has attracted attention. The activity temperature window is shifted to lower temperatures and the deactivation of the catalyst by water is decreased by using microwaves.[103,104]

In contrast with metal oxide and zeolite-based catalysts, noble metal catalyst and especially the noble metals of the platinum group show excellent low-temperature activity. These metals show the best resistance against sulfur poisoning.[105-111] However, the narrow active temperature window of most catalyst is an obstacle in practical application as exhaust gas temperatures varies more widely depending on driving conditions. A cooperation of different catalysts is a possible solution and future developments will probably be focused on multiple-stage and multifunctional catalysts.

About the mechanism of HC-SCR, opinions are divided. Roughly all mechanisms can be classified into three groups. The first one comprises mechanisms where the catalytic decomposition of NO to N_2 and adsorbed oxygen is an important step. Hydrocarbons serve here as a scavenger which liberates the catalyst surface from adsorbed oxygen as demonstrated in equation (21) and (22).[112]

$$2NO \rightarrow N_2 + 2O_{ads} \quad (21)$$

$$HC + O_{ads} \rightarrow CO_x + H_2O \quad (22)$$

In the second interpretation the oxidation of NO to NO_2 is a crucial step. NO_2 acts as a strong oxidizing agent and will react further with the hydrocarbons to N_2 via organic intermediates according to equation (23) and (24).[112-117]

$$NO + ½\ O_2 \rightarrow NO_2 \quad (23)$$

$$NO_2 + HC \rightarrow N_2 + CO_x + H_2O \quad (24)$$

In the last interpretation, the reaction scheme starts with the partial oxidation of the hydrocarbons by oxygen or nitrogen oxides (Eq. (25)). In the next step, the oxygen- and/or nitrogen containing organic intermediates react with nitrogen oxides to N_2, CO_x and H_2O (Eq. (26)).[118-119]

$$HC + O_2 \text{ and/or } NO_x \rightarrow HC^{\bullet} \quad (25)$$

$$HC^{\bullet} + NO_x \rightarrow N_2 + CO_x + H_2O \quad (26)$$

1.6.2.4. NO_x Storage and Reduction (NSR) Catalysts

In NO_x storage and reduction catalytic technology, adsorption of NO_x and catalytic reduction are operated in a cycle. The concept originally was developed by Toyota.[120,121] NO_x is trapped on the adsorbent when the engine is running under lean conditions. When the adsorbent approaches its saturation level, the exhaust gas composition is made slightly reducing for a short period. This change of gas composition causes NO_x to be released from the adsorbent surface and to be chemically reduced to N_2 on the catalyst. The first reaction step in the NSR concept is the oxidation of NO to NO_2 which is catalyzed by platinum. Palladium and rhodium are much less active in NO oxidation compared to Pt. The NO_2 will react further and will be chemisorbed on the surface of the storage compound initially as nitrites and

eventually as nitrates. After a while, the engine is run rich for a short time. In absence of oxygen the stored NO_x is released by decomposition of the surface nitrite and nitrate and chemically reduced to N_2 by HC, H_2 and CO from the rich gas mixture over noble metal catalyst like platinum, palladium or rhodium (Figure 8).[122]

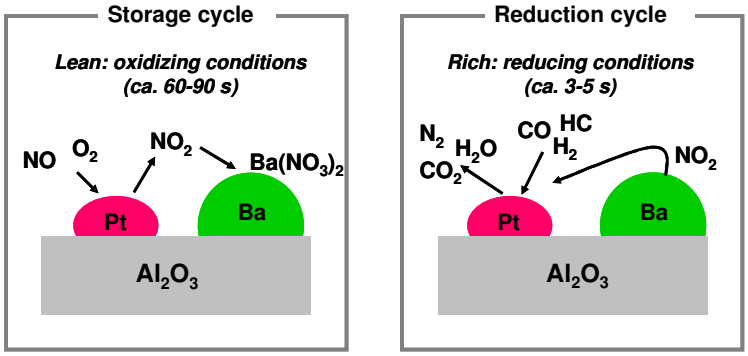

Figure 8: Schematic representation of the working principle of the NO_x storage and reduction catalyst.[30]

This NSR technology requires a material with strong basic properties to accomplish the storage of NO_2 and an oxidation and reduction catalyst to facilitate oxidation and reduction depending on conditions. A NO_x storage material is thus typically composed of at least one alkali or alkaline-earth metal and at least one precious-metal component, which are supported on a high surface area refractory oxide like Al_2O_3, ZrO_2, CeO_2, MgO or a mixture of these metal oxides.[123] The most commonly used formulation includes Pt and BaO supported on a γ-Al_2O_3. The Ba-loading varies mostly from 8 to 20%. The use of other alkali metals such as Na and K and alkaline-earth metals like Ca, Sr and Mg is less common.[124-127] The amount of precious metal generally used is in the range of 1-2 wt-%. The influence of the nature, the loading, the dispersion, the size and the morphology of the Pt particles on the catalytic activity still is a matter of discussion.[124] Using the NSR catalyst appears to be very effective to achieve high NO_x conversion. Storage of NO_x in real systems takes mostly 1-2 minutes and regeneration of the bed is finished within 3-5 seconds. In laboratory studies, the adsorbent regeneration phase of the cycle is much longer compared to those applied in real engines.

In Figure 9 an overview of the NO_x capacities of the current NO_x storage adsorbents, reported in literature, is given. The NO_x adsorption capacities are between 1 and 9 10^{-4} mol/g catalyst.

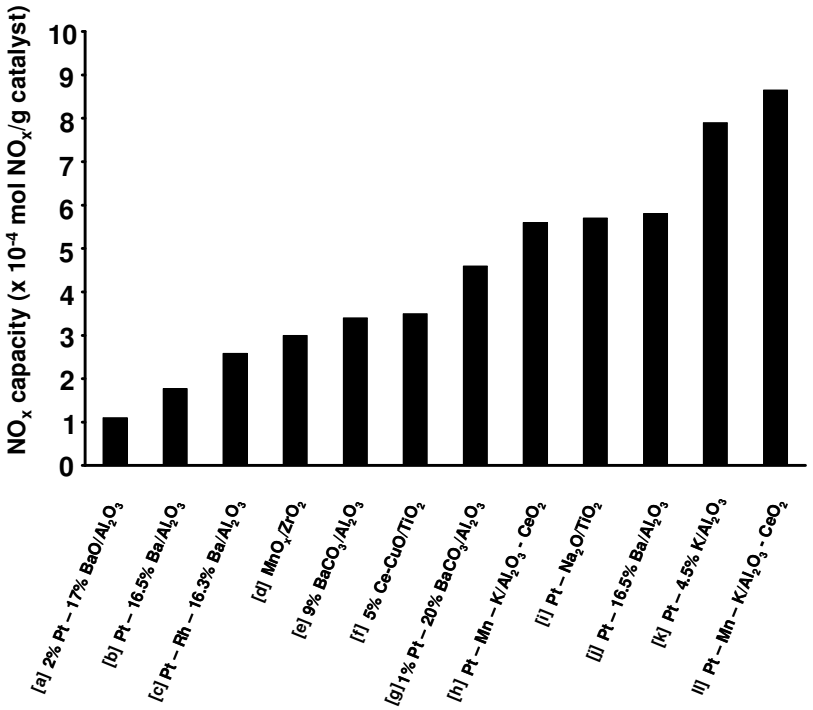

Figure 9: Overview of the NO_x adsorption capacities of the current NO_x storage adsorbents.[28,128,129] Feed gas comprised at least NO and O_2. The reaction temperatures were [a][130] 300 °C; [b][131] 200 °C; [c][132] 300 °C; [d][128] 200 °C; [e][133] 400 °C; [f][129] 200 °C; [g][134] 350 °C; [h][135] 200 °C; [i][136] 300 °C; [j][131] 300 °C; [k][137] 250 °C; [l][135] 300 °C.

In engine exhaust gas, a broad range of species are present in ppb to percent concentrations, like H_2O, CO_2 and different possible reductants (H_2, CO, C_3H_6).[50] These may influence the NSR catalyst in different ways and to different extents. They may e.g. alter the selectivity to N_2 formation under rich conditions and alter the NO_x storage capacity.[138] H_2 has been observed to be a better reductant compared to CO and hydrocarbons like C_3H_6.[139] H_2 can be produced on board via steam reforming, water gas shift reaction, partial oxidation or auto thermal reforming.

Although a lot of studies in the laboratory for reasons of convenience have been performed using gases that do not contain water, the presence of water in the gas

phase is known to influence the NO_x adsorption capacity by hindering the oxidation of NO to NO_2.[140,141] H_2O also has been shown to decrease the stability of nitrate species and prevents NO_x trapping on sites associated with Al_2O_3.[142,143] However, H_2O reduces the negative impact of CO_2 on NO_x adsorption by reducing the amount of carbonate at the surface via the equilibrium reaction (27). The hydroxide is less stable than the carbonate in relation to the surface NO_x species and can be displaced more easily by NO_x involved in nitrite or nitrate formation.[124]

$$BaCO_3 + H_2O \leftrightarrow Ba(OH)_2 + CO_2 \quad (27)$$

Nevertheless, a number of issues arise from implementation of this NSR concept such as the fuel penalty due to the rich excursions, sensitivity of the Ba adsorbent to fuel sulfur and difficult control under transient engine operation.

Diesel fuel and lubricating oil serve as the two major sources of sulfur in exhaust gas. The use of 2007 ultra-low sulfur fuel results in an exhaust gas containing less than 1 ppm sulfur. At this low level, the lubricating oil will become a significant contributor to sulfur in the exhaust, depending on lube oil sulfur content and the rate of oil consumption.[124]

During lean phase, sulfur is almost exclusively present in the form of SO_2 because most of the sulfur compounds are oxidized in the combustion process. These sulfur species compete with NO_x for the active sites and adsorb on the support and the storage component first as sulfates on the surface of Ba and later as bulk barium and aluminum sulfates. These bulk sulfates are stable during regeneration and permanently block Ba sites, leading to a gradual loss of NO_x adsorption capacity.[143] A second pathway of deactivation by sulfur species is linked with the rich conditions. Sulfides are formed on the Pt particles, blocking the metal surface and thus poison the catalytic reduction function of the metal. No such poisoning of Pt by sulfur was observed during the lean phase.[121,124,143] To enhance the durability of the NSR catalyst, Matsumoto *et al.* attempted to suppress the sulfur poisoning by enhancing sulfur desorption.[122,144] For this purpose a small amount of TiO_2 was added to the alumina catalyst. This reduced not only the number of sulfates stored but also suppressed the size of the sulfate particles without reducing the NO_x storage capacity. The smaller the size of the sulfate particles, the more easily they can be removed from the catalyst under reducing conditions.

Hydrogen has a much greater reducing power than CO and hydrocarbons. In-situ H_2 generation was achieved via steam reforming promoted by adding Rh/ZrO_2 to the washcoat.[122,139,144,145] Changing the structure of the ceramic monolithic substrate from square to hexagonal led not only to a lower SO_x deposit but also to a higher NO_x storage capacity.[122]

Heteropolyacids (HPA's) and particulary those of the Keggin type were presented as new NO_x adsorbents.[146-151] Among the HPA's family of compounds containing various metals, mainly 12-tungstophosphoric acid hexahydrate ($H_3PW_{12}O_{40}.6H_2O$, HPW) has shown significant NO_x adsorption capacity.[148] NO and NO_2 are adsorbed in equimolar ratio. Desorption is observed during cooling under humidified air.[149] During this regeneration an exchange of NO and NO_2 with the structural H_2O molecules of the secondary Keggin structure occurs.[149] Vaezzadeh *et al.* investigated the chemical reactions occurring on HPW and Pt doped HPW when a representative rich exhaust gas is used during regeneration.[150] The conclusion from that study was that high amounts of NO_x could be trapped during a lean phase but reduction of NO_x during a rich phase could not be achieved. This problem was solved by the development of a dual-bed system through which a reduction was accomplished by a TWC located downstream of the heteropolyacid adsorbent. TiO_2 and SnO_2 were evaluated as supports for HPW. Supporting the heteropolyacid systematically led to a partial loss of the HPW crystalline structure. The intact share of the HPW remained available for NO_x adsorption.[151] Heylen *et al.* investigated temperature swing co-adsorption of NO and NO_2 over Keggin and Wells-Dawson type heteropolyacids as pure compounds and supported on zeolite Y or encapsulated in the metal organic framework $Cu_3(BTC)_2$. That study revealed that the presence of crystal water in the heteropolyacids is a prerequisite for achieving NO_x adsorption.[152] While the adsorbed state of the NO_x molecules in heteropolyacids remained for long time a matter of discussion, strong evidence for formation of $H_2NO_2^+$ recently has been provided.[152]

Zeolites also have been reported as possible NO_x adsorbents. Important zeolite parameters were reported to be the zeolite structure, the Si/Al ratio and the nature of the cations compensating the negative charge of the framework. Earlier studies have not been performed under conditions relevant for exhaust gas aftertreatment, e.g. at ambient temperature and in absence of H_2O or O_2 or using pure NO_2.[153-159] The use of FAU zeolites as NO_x adsorbent under conditions more relevant to NSR was reported

by Monticelli *et al.* and Sultana *et al.*.[160-162] Monticelli *et al.* found a correlation between the type of exchanged alkali and alkaline-earth metal and the NO_x storage capacity (Ba-Y > Cs-Y > Na-Y > Li-Y).[160] NO_x was stored mainly as nitrate in the temperature window 100-177°C and in presence of H_2O according to following reactions:

$$3NO_2 + H_2O \rightarrow 2HNO_3 + NO \quad (28)$$

$$M^{n+}\text{-}nZ^- + nHNO_3 \rightarrow M(NO_3)_n + n\text{H-Z} \quad (29)$$

At these temperatures the zeolite showed affinity for NO_2 but not for NO. Regeneration of the adsorbent was done via temperature swing. Bentrup *et al.* confirmed storage of NO_x as nitrates in their study on MnO_2/Na-Y zeolite.[163] NO_x storage on Na-Y at 250 °C was performed by Sultana *et al.*.[161] A simultaneous adsorption of NO and NO_2 as N_2O_3, on a specific adsorption site in the supercages of zeolite Y was observed as illustrated in Figure 10. The adsorption site was created by water molecules interacting with the sodium cations to form a complex Na-H_2O network extending in the zeolite pores. The N_2O_3 molecule competes with 3 H_2O molecules in this complex Na-H_2O network according to:[161]

$$Na_x(H_2O)_y + NO + NO_2 \leftrightarrow Na_x(H_2O)_{y-3}(N_2O_3) + 3H_2O \quad (30)$$

Regeneration of the adsorbent bed was done in a pressure swing process by using hydrated, inert gas.[162,164]

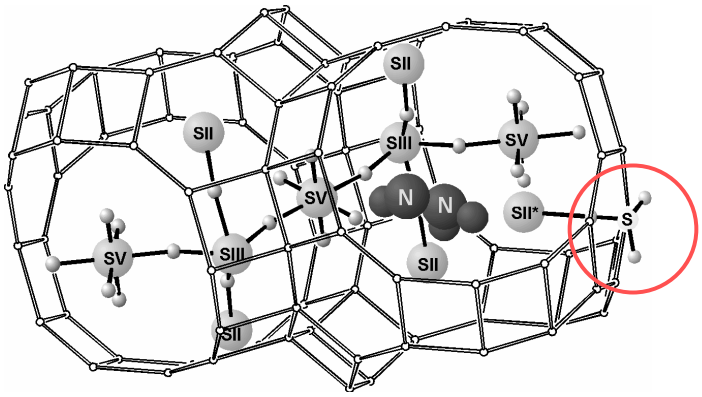

Figure 10: Illustration of the refined structure of NO_x adsorbed as N_2O_3 in Na-Y zeolite in the presence of water. Sodium cations are labeled SII, SII*, SIII and SV according to their position. The small spheres are oxygen atoms of water molecules that bridge sodium cations.[161]

In contrast with the commercial $Pt/Ba/Al_2O_3$ NSR catalyst, the Na-Y adsorbent was not sensitive to sulfur poisoning. Sulfurous acid molecules are formed at a specific site in the Na-Y zeolite cage, which is remote from the NO_x adsorption sites (Figure 10).[162,165] However, the Na-Y zeolite suffered from relatively slow NO_x desorption during regeneration and the necessity of having at least as much NO_2 as NO in the gas mixture for adsorption.

1.7. Aim of the thesis

From the literature study it is clear that NO_x adsorbents are gaining importance in NO_x elimination systems from exhaust gas emitted by vehicles with a lean burn internal combustion engine. The NSR concept is one of the technologies that made it to the market. Other concepts such as the SNR are awaiting the development of better NO_x adsorbents. In the past, considerable research efforts have already been investigated in comparative studies of NO_x adsorbents to be implemented in exhaust gas aftertreatment systems. While those studies were not always performed in relevant temperature windows and in presence of the relevant gases such as water, it can be concluded that the potential of many materials remains insufficiently explored. Another problem of most NO_x adsorbents is their sensitivity towards poisoning by SO_x, formed by combustion of organic sulphur compounds in the hydrocarbon fuel.

One of the intriguing adsorbent materials is the Na-Y zeolite, which was reported to be sulfur resistant and to show a unique co-adsorption of NO and NO_2 molecules in its supercages. The aim of the present study was to incorporate catalytic functions in the Na-Y zeolite and to enhance the NO_x adsorption capacity in order to overcome the shortcomings noticed in previous work. These shortcomings were the inactivity in gas mixtures lacking NO_2 and the slow NO_x desorption kinetics during regeneration beside the limited NO_x adsorption capacity. The research work was experimental and comprised performance testing of zeolite Y based NO_x adsorbents using synthetic gas mixtures mimicking exhaust gas and advanced characterization of adsorptive and catalytic functions using EXAFS, ^{23}Na MAS NMR, ^{99}Ru Mössbauer spectroscopy, TEM, XRD and Rietveld refinement in combination with analysis of difference electron density charts.

1.8. References

[1] de Nevers N., *Air pollution control engineering*, 2nd edition, McGraw-Hill Higher Education, **2000**, 586p.

[2] Miller J. A., Bowman C. T., *Prog. Energy Combust. Sci.* 15, **1989**, 287-338.

[3] Stoffel G., *Nitric oxide in a diesel engine: laser-based detection and interpretation*, Faculteit Natuurwetenschappen, wiskunden en informatica, Katholieke Universiteit Nijmegen, **1999**.

[4] Gómez-Garcia M. A., Pitchon V., Kiennemann A., *Environ. Int.* 31, **2005**, 445-467.

[5] Perry R. H., Green D. W., Maloney J. O., *Perry's chemical engineering handbook*, 6th edition, McGraw-Hill, **1985**.

[6] Zeldovich Y., *Acta Physicochimica USSR*, 21, **1946**, 577-628.

[7] Hayhurst A. N., Vince I. M., *Prog. Energy Combust. Sci.*, 6, **1980**, 35-51.

[8] Hill S. C., Douglas Smoot L., *Prog. Energy Combust. Sci.*, 26, **2000**, 417-458.

[9] Butler A., Nicholson R., *Life, death and nitric oxide*, RSC Paperbacks, **2003**, 154p.

[10] Atkinson R., *Atmos. Environ.*, 34, **2000**, 2063-2101.

[11] Jacob D. J., *Atmos. Environ.*, 34, **2000**, 2131-2159.

[12] Wesely M. L., Hicks B. B., *Atmos. Environ.*, 34, **2000**, 2261-2282.

[13] U.S. Environmental protection agency http://www.epa.gov/acidrain/, December **2009**.

[14] Anoniem, Lozingen in de lucht 1990-2007, Vlaamse Milieumaatschappij, Aalst, **2007**, 236p.

[15] Vestreng V., Ntziachristos L., Semb A., Reis S., Isaksen I. S. A., Tarrasón L., *Atmos. Chem. Phys.*, 9, **2009**, 1503-1520.

[16] Website Departement Leefmilieu, Natuur en energie, http://www.lne.be/themas/luchtverontreiniging/beleid/europees-beleid/nec-richtlijn, December **2009**.

[17] Website Vlaamse Milieumaatschappij, http://www.vmm.be/lucht/beleid-en-instrumenten.html/grens_en_richtwaarden.html/?searchterm=jaargrenswaarde%20NO , December **2009**.

[18] Shelef M., McCabe R. W., *Catal. Today* 62, **2000**, 35-50.

[19] Website Departement Leefmilieu, Natuur en Energie, http://www.lne.be/themas/milieu-en-mobiliteit/milieuvriendelijke-voertuigen/ecoscore-en-euronormen/euronormen-voor-voertuigen, December **2009**.

[20] Website Dieselnet, http://www.dieselnet.com/standards/eu/ld.php, December **2009**.

[21] Klaver P., *Katalysatoren*, VAM, Voorschoten, **1987,** 104p.

[22] Lumley J. L., *Engines, an introduction*, Cambridge University Press, **1999**, 248p.

[23] Stone R., *Introduction to Internal Combustion Engines*, Society of Automotive Engineers, Inc., **1997**, 574p.

[24] Thomson W., *Fundamentals of automotive engine balance*, Mechanical engineering publications LTD, Londen, **1978**, 96p.

[25] Zhao F., Lai M.-C., Harrington D. L., *Prog. Energy Combust. Sci.* 25, **1999**, 437-562.

[26] MacLean H. L., Lave L. B., *Prog. Energy Combust. Sci.* 29, **2003**, 1-69.

[27] Lapuerta M., Armas O., Rodríguez-Fernández J., *Prog. Energy Combust. Sci.* 34, **2008**, 198-223.

[28] Roy S., Baiker A., *Chem. Rev.* 109, **2009**, 4054-4091.

[29] Wu R. J., Yeh C. T., *Int. J. Chem. Kinet.* 28, **1996**, 89-94.

[30] Iwamoto M., Furukawa H., Mine Y., Uemura F., Mikuriya S., Kagawa S., *J. Chem. Soc. Chem. Commun*. **1986,** 1272-1273.

[31] Iwamoto M., Yahiro H., Shundo S., Yu Y., Mizuno N., *Appl. Catal.* 69, **1991**, L15-L19.

[32] Shelef M., *Chem. Rev.* 95, **1995**, 209-225.

[33] Iwamoto M., Yahiro H., Shundo S., Yu Y., Mizuno N., *Appl. Catal.* 69, **1991**, L15-L19.

[34] Kustova M. Y., Rasmussen S. B., Kustov A. L., Christensen C. A., *Appl. Catal. B* 67, **2006**, 60-67.

[35] Groothaert M. H., Lievens K., Leeman H. , Weckhuysen B. M., Schoonheydt R. A., *J. Catal.* 220, **2003**, 500-512.

[36] Pârvulescu V. I., Grange P., Delmon B., *Appl. Catal. B* 33, **2001**, 223-237.

[37] Dědeček J., Bortnovsky O., Vondrová A., Wichterlová B., *J. Catal.* 200, **2001**, 160-170.

[38] Groothaert M. H., van Bokhoven J. A., Battiston A. A., Weckhuysen B. M., Schoonheydt R. A., *J. Am. Chem. Soc.* 125, **2003**, 7629-7640.

[39] Groothaert M. H., Lievens K., van Bokhoven J. A., Battiston A. A., Weckhuysen B. M., Pierloot K., Schoonheydt R. A., *ChemPhysChem* 4, **2003**, 626-630.

[40] Goralski C. T., Schneider W. F., *Appl. Catal. B* 37, **2002**, 263-277.

[41] Krutzsch B., Wenninger G., Weibel M., Stapf P., Funk A., Webster D. E., Chaize E., Kasemo B., Martens J., Kienneman A., *SAE Paper*, **1998**, 982592.

[42] Method and apparatus for reducing nitrogen oxides in the exhaust gas of an internal combustion engine. Patent 5457958, United States, 17 October **1995** (Daimler-Benz AG).

[43] Hodjati S., Vaezzadeh K., Petit C., Pitchon V., Kiennemann A., *Catal. Today* 59,**2000**, 323-334.

[44] Chaize E., Webster D. E., Krutzsch B., Wenninger G., Weibel M., Hodjati Sh., Petit C., Pitchon V., Kiennemann A., Loenders R., Monticelli O., Jacobs P. A., Martens J. A., Kasemo B., *SAE paper*, **1998**, 982593.

[45] Zheng M., Reader G. T., Hawley J. G., *Energ. Convers. Manage.* 45, **2004**, 883-900.

[46] Hountalas D. T., Mavropoulos G. C., Binder K. B., *Energy* 33, **2008**, 272-283.

[47] Kouremenos D. A., Hountalas D. T., Binder K. B., Raab A., Schnabel M. H., *SAE 2001-01-0199*, **2001**.

[48] Lazaro J. L., Garcia-Bernad J. L., Perez C., Galindo J., Climent H., Arnau F. J., *SAE 2002-01-1154*, **2002**.

[49] Website Detroit Diesel Corporation, http://www.detroitdiesel.com/emissions/epa2007/aftertreatment.aspx, December **2009**.

[50] Heck R. M., Farrauto R. J., Catalytic air pollution control, 2nd Ed., John Wiley&Sons, New York, **2002**, 391p.

[51] Evans J., Tromp M., *J. Phys.: Condens. Matter* 20, **2008**, 184020.

[52] Granger P., Dujardin C., Paul J.-F., Leclercq G., *J. Mol. Catal. A* 228, **2005**, 241-253.

[53] Roy S., Hegde M. S., Madras G., *Appl. Energy* 86, **2009**, 2283-2297.

[54] Dent A. J., Evans J., Fiddy S. G., Jyoti, Newton M. A., Tromp M., *Angew. Chem. Int. Ed.* 46, **2007**, 5356-5358.

[55] Taylor K. C., *Catal. Rev.-Sci. Eng.* 35, **1993**, 457-481.

[56] Gandhi H. S., Graham G. W., McCabe R. W., *J. Catal.* 216, **2003**, 433-442.

[57] Kašpar J., Fornasiero P., Hickey N., *Catal. Today* 77, **2003**, 419-449.

[58] Twigg M. V., *Appl. Catal. B* 70, **2007**, 2-15.

[59] Lööf P., Kasemo B., Andersson S., Fredstad A., *J. Catal.* 130, **1991**, 181-191.

[60] Oh S. H., *J. Catal.* 124, **1990**, 477-487.

[61] Rabinowitz H. N., Tauster S. J., Heck R. M., *Appl. Catal. A* 212, **2001**, 215-222.

[62] Lecomte J. J., Granger P., Leclercq L., Lamonier J. F., Aboukaïs A., Leclercq G., *Colloids and Surfaces A : Physicochem. Eng. Aspects* 158, **1999**, 241-247.

[63] Waqif M., Bazin P., Saur O., Lavalley J. C., Blanchard G., Touret O., *Appl. Catal. B* 11, **1997**, 193-205.

[64] Rabinowitz H. N., Tauster S. J., Heck R. M., *Appl. Catal. A* 212, **2001**, 215-222.

[65] Gandhi H. S., Shelef M., *Appl. Catal.* 77, **1991**, 175-186.

[66] Heck R. M., Catal. Today 53, **1999**, 519-523.

[67] Forzatti P., *Appl. Catal. A* 222, **2001**, 221-236.

[68] Mercedes-Benz website, http://www.mercedes-benz.be, November **2009**.

[69] Volvo website, http://www.volvo.com/group/scr/en-gb/home.htm, November **2009**.

[70] Kato A., Matsuda S., Kamo T., Nakajima F., Kuroda H., Narita T., *J. Phys. Chem.* 85, **1981**, 4099-4102.

[71] Koebel M., Elsener M., Madia G., *Ind. Eng. Chem. Res.* 40, **2001**, 52-59.

[72] Koebel M., Madia G., Raimondi F., Wokaun A., *J. Catal.* 209, **2002**, 159-165.

[73] Madia G., Koebel M., Elsener M., Wokaun A., *Ind. Eng. Chem. Res.* 41, **2002**, 3512-3517.

[74] Kwak J. H., Szanyi J., Peden C. H. F., *J. Catal.* 220, **2003**, 291-298.

[75] Kwak J. H., Szanyi J., Peden C. H. F. *Catal. Today* 89, **2004**, 135-141.

[76] Ciardelli C., Nova I., Tronconi E., Chatterjee D., Bandl-Konrad B., Weibel M., Krutzsch B., *Appl. Catal. B* 70, **2007**, 80-90.

[77] Ciardelli C., Nova I., Tronconi E., Chatterjee D., Burkhardt T., Weibel M., *Chem. Eng. Sci.* 62, **2007**, 5001-5006.

[78] Grossale A., Nova I., Tronconi E., *Catal. Today* 136, **2008**, 18-27.

[79] Kröcher O., Devadas M., Elsener M., Wokaun A., Söger N., Pfeifer M., Demel Y., Mussmann L., *Appl. Catal. B* 66, **2006**, 208-216.

[80] Sjövall H., Olsson L., Fridell E., Blint R. J., *Appl. Catal. B* 64, **2006**, 180-188.

[81] Yeom Y. H., Henao J., Li M. J., Sachtler W. M. H., Weitz E., *J. Catal.* 231, **2005**, 181-193.

[82] Long R. Q., Yang R. T., *J. Catal.* 207, **2002**, 224-231.

[83] Yim S. D., Kim S. J., Baik J. H., Nam I.-S., *Ind. Eng. Chem. Res.* 43, **2004**, 4856-4863.

[84] Kleemann M., Elsener M., Koebel M., Wokaun A., *Ind. Eng. Chem. Res.* 39, **2000**, 4120-4126.

[85] Mercedes-Benz website, http://www.mercedes-benz.nl/content/netherlands/mpc/mpc_netherlands_website/nl/home_mpc/truck_home/home/trucks/acris/bluetec.html, November **2009**.

[86] Macleod M., Lambert R. M., *Chem. Commun.*, **2003**, 1300-1301.

[87] Kung H. H., Kung M. C., *Catal. Today* 30, **1996**, 5-14.

[88] Iwamoto M., Yahiro H., Shin H. K., Watanabe M., Guo J., Konno M., Chikahisa T., Murayama T., *Appl. Catal. B* 5, **1994**, L1-L5.

[89] Held W., König A., Richtel T., Puppe L., *SAE 900496*, **1990**.

[90] Shimizu K., Satsuma A., Hattori T., *Appl. Catal. B* 16, **1998**, 319-326.

[91] Seker E., Cavataio J., Gulari E., Lorpongpaiboom P., Osuwan S., *Appl. Catal. A* 183, **1999**, 493-505.

[92] Bethke K. A., Kung H. H., *J. Catal.* 172, **1997**, 93-102.

[93] Maunula T., Ahola J., Hamada H., *Appl. Catal. B* 26, **2000**, 173-192.

[94] Park P. W., Ragle C. S., Boyer C. L., Balmer M. L., Engelhard M., *J. Catal.* 210, **2002**, 97-105.

[95] Park P. W., Kung H. H., Kim D. W., Kung M. C., *J. Catal.* 184, **1999**, 440-454.

[96] Yan J., Kung M. C., Sachtler W. M. H., Kung H. H., *J. Catal.* 172, **1997**, 178-186.

[97] Kung M. C., Park P. W., Kim D. W., Kung H. H., *J. Catal.* 181, **1999**, 1-5.

[98] Brosius R., Martens J. A., *Top. Catal.* 28, **2004**, 119-130.

[99] Traa Y., Burger B., Weitkamp J., *Micropor. Mesopor. Mater.* 30, **1999**, 3-41.

[100] Miessner H., Francke K., Rudolph R., *Appl. Catal B* 36, **2002**, 53-62.

[101] Yoon S., Panov A. G., Tonkyn R. G., Ebeling A. C., Barlow S. E., Balmer M. L., *Catal. Today* 72, **2002**, 243-250.

[102] Yoon S., Panov A. G., Tonkyn R. G., Ebeling A. C., Barlow S. E., Balmer M. L., *Catal. Today* 72, **2002**, 251-257.

[103] Wang X., Zhang T., Xu C., Sun X., Liang D., Lin L., *Chem Comm.*, **2000**, 279-280.

[104] Tang J., Zhang T., Ma L., Li N., Liang D., Lin L., *Top. Catal.* 22, **2003**, 59-63.

[105] Obuchi A., Ohi A., Nakamura M., Ogata A., Mizuno K., Ohuchi H., *Appl. Catal. B* 2, **1993**, 71-80.

[106] Fujii R., Seki M., Shinoda J., Okazaki N., Tada A., *Chem. Lett.* 32, **2003**, 764-765.

[107] Efthimiadis E. A., Lionta G. D., Christoforou S. C., Vasalos I. A., *Catal. Today* 40**, 1998**, 15-26.

[108] Burch R., Millington P. J., *Catal. Today* 29, **1996**, 37-42.

[109] Burch R., Ottery D., *Appl. Catal. B* 13, **1997**, 105-111.

[110] Ingelsten H. H., Skoglundh M., Fridell E., *Appl. Catal. B* 41, **2003**, 287-300.

[111] García-Cortés J. M., Pérez-Ramírez J., Illán-Gómez M. J., Lecea C. S.-M. D., *Catal. Comm.* 4, **2003**, 165-170.

[112] Burch R., Millington P. J., Walker A. P., *Appl. Catal. B* 4, **1994**, 65-94.

[113] Yokoyama C., Misono M., *Catal. Today* 22, **1994**, 95-72.

[114] Kikuchi E., Ogura M., Terasaki I., Goto Y., *J. Catal.* 161, **1996**, 465-470.

[115] Descorme C., Gélin P., Primet M., Lécuyer C., *Catal. Lett.* 41, **1996**, 133-138.

[116] Miller J. T., Glusker E., Peddi R., Zheng T., Regal-buto J. R., *Catal. Lett.* 51, **1998**, 15-22.

[117] Yan J.-Y., Kung H. H., Sachtler W. M. H., Kung M. C., *J. Catal*. 175, **1998**, 294-301.

[118] Li Y., Slager T. L., Armor J. N., *J. Catal.* 150, **1994**, 388-399.

[119] Lobree L. J., Aylor A. W., Reimer J. A., Bell A. T., *J. Catal.* 169, **1997**, 188-193.

[120] Matsumoto S., *Catal. Today* 29, **1996**, 43-45.

[121] Takahashi N., Shinjoh H., Iijima T., Suzuki T., Yamazaki K., Yokota K., Suzuki H., Miyoshi N., Matsumoto S., Tanizawa T., Tanaka T., Tateishi S., Kasahara K., *Catal. Today* 27, **1996**, 63-69.

[122] Matsumoto S., *Catal. Today* 90, **2004**, 183-190.

[123] Muraki H., Zhang G., *Catal. Today* 63, **2000**, 337-345.

[124] Epling W. S., Campbell L. E., Yezerets A., Currier N. W., Parks J. E., *Catal. Rev.-Sci. Eng.* 46, **2004,** 163-245.

[125] Lesage T., Saussey J., Malo S., Hervieu M., Hedouin C., Blanchard G., Daturi M., *Appl. Catal. B* 72, **2007**, 166-177.

[126] Lesage T., Verrier C., Bazin P., Saussey J., Malo S., Hedouin C., Blanchard G., Daturi M., *Top. Catal.* 30-31, **2004**, 31-36.

[127] Verrier C., Kwak J. H., Kim D. H., Peden C. H. F., Szanyi J., *Catal. Today* 136, **2008**, 121-127.

[128] Eguchi K., Watabe M., Ogata S., Arai H., *J. Catal.* 158, **1996**, 420-426.

[129] Li W. B., Yang R. T., Krist K., Regalbuto J. R., *Energy&Fuels* 11, **1997**, 428-432.

[130] Mahzoul H., Brilhac J. F., Gilot P., *Appl. Catal B* 20, **1999**, 47-55.

[131] Lietti L., Forzatti P., Nova I., Tronconi E., *J. Catal.* 204, **2001**, 175-191.

[132] Lesage T., Verrier C., Bazin P., Saussey J., Daturi M., *Phys. Chem. Chem. Phys.* 5, **2003**, 4435-4440.

[133] Rodrigues F., Juste L., Potvin C., Tempere J. F., Blanchard G., Djega-Mariadassou G., *Catal. Lett.* 72, **2001**, 59-64.

[134] Nova I., Castoldi L., Lietti L., Tronconi E., Forzatti P., Prinetto F., Ghiotti G., *J. Catal.* 222, **2004**, 377-388.

[135] Lesage T., Saussey J., Malo S., Hervieu M., Hedouin C., Blanchard G., Daturi M., *Appl. Catal. B* 72, **2007**, 166-177.

[136] Yamamoto K., Kikuchi R., Takeguchi T., Eguchi K., *J. Catal.* 238, **2006**, 449-457.

[137] Toops T. J., Smith D. B., Epling W. S., Parks J. E., Patridge W. P., *Appl. Catal. B* 58, **2005**, 255-264.

[138] Abdulhamid H., Fridell E., Skoglundh M., *Appl. Catal. B* 62, **2006**, 319-328.

[139] Poulston S., Rajaram R. R., *Catal. Today* 81, **2003**, 603-610.

[140] Scholz C. M. L., Gangwal V. R., de Croon M., Schouten J. C., *Appl. Catal. B* 71, **2007**, 143-150.

[141] Olsson L., Abul-Milh M., Karlsson H., Jobson E., Thormahlen P., Hinz A., *Top. Catal.* 30-31, **2004**, 85-90.

[142] Lindholm L., Currier N. W., Fridell E., Yezerets A., Olsson L., *Appl. Catal. B* 75, **2007**, 78-87.

[143] Sedlmair Ch., Seshan K., Jentys A., Lercher J. A., *Catal. Today* 75, **2002**, 413-419.

[144] Matsumoto S., Ikeda Y., Suzuki H., Ogai M., Miyoshi N., *Appl. Catal. B* 25, **2000**, 115-124.

[145] Hirata H., Hachisuka I., Ikeda Y., Tsuji S., Matsumoto S., *Top. Catal.* 16/17, **2001**, 145-149.

[146] Yang R. T., Chen N., *Ind. Eng. Chem. Res.* 33, **1994**, 825-831.

[147] Bélanger R., Moffat J. B., *J. Catal.* 152, **1995**, 179-188.

[148] Hodjati S., Petit C., Pitchon V., Kiennemann A., *J. Catal.* 197, **2001**, 324-334.

[149] Hodjati S., Vaezzadeh K., Petit C., Pitchon V., Kiennemann A., *Top. Catal.* 16/17, **2001**, 151-155.

[150] Vaezzadeh K., Petit C., Pitchon V., *Catal. Today* 73, **2002**, 297-305.

[151] Thomas S., Vaezzadeh K., Pitchon V., *Top. Catal.* 30/31, **2004**, 207-213.

[152] Heylen S., Smeekens S., C. Kirschock, Parac-Vogt T., Martens J.A. *Energy Environ. Sci.* ***2010*** *DOI: 10.1039/b923160a*.

[153] Despres J., Koebel M., Kröcher O., Elsener M., Wokaun A., *Micropor. Mesopor. Mater.* 58, **2003**, 175-183.

[154] Arai H., Machida M., *Catal. Today* 22, **1994**, 97-109.

[155] Zhang W. H., Yahiro H., Mizuno N., Izumi J., Iwamoto M., *Langmuir* 9, **1993**, 2337-2343.

[156] Adelman B. J., Lei G.-D., Sachtler W. M. H., *Catal. Lett.* 28, **1994**, 119-130.

[157] Yokoyama C., Misono M., *J. Catal.* 150, **1994**, 9-17.

[158] Szanyi J., Kwak J. H., Peden C. H. F., *J. Phys. Chem B* 108, **2004**, 3746-3753.

[159] Sedlmair C., Gil B., Seshan K., Jentys A., Lercher J. A., *Phys. Chem. Chem. Phys.* 5, **2003**, 1897-1905.

[160] Monticelli O., Loenders R., Jacobs P. A., Martens J. A., *Appl. Catal. B* 21, **1999**, 215-220.

[161] Sultana A., Loenders R., Monticelli O., Kirschhock C., Jacobs P. A., Martens J. A., *Angew. Chem. Int. Ed.* 39, **2000**, 2934-2937.

[162] Sultana A., Habermacher D. D., Kirschhock C. E. A., Martens J. A., *Appl. Catal. B* 48, **2004**, 65-76.

[163] Bentrup U., Brückner A., Richter M., Fricke R., *Appl. Catal. B* 32, **2001**, 229-241.

[164] Brilhac J.-F., Sultana A., Gilot P., Martens J. A., *Environ. Sci. Technol.* 36, **2002**, 1136-1140.

[165] Kirschhock C. E. A., Sultana A., Godard E., Martens J. A., *Angew. Chem. Int. Ed.* 43, **2004**, 3722-3724.

CHAPTER 2

2. Experimental Section

2.1. Catalyst preparation

2.1.1. Na-Y

Zeolite Na-Y (Zeocat) was used for loading with different noble metals by cation exchange. Elemental analysis of the Na-Y zeolite was performed by inductively-coupled plasma atomic emission spectroscopy (ICP-AES) and was done at the Bodemkundige Dienst van België. The unit cell composition corresponded to $Na_{52}Al_{52}Si_{140}O_{384}$ resulting in a Si/Al atomic ratio of 2.7.

Na-Y zeolite was stored in a humidifier in air with 75% relative humidity obtained over saturated NH_4Cl solution. The physical water content of the water saturated Na-Y sample, determined using thermogravimetric analysis was 21 wt.-%. In all preparation procedures, water saturated Na-Y was weighed considering a water content of 21%.

2.1.1.1. Ru/Na-Y

Zeolite Na-Y (Zeocat) was loaded with ruthenium by cation exchange. Ammonia was added to 100 ml de-ionized H_2O to set the initial pH at 8.5. To this aqueous solution $RuCl_3$ (99+%, anhydrous, Acros) was added. The amount of $RuCl_3$ was dependent on the preferred Ru content in the zeolite, for example 0.18 g $RuCl_3$ was added for a Ru content of 3 wt.-%. After stirring this solution for 1 h, 3.63 g Na-Y powder was added. This suspension was stirred at 80 °C for 5 h. The addition of ammonia during the loading process was done to avoid ruthenium precipitation.[1] After filtration and washing with de-ionized water, the ruthenium loaded Na-Y zeolite was dried in static air at 60 °C and stored again in an atmosphere of constant humidity. Using this procedure, ruthenium in solution was quantitatively taken up by the zeolite as verified via ICP analysis. In the sample notation, the Ru content in wt.-% is indicated for dry zeolite conditions. Ru(3%)/Na-Y is the notation of a sample containing 0.03g Ru metal for each gram of dry Na-Y zeolite, corresponding to an ion exchange of 21% of the cation exchange capacity (CEC). Lower Ru contents were obtained by using less Ru in the same amount of solution and for the same quantity of zeolite (3.63 g water saturated zeolite, corresponding to 3 g dry zeolite).
The unit cell composition of the prepared Ru/Na-Y zeolites can be found in Table 1.

Table 1: Unit cell composition for Ru/Na-Y zeolites with different Ru contents verified by ICP-AES analysis.

Zeolite composition	Unit cell composition
Ru(3%)/Na-Y	$Ru_{3.7}Na_{41}Al_{52}Si_{140}O_{384}$
Ru(2%)/Na-Y	$Ru_{2.5}Na_{44.5}Al_{52}Si_{140}O_{384}$
Ru(1%)/Na-Y	$Ru_{1.3}Na_{48}Al_{52}Si_{140}O_{384}$
Ru(0.5%)/Na-Y	$Ru_{0.6}Na_{50}Al_{52}Si_{140}O_{384}$

2.1.1.2. Pt/Na-Y, Pd/Na-Y, Rh/Na-Y, Ir/Na-Y

Zeolite Na-Y was loaded with 3 wt.-% of Pt, Pd, Rh and Ir metal via ion exchange at 80 °C for 5 h followed by filtering, washing and drying at 60 °C as described in section 2.1.1.1. The following complexes were used as metal source: $Pt(NH_3)_4Cl_2.H_2O$, $Pd(NH_3)_4Cl_2.H_2O$, $Rh(NH_3)_5Cl_3$ and $IrCl_3.H_2O$ (Alfa Aesar). No ammonia was added to the aqueous solutions.

2.1.1.3. Ba,Na-Y

Zeolite Na-Y (Si/Al atomic ratio of 2.7, Zeocat) was cation exchanged by slurring 6.05 g of zeolite (corresponding to 5 g Na-Y on dry basis) in 1 dm^3 of a 0.05 M aqueous solution of $BaCl_2.2H_2O$ (Acros) for 16 h at room temperature as described in Monticelli *et al.*.[2] After filtration and washing with de-ionized water, the Ba-Y zeolite was dried in static air at 60 °C and stored in an atmosphere of constant humidity. Elemental analysis on this Ba-Y zeolite was performed by ICP-AES, analyzed at Bodemkundige Dienst van België v.z.w./Leuven/Belgium. The unit cell composition corresponded to $Ba_{17.3}Na_{17.3}Al_{52}Si_{140}O_{384}$ pointing at an ion exchange of 67% of the cation exchange capacity (CEC). Because of the high amount of Na^+ cations which are still present in this zeolite, we will refer to it as Ba,Na-Y.

2.1.1.4. Ru/Ba,Na-Y

The Ba,Na-Y zeolite, as prepared in section 2.1.1.3., was loaded with ruthenium. In order to avoid ruthenium precipitation, ammonia was added to 100 ml de-ionized H_2O to set the initial pH at 8.5 before $RuCl_3$ (99+%, anhydrous, Acros) was added. The amount of $RuCl_3$ was adapted to the targetted Ru content in the zeolite. After dissolution of the ruthenium salt under stirring at ambient temperature for 1 h, 3.63 g Ba,Na-Y zeolite (3 g on dry weight basis) was added. This suspension was stirred for 2.5 h at ambient temperature. After filtration and washing with de-ionized water, the ruthenium loaded Ru/Ba,Na-Y zeolite was dried in static air at 60 °C and stored in an atmosphere of constant humidity. Using this procedure, ruthenium in solution was quantitatively taken up by the zeolite as verified via ICP-AES analysis. In the sample notation, the Ru content in wt.-% denotes the weight increase of dry zeolite. Ru(0.5%)/Ba,Na-Y is the notation of a sample containing 5 mg Ru metal for each

gram of dry Ba,Na-Y zeolite. The corresponding unit cell composition is $Ru_{0.7}Ba_{17}Na_{15.8}Al_{52}Si_{140}O_{384}$.

2.1.2. Na-X (FAU)

Faujasite zeolite Na-X (Vetikon) with Si/Al ratio 1.2 and unit cell composition $Na_{86}Al_{86}Si_{106}O_{384}$, was available at the COK and was loaded with 3 wt.-% ruthenium by cation exchange using the procedure of section 2.1.1.1.

2.1.3. EMC-1 (FAU)

Zeolite EMC-1 was prepared according to method II in a publication by Chatelain *et al.*[3] (Si/Al 3.8). The various reactants which were used in this synthesis are given in Table 2.

Table 2: Products used for the synthesis of zeolite EMC-1.

Product		Composition	Function	Amount used (g)
Sodium aluminate	Riedel-de Haën	54% Al_2O_3, 41% Na_2O	Al source	3.64
Ludox® HS-40	Sigma-Aldrich	40% SiO_2, 60% H_2O	Si source	30.00
15-crown-5 ether	Acros	98%	template	2.25
NaOH	Riedel-de Haën	Purum 99%	alkali source	1.65
de-ionized H_2O			solvent	17.75

The molar composition of the starting mixture was:

10 SiO_2 : 1 Al_2O_3 : 2.1 Na_2O : 0.5 crown-ether : 100 H_2O

The EMC-1 zeolite was obtained by hydrothermal synthesis at 110 °C for 8 days. After filtration, washing with de-ionized water (400 ml) and drying in static air at 60 °C, the template was removed by calcination at 450 °C for 20 h.

XRD confirmed the formation of phase-pure zeolite EMC-1. The calcined EMC-1 zeolite was loaded with 3 wt.-% ruthenium by cation exchange using the procedure of section 2.1.1.1.

2.1.4. EMC-2 (EMT)

Zeolite EMC-2 was prepared according to Feijen *et al.*[4] (Si/Al 3.8). The reagents used for the preparation of the hydrogel are represented in Table 3.

Table 3: Reagents used for the synthesis of zeolite EMC-2.

Product		Composition	Function	Amount used (g)
Gibbsite	Fluka	64-66% Al_2O_3	Al source	3.14
Ludox® HS-40	Sigma-Aldrich	40% SiO_2, 60% H_2O	Si source	30.00
18-crown-6 ether	Acros	99%	template	5.18
NaOH	Riedel-de Haën	Purum 99%	alkali source	3.88
de-ionized H_2O			solvent	30.55

The molar composition of this gel was:

10 SiO_2 : 1 Al_2O_3 : 2.4 Na_2O : 0.97 crown-ether : 135 H_2O

The gel was aged at room temperature for 3 days. After that, the aged gel was transferred into Teflon-lined autoclaves and heated at 100 °C for 9 days. After this crystallization period, the autoclave was cooled down and the formed zeolite was recovered by filtration, washing with de-ionized water (400 ml) and drying in static air at 60 °C. Removal of the template was done by calcination in a muffle furnace at 550 °C for 20 h. An XRD pattern was taken after calcination and confirmed the formation of zeolite EMC-2. The calcined EMC-2 zeolite was further loaded with 3 wt.-% ruthenium by cation exchange using the procedure of section 2.1.1.1.

2.1.5. ZSM-3 (FAU/EMT)

Zeolite Na-ZSM-3 was available at the COK from the work by Xiong[5] at the COK and was synthesized following the procedure of Perez-Pariente *et al.*[6]. The zeolite was further loaded with 3 wt.-% ruthenium by cation exchange using the procedure of section 2.1.1.1.

2.1.6. LTL (LTL)

Zeolite LTL (Vetikon) with Si/Al ratio 3 and unit cell composition $K_9Al_9Si_{27}O_{72}$, was available at the COK and was loaded with 3 wt.-% ruthenium by cation exchange using the procedure of section 2.1.1.1.

2.1.7. ETS-10

Titanosilicate ETS-10 with Si/Ti ratio 5 was kindly provided by Engelhard and was loaded with 3 wt.-% ruthenium by cation exchange using the procedure of section 2.1.1.1.

Metal loaded zeolite powder was compressed under a hydrostatic pressure of 40 MPa and the compacted tablets were crushed and sieved to obtain pellets of 0.25-0.50 mm for use in an adsorbent bed. The zeolite pellets were pretreated at 450 °C for 1 h under a stream of nitrogen with 5% O_2 and 3% H_2O, unless stated otherwise.

2.2. Reactor Equipment

2.2.1. Gas phase reactor unit

Pellets of the synthesized catalysts (0.25-0.50 mm) were evaluated on their NO_x adsorption-desorption behavior. This was done by using gas mixtures which simulate on a realistic way the investigated compounds in exhaust of lean-burn gasoline and diesel engines.[7]

Cyclic NO_x adsorption-desorption experiments were conducted in a dual-line flow system with fixed adsorbent bed contained in a quartz tube. A flow chart of the set-up available at the COK is shown in Figure 1. Gases from cylinders were mixed and water vapor was introduced through a thermostatic water evaporator. The lean, oxidizing gas composition was 1000 ppm NO (Air Liquide, 5 ± 0.2 vol.-% NO in He), 3% H_2O, 5% O_2 and N_2 make up. Rich, reducing gas was composed of N_2 with 3% H_2O and 1% H_2. Switching from lean to rich conditions and vice versa was achieved without flow interruption. The temperature during adsorption and desorption was 250 °C, the total gas flow rate 150 ml STP/min and the catalyst volume 0.6 ml (400 mg water saturated zeolite), corresponding to a volumetric hourly space velocity (VHSV) of 15,000 h^{-1}. All the gas tubes were continuously kept at a temperature of 110°C in order to avoid condensation. The reactor set-up was partly computerized by the Camile TG program. The NO_x concentration was analyzed by an internally heated chemiluminescence detector (CLD 700 EL ht, Eco Physics); NH_3 concentration was measured via UV spectroscopy (Limas 11 HW analyzer) and N_2O with an Uras 26 NDIR analyzer (both ABB).

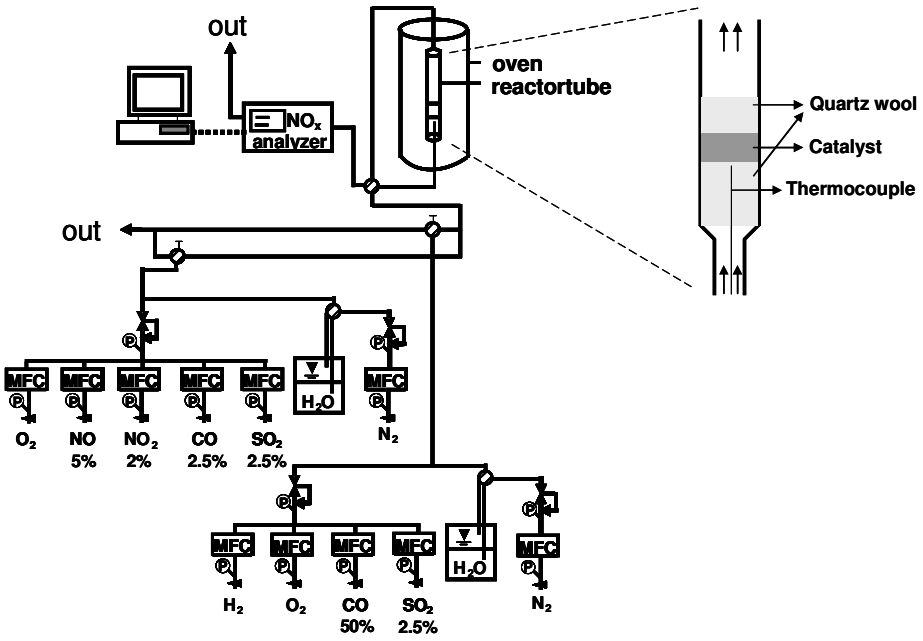

Figure 1: Fixed bed reactor set-up used for the evaluation of catalysts on their NO_x adsorption-desorption behavior. MFC: mass flow controller.

2.2.2. Chemiluminescence detector

The NO_x concentration at the in- and outlet of the adsorbent bed in the gas phase reactor unit, was analyzed using an internally heated chemiluminescence detector (CLD 700 EL ht, Eco Physics). The detection threshold was 0.1 ppm.[8]

The CLD is based on following measurement principle: sample gas is drawn into the analyzer and mixed with internally produced ozone. This leads to following reactions:

$$NO + O_3 \rightarrow NO_2^* + O_2 \quad (1)$$

$$NO + O_3 \rightarrow NO_2 + O_2 \quad (2)$$

Only about 20% of the NO_2 gas ends into the excited state (Eq. 1). These excited NO_2^* molecules reverts back into the ground state while emitting electromagnetic radiation (Eq. 3).

$$NO_2^* \rightarrow NO_2 + h\nu \quad (3)$$

This radiation emission is detected photo-electrically. When O_3 is present in excess, the signal is proportional to the NO concentration of the sample gas. By far the largest part of the excited NO_2^* molecules return back to the ground state without radiation emission. This is due to the collisions with other molecules (Eq. 4).

$$NO_2^* + M \rightarrow NO_2 + M \qquad (4)$$

This effect is known as quenching and the extent to which it occurs depends on the character of the colliding molecule M.

In order to measure the NO_2 content in the sample gas, it has first to be converted into NO. This reduction is done by passing the sample gas through a converter heated to 415 °C. Simultaneous NO and NO_x measurement is guaranteed by a two chamber construction as shown in Figure 2. The sample gas is divided into 2 equal streams. In the converter channel the total NO_x amount is measured. In the other channel the NO concentration is measured allowing determining the NO_2 concentrating by subtracting one from the other.

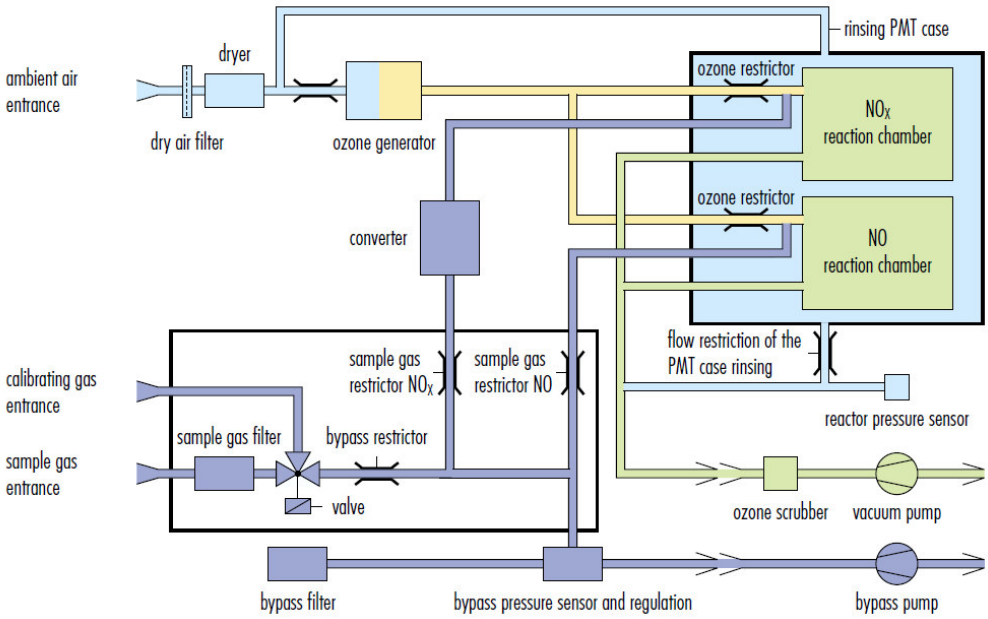

Figure 2: Schematic flow diagram of the chemiluminescence detector.[8]

2.2.3. Calculation of the NO_x ($NO + NO_2$) adsorption and desorption capacity

In the following chapters, the terms NO_x adsorption and desorption capacity are frequently used. The NO_x adsorption capacity refers to the amount of NO_x adsorbed by the adsorbent out of NO_x containing gasflow. This capacity is obtained by measuring NO_x concentrations and integration over time. The adsorption capacity is determined from the difference between the total amount of NO_x fed over the adsorbent bed and the outlet NO_x concentration. The desorption capacity corresponds to the amount of NO_x which is released by the adsorbent bed during a desorption phase and is estimated by integration of the NO_x concentration curve over time

The NO_x adsorption and desorption capacities and the corresponding standard deviations are estimated based on an average of 10 stable and reversible NO_x adsorption-desorption cycles and are expressed in mg NO_2/g dry zeolite.

2.3. Catalyst characterization

2.3.1. Powder X-Ray diffraction (XRD)

X-ray diffraction data were collected on a STOE STADI-P powder diffractometer equipped with a curved Ge(111)-monochromator and a linear position sensitive detector (6° 2 θ) with a resolution of about 0.01° 2θ at full width-half maximum (FWHM). All powder samples were sealed in 0.7 mm (outer diameter) glass capillaries (Hilgenberg) under dry nitrogen atmosphere and were measured with Cu $K_{\alpha 1}$-radiation in the range of $4° \leq 2\theta \leq 80°$ in Debye-Scherrer geometry with a step size of $\Delta\ 2\theta = 0.02°$. Asides determination of the present phases, the structure of the Ru zeolites was refined after ad- and desorption.

2.3.1.1. Rietveld refinement

Rietveld refinement is a powerful technique for extracting structural details from powder diffraction data. The Rietveld method refines user-selected parameters to minimize the difference between an experimental pattern (observed data) and a model based on the hypothesized crystal structure and instrumental parameters (calculated pattern). This method can provided information of the atomic positions and fractional occupancy.

Hugo Rietveld developed a method allowing to overcome the loss of scattering phases and the loss of the spatial relation of reflections by comparison of a simulated powder pattern with a measured data set.[9,10] By assigning a profile function to the measured reflection and refining this function in the course of the structure analysis, this method allowed handling of strongly overlapping reflections which previously was an insolvable problem. To reconstruct the structure of a crystalline structure from diffraction data, the intensity as well as the phase for each reflection, originating with a set of scattering planes has to be derived from the measured data.

The accurate description of the profile shapes allows concise extraction of intensities of each reflection which is necessary to determine the structure factor. In most cases a combination of Gaussian and Lorentzian components allowing for asymmetry, the Pseudo-Voigt profile successfully describes the general profile shape.[11] To account for line broadening effects due to particle size and/or strain, the Gaussian and

Lorentzian components contain terms with the corresponding dependence on the scattering angle.[12] For the refinements described in this work a variation of the Pseudo-Voigt profile with a very powerful handling of asymmetry, as developed by Finger *et al.* was chosen.[13] Experience taught that this function, implemented as continuous wave profile function N°3 in the GSAS software package[14], is well suited to account for the notoriously high asymmetry encountered with the intense low angle reflections of many zeolites.

Rietveld refinement depends on fitting a structural model to the measured data. The model is necessary to assign scattering phases to the observed reflections. Therefore a starting model already resembling the final structure is of essential importance. With these scattering phases it is possible to calculate the structure factor of the structure and to apply a Fourier transformation to convert it from reciprocal to real space and vice versa. Using the model phases it is possible to calculate electron density maps corresponding to the measured data and search therein for residual electron density not yet accounted for by the model. Using Rietveld refinement for the localisation of guest molecules within the structures of known crystalline phases therefore is exceptionally promising as the major scattering component of the unit cell, i.e. the host framework, already is known and therefore an ideal set of starting parameters is available. The whole method depends on matching a modelled diffraction pattern to an experimental set of data. Therefore tools for a critical assessment of the accuracy of the fit have to be available. For this assessment serve the R- factors, which are derived scaling the linear or square deviations of measured and calculated intensities. The corresponding parameters are the R_p and weighed R_{wp} factors. Naturally these not only depend on the goodness of the refined structure model but also heavily depend on the accurate description of the profile shape. Therefore often a third R factor, the R_f factor, is used. This factor compares calculated and measured structure factors for each observed reflection. To assess the accuracy of the obtained structure parameters often the estimated standard deviation (esd) is used. This assessment tool can be derived during the least square refinement routine and usually is listed in the structure tables in brackets, giving the values of the esd for the last digit of the respective parameter.

Typically guest molecules in a known porous material are refined as follows: a starting model serves the structure of the empty reference material. It is of advantage if the host material is prepared and measured with and without the sought guest under

identical conditions. This way a first refinement of the empty host readily yields a starting set. Alternatively, the starting model can be taken from literature, in case of zeolites from the database maintained by the structural commission of the International Zeolite Association.[15] At first, background, zeropoint shift and scaling factors are refined before the lattice constant also is left free to refine. Then the profile function is optimised to allow concise extraction of intensities of reflections. In a next step electron density charts are inspected for unaccounted electron density. The latter is inserted as fractional coordinates into the structural model. Special care has to be taken to remain consistent with the known composition of the unit cell. In the here present case, the number and type of cations in the framework have to be respected. This involves constraining the occupation numbers of cations on the located sites. As there are only limited solutions which can account for the observed electron density on one hand and the known numbers of cations on the other, identification of the type of cation on a crystallgraphic site is feasible. A further help for this identification are the typical distances of the cations to ligand (water) and framework. Successive cycles of this procedure eventually lead to increasingly improved structure solutions. When the fit of the structure has reached a satisfactory level, which admittedly is a rather subjective impression, also the framework itself can be left to refinement. Obviously, any extra information asides exact knowledge of unit cell composition will also improve the level of confidence of the finally observed structure so that the most significant structure solutions by Rietveld refinement always are in combination with spectroscopic and other scientific methods of characterisation.

Ru/Na-Y samples with a Ru content of 1 wt.-% and Ru/Ba,Na-Y samples with a Ru content of 0.5 wt.-% were refined. Rietveld refinements and Difference Fourier Electron Density Analyses were done in collaboration with Prof. Christine Kirschhock and were performed using the GSAS/EXPGUI software package. The starting model was generated from the structure parameters published by the International Zeolite Association.[15] Cation and water occupation numbers were constrained to account for the experimentally determined unit cell composition.

2.3.2. ^{23}Na Magic Angle Spinning Nuclear Magnetic Resonance (^{23}Na MAS NMR)

NMR is based on the existence of a nuclear spin which can be thought of as a small magnetic field. The spin of a nucleus is called the spin quantum number (*I*) and is determined by the internal structure of the nucleus. The application of this technique is therefore limited to nuclei with a spin quantum number. When the nucleus is placed in an external magnetic field, the nuclear spin will orientate itself according to the external magnetic field. However, not every orientation is allowed. Between the different orientations, there is an energy difference (ΔE) which corresponds with a specific frequency (ν) of the electromagnetic spectrum. This is called the resonance frequency. When nuclei with a spin quantum number are placed in a magnetic field and irradiated with the resonance frequency, some nuclei will absorb the electromagnetic radiation and go to a higher energy level, changing thereby the direction of their magnetic field. At the same moment, some nuclei with increased energy will emit energy and change orientation. Those transitions are only possible when the energy difference between the energy levels of the nuclear spin is the same as the energy of the incoming electromagnetic radiation. However, in a molecule, not every nucleus has the same electron density. Electrons shield the nucleus, changing thereby the magnetic properties of the nucleus. Depending on the chemical local environment of the nucleus, the resonance frequency will change. This phenomenon is known as the chemical shift (δ), expressed in parts per million (ppm), and measured relative to a reference compound. The chemical shift allows determining the structure of molecules.[16-18]

A problem with solid samples is the broadening of the spectral lines compared to liquid samples. This is due to all sorts of interactions (dipolar, chemical shift, quadrupolar, paramagnetic) which have one common factor: the geometric factor ($3\cos^2\theta - 1$). When this factor is 0, the spectral lines are narrow. When the rotor, which contains the solid sample, is placed under an angle of 54.7 °, this geometric factor becomes 0, resulting in more narrow spectral lines. This angle is called the magic angle.[16,17]

^{23}Na MAS NMR spectra were recorded on a Bruker Avance DSX400 spectrometer (9.4 T). 5550 scans were accumulated with a recycle delay of 1 s. The samples were

packed under inert atmosphere in 2.5 mm rotors. The spinning frequency of the rotor was 20 kHz. Solid NaCl was used as chemical shift reference. ^{23}Na has a spin quantum number of 3/2.

2.3.3. Extented X-ray Absorption Fine Structure (EXAFS)

X-ray absorption spectroscopy is a spectroscopic method in which an electron is excited from one energy level to another. On the other hand, it is also a scattering method in which an ejected photoelectron is scattered through atoms surrounding the absorber. Electronic excitations from deep core levels of the absorbing atom to valence and continuum levels give sensitivity to electronic structure, including oxidation state of the absorber. The interference between outgoing and backscattered photoelectron waves provides the local structure of an absorber atom.[19]

An X-ray absorption spectrum can be divided into three regions: 1) the pre-edge region, 2) the absorption edge and the X-ray absorption near-edge structure (XANES) and 3) the extended X-ray absorption fine structure (EXAFS).[19]

When a beam of X-ray photons, produced by a synchrotron, passes through a material, the incident intensity (I_0) will be decreased by an amount that is determined by the absorption characteristics of the material being irradiated:

$$I_t = I_0 \, e^{-\mu(E)x} \qquad (5)$$

where I_t is the intensity of the transmitted photons, $\mu(E)$ the linear absorption coefficient and x the absorption path length which is the thickness of the sample. If the energy of the incident X-ray beam ($h\nu$) is high enough to excite a core electron to an empty state or the continuum (unbound), a sharp rise in the absorption intensity appears, denoted as the X-ray absorption edge or threshold energy. Since the excitation energy depends on the binding energy (E_b) of the core-level, the absorption edge is element specific.[20] The consecutive edges are named after the origin of the electron. In case of a K-edge, the electron is excited from the first electron shell (K-shell). As $h\nu$ increases beyond E_b, electrons can be ejected to continuum levels and remain in the vicinity of the absorber for a short time with excess kinetic energy. In the energy region extending from just above to 50 eV beyond E_b, the electrons are multiply scattered among neighbouring atoms, producing the XANES spectrum which

provides information about the coordination geometry and oxidation state. When hν is about 50 to 1500 eV above E_b, electrons are ejected from the absorber and they are singly or multiply backscattered through first or second neighbor atoms.[20] The interference between outgoing and backscattered photoelectrons modulates the absorption process, creating an EXAFS spectrum. Because the interference pattern, also called as the fine structure, is not only determined by the type of atoms but also by the position of these atoms, EXAFS provide detailed geometrical information.[21] The absorption coefficient above the absorption edge is defined as

$$\mu_{tot} = \mu_0 (1 + \chi(k)) \quad (6)$$

where μ_0 is the atomic background and $\chi(k)$ the oscillatory EXAFS part of the spectrum as a function of the wave vector k. $\chi(k)$ describes the summation over all interference patterns scattered off of all neighboring atoms:

$$\chi(k) = \sum_j A_j (k) \sin (2 k R_j + \varphi_j (k)) \quad (7)$$

with j referring to the j^{th} coordination shell, R_j the distance of the absorber atom to this coordination shell, $A_j(k)$ the backscattering amplitude and φ_j (k) the phase shift experienced by the photoelectron[21]. The backscattering amplitude $A_j(k)$ is a function of k:

$$A_j(k) = \frac{S_0^2 e^{-2R_j/\lambda}}{kR_j^2} N_j F_j(k) e^{-2\sigma_j^2 k^2} \quad (8)$$

In this equation N_j presents the coordination number and $F_j(k)$ is the magnitude of the backscattering amplitude which is element specific. S_0^2 is an amplitude reduction factor and approximates the loss in photon intensity. The exponential term contains the mean free path of the photoelectron λ which accounts for the finite lifetime of the excited state. The thermal motion and structural disorder in the distance R_j is described by the Debye-Waller factor σ.[19-21]

Fourier transformation of the EXAFS data results eventually in a radial atomic distribution function. In that way, EXAFS data will not only provide information about the type and the number of neighbors but also their distance to the scatterer and their disorder.[19-21]

Because EXAFS is a bulk technique, an average of all different compounds is obtained. This makes the data-analysis and the interpretation severely complicated. Furthermore, the concentration of the species which are investigated should be high enough to be able to measure them with a good signal to noise ratio. A specific compound in a mixture can only be distinguished if it is present in amounts higher than 10 to 20%.[21]

Ru K-edge Extended X-ray Absorption Fine Structure (EXAFS) spectroscopy experiments were carried out at the Dubble beamline BM26A at the European Synchrotron Radiation Facility (ESRF) in Grenoble, France. A double crystal monochromator Si(311) was used. The measurements were performed in transmission mode using optimized ionization chambers as detector. The spectra were calibrated using a Pd foil (1^{st} maximum 1^{st} derivative 24350 eV). The samples were prepared by pressing 0.3 g powder for 10 minutes at 20 kN into tablets (13 x 2 mm). These tablets were placed into a sample holder with kapton film as an X-ray transparent window.
The experiments were performed at room temperature. XAS data processing and EXAFS analysis were performed using IFEFFIT[22] with the Horae package[23] (Athena and Artemis). The hexagonal close packed structure of Ru metal was used as a fitting model for the Ru particles in the zeolite samples (space group P63/mmc with cell parameters a = b = 270.59 pm c = 428.15 pm, $\alpha = \beta = 90°$, $\gamma = 120°$).[24]

2.3.4. Transmission Electron Microscopy (TEM)

TEM measurements were done at the Department of Metallurgy and Materials Engineering (KULeuven) and performed using a Philips CM200 FEG microscope operating at 200 kV. The sample was crushed between two glass plates and deposited on a Cu TEM grid containing holey C-film, without any contact with solvent.

2.3.5. ^{99}Ru Mössbauer spectroscopy

Mössbauer spectroscopy is based on the phenomenon of recoilless resonance absorption of γ-rays by the atomic nuclei immersed in a crystalline or disordered solid environment.[25-28] Under normal conditions atomic nuclei recoil when they emit γ-rays and the wavelength of the emission varies with the amount of recoil. Mössbauer found that at a low temperature, the recoil momentum during absorption and emission of the γ photon is taken up by its entire lattice. This reduces the recoil energy to nearly zero and thus allows resonance absorption to occur.[26,27]

The frequency of the nuclear γ transition depends on the interaction with the surrounding electronics and is therefore influenced by the local electronic structure and chemical environment of the resonating atom. The Mössbauer isomer shift δ is defined as a measure of the energy difference between the energies of γ transitions occurring in the sample (absorber) nucleus as compared to the reference (source) nucleus. In a typical transmission experiment, the energy of the γ-rays emitted by the source containing the Mössbauer nuclei, is shifted over a broad energy range via a Doppler shift, obtained by moving the source with respect to the absorber. Velocities of a few millimetres per second are required. The γ-rays transmitted by the absorber at different energies can be counted by a detector placed behind the absorber. A drop in counting rate is then due to resonant absorption. The γ-rays detected per second are plotted as a function of the Doppler velocity, resulting in a Mössbauer effect absorption spectrum.[25-28]

The Mössbauer effect has been observed in more than 35 isotopes. Suitable isotopes must have a stable or long-lived ground state and a low-lying excited state that decays to an appreciable extent by gamma-ray emission.[27]

^{99}Ru Mössbauer spectroscopy was done at the Physics Department of the Buffalo State College (Buffalo, USA). In the ^{99}Ru Mössbauer experiment a ^{99}Rh(Ru) source was used. The isotope ^{99}Ru is 12% of naturally occurring ruthenium. This source was produced by proton irradiation at the University at Buffalo cyclotron on enriched ^{100}Ru and ^{101}Ru targets. The production mechanism proceeded by using (p, 2n) and (p, 3n) reaction using 30 MeV protons. The ^{99}Rh source produced 90 keV gamma rays which were resonantly absorbed in the isotope of ^{99}Ru present in the natural Ru in the absorber sample. The sample holder was filled under dry nitrogen atmosphere and

contained 24 mg natural Ru/cm^2. The sample holder was sealed afterwards. The source and the absorber were both mounted inside a low temperature gas exchange cryostat allowing the experiment to be performed at temperatures below 78 K and near 25 K. The calibration for the velocity of the drive was performed using the inner four lines of the six lines in the standard experiment using Fe foil with a source of ^{57}Co(Rh). The calibration experiment with ^{99}Rh(Ru) versus Ru metal powder established the zero velocity signal.

2.4. References

[1] Jacobs P. A., *Studies in Surface Science and Catalysis*, Vol. 12, Jacobs P.A., Jaeger N. I., Jíru P., Schulz-Ekloff G., Eds., Elsevier, Amsterdam, **1982**, 71-85.

[2] Monticelli O., Loenders R., Jacobs P. A., Martens J. A., *Appl. Catal. B* 21, **1999**, 215-220.

[3] Chatelain T., Patarin J., Soulard M., Guth J. L., Schulz P., *Zeolites* 15, **1995**, 90-96.

[4] Feijen E. J. P., De Vadder K., Bosschaerts M., Lievens J. L., Martens J. A., Grobet P. J., Jacobs P. A., *J. Am. Chem. Soc.* 116, **1994**, 2950-2957.

[5] Xiong Y., *Synthesis and characterization of the low silica FAU/EMT intergrowth zeolites ZSM-2 and ZSM-3*, Doctoraatsproefschrift Nr. 263, Faculteit Landbouwkundige en Toegepaste Biologische Wetenschappen, Katholieke Universiteit Leuven, **1994**, 119p.

[6] Perez-Pariente J., Fornes V., Martens J. A., Jacobs P. A., *Studies in Surface Science and Catalysis*, Vol. 37, Grobet P. J., Mortier W. J., Vansant E. F., Schulz-Ekloff G., Eds., Elsevier, Amsterdam, **1988**, 123-131.

[7] Kaspar J., Fornasiero P., Hickey N., *Catal. Today* 77, **2003**, 419-449.

[8] Website Ecophysics, http://ecophysics-us.com/pdf/source_emissions/700elht_eu.pdf, January **2010**.

[9] Rietveld H. M., *Acta Cristallogr.* 22, **1967**, 151-152.

[10] Rietveld H. M., *J. Appl. Crystallogr.* 2, **1969**, 65-71.

[11] Thompson P., Cox D. E., Hastings J. B., *J. Appl. Cryst.* 20, **1987**, 79-83.

[12] Balzar D., Audebrand N., Daymond M., Fitch A., Hewat A., Langford J. I., Le Bail A., Louër D., Masson O., McCowan C. N, Popa N. C, Stephens P. W., Toby B., *J. Appl. Cryst.* 37, **2004**, 911-924.

[13] Finger L. W., Cox D. E., Jephcoat A. P., *J. Appl. Cryst.* 27, **1994**, 892-900.

[14] Larson A. C., Von Dreele R. B., *General Structure Analysis System (GSAS)*, Los Alamos National Laboratory Report LAUR 86-748, **2004**.

[15] Website International Zeolite Association, http://www.iza-structure.org/, March **2010.**

[16] Abraham R.J., Fisher J., Loftus P., *Introduction to NMR spectroscopy*, 2nd Ed.,Wiley, Chichester, **1999**, 271p.

[17] Harald G., *NMR spectroscopy : basic principles, concepts, and applications in chemistry*, 2nd Ed., Wiley, Chichester, **1996**, 581p.

[18] Hore P. J., *Nuclear magnetic resonance*, Oxford University Press, Oxford, **1995**, 90p.

[19] Koningsberger D. C., Mojet B. L., van Dorssen G. E., Ramaker D. E., *Top. Catal.* 10, **2000**, 143-155.

[20] Koningsberger D. C., Prins R., *X-ray absorption : principles, applications, techniques of EXAFS, SEXAFS, and XANES*, Wiley Interscience, New York, **1988**, 673p.

[21] Boon K. T., *EXAFS : basic principles and data analysis*, Springer, Berlin, **1986**, 349p.

[22] Newville M., *J. Synchrotron Rad.* 8, **2001**, 322-324.

[23] Ravel B., Newville M., *J. Synchrotron Rad.* 12, **2005**, 537-541.

[24] Finkel V. A., M. Palatnik M. I., Kovtun G. P., *Phys. Met. Metall.* 32, **1971**, 231.

[25] Filatov M., *Coord. Chem. Rev.* 253, **2009**, 594-605.

[26] Dickson D. P. E., Berry F. J., *Mössbauer Spectroscopy*, Cambridge University Press, Cambridge, **1986**, 274p.

[27] Cranshaw T. E., Dale B. W., Longworth G. O., *Mössbauer Spectroscopy and its Applications*, Cambridge University Press, Cambridge, **1985**, 119p.

[28] Millet J.-M. M., *Adv. Catal.* 51, **2007**, 309-350.

CHAPTER 3

3. Reversible NO_x storage over Ru/Na-Y

Ruthenium loaded Na-Y zeolite was found to be an efficient adsorbent for achieving NO_x adsorption-desorption cycles comprising adsorption under oxidizing and desorption under reducing conditions. The speciation of ruthenium was investigated using TEM, EXAFS, ^{99}Ru Mössbauer spectroscopy and XRD in combination with Rietveld refinement. The sodium cation siting was monitored using ^{23}Na MAS NMR. Characterization of the Ru/Na-Y adsorbent in NO_x saturated and regenerated state revealed a unique cooperation of ruthenium metal clusters outside the zeolite and isolated Ru atoms in the framework cavities affecting the sodium cations. Supported ruthenium nanoparticles assume a catalytic role in NO oxidation. The oxidation state of ruthenium atoms in the framework cavities is switched during adsorption-desorption cycles. It triggers reversible sodium cation migrations from coordination with the framework in the regenerated state to coordination in sodium-water networks in supercages providing adsorption sites for NO_x during adsorption. The peculiar ruthenium organization is naturally obtained upon cycling the adsorbent irrespective of pretreatment conditions. Ru/Na-Y adsorbent is insensitive to SO_x and to the presence of CO during reductive regeneration.

3.1. Introduction

Nitrogen oxides (NO_x) are produced in combustion processes of solid, liquid or gaseous fuel in presence of air. Especially the NO_x emitted in the troposphere by traffic is of major concern.[1] In cities with high traffic density NO_x contributes to photochemical smog formation affecting human health.[2-5] One solution to the NO_x emission problem is the development of customized exhaust gas cleaning techniques for the different engine types.[6] Three-way catalysts can achieve simultaneous and almost complete removal of uncombusted hydrocarbons, carbon monoxide and NO_x from exhausts of gasoline engines, operated at nearly stoichiometric air-to-fuel ratio.[7] Higher fuel efficiency and reduced emissions of the greenhouse gas CO_2 make diesel and lean-burn engines attractive compared to conventional gasoline engines. However, controlling the exhaust NO_x emission has been recognized as one of the most challenging aspects for lean-burn engine technology as the conventional three-way catalyst is not effective in reducing NO_x in a lean exhaust due to the high oxygen level. A NO_x storage and reduction (NSR) catalyst is among the most promising solutions to control NO_x in lean exhaust.[8-10] The NSR catalyst contains a storage component, e.g. $BaCO_3$ or BaO, in order to store NO_x as nitrates under lean conditions. Catalyst regeneration is necessary as the storage capacity of the adsorbing component gets saturated. Regeneration takes place by introduction of a short period of rich driving, as injections of extra fuel cause decomposition of stored NO_x and subsequent reduction into N_2.[11,12] A precious metal, mostly Pt, is used for the oxidation of NO into NO_2 during lean conditions and the reduction of NO_2 to N_2 during regeneration. A critical aspect of the NSR technology is the catalyst deactivation by sulfur.[13-15]

Zeolites are gaining popularity in automotive exhaust gas treatment and the potential of zeolites for NO_x adsorption in view of NSR applications has been investigated.[16-19] Generally, in alkali and alkaline earth metal exchanged Y zeolites NO_x is adsorbed as surface nitrates.[18-20] In Na-Y zeolite NO_x can be adsorbed according to a different mechanism.[21] At temperatures above 200 °C, NO and NO_2 are co-adsorbed as N_2O_3 molecules which compete with three water molecules for an adsorption site composed of sodium cations in the zeolite Y supercage. The stored NO_x can be released in a pressure swing process using hydrated inert gas. The

presence of SO_x does not have an influence on the NO_x storage capacity owing to a different location of adsorbed SO_x and NO_x molecules in the Na-Y cages.[22,23] Nevertheless, Na-Y fails short in practical applications due to the slow NO_x desorption kinetics and the requirement of an equimolar mixture of NO and NO_2 in the exhaust, which is difficult to achieve.[21-24] Since NO is the main NO_x compound of engine exhaust gas, NO_x adsorption on Na-Y is critically dependent on NO into NO_2 oxidation. Practically the oxidation could be achieved using an upfront catalyst. Incorporation of an oxidation function via a supported noble metal on the Na-Y zeolite itself could be an elegant solution.

Exceptional catalytic activity of ruthenium metal dispersed on zeolites including Na-Y zeolite in redox reactions has been observed in carbon oxidation[25], Fischer-Tropsch synthesis[26], the water gas shift reaction[27], ammonia synthesis[28,29] and carbon monoxide oxidation[30]. In this chapter ruthenium is evaluated as a NO oxidation catalyst during lean-rich NO_x adsorption-desorption cycles. For better understanding of catalyst behavior, catalyst characterization using EXAFS, XRD and Rietveld refinement in combination with analysis of difference electron density charts, ^{23}Na MAS NMR, ^{99}Ru Mössbauer spectroscopy and TEM have been done. The loading of Na-Y with ruthenium resulted in a remarkable adsorption behavior characterized by trapping of pure NO and accelerated desorption kinetics. In the Ru/Na-Y adsorbent, ruthenium particles exert a redox catalytic function. In addition, isolated ruthenium atoms in the framework cavities undergo reversible oxidation and reduction which causes dramatic sodium cation migration. Cation migration in zeolites induced by adsorbate molecules is a known phenomenon.[31-34] Here we demonstrate a cooperation of reducible and non-reducible cations which allows switching of the cation distribution in the framework cavities. This mechanism reversibly generates and destroys the adsorption site for NO_x.

3.2. Results and Discussion

Ru(3%)/Na-Y zeolite was loaded in the adsorption unit and subjected to NO_x adsorption-desorption cycles at 250 °C as shown in Figure 1. Inlet gas composition during adsorption was 1000 ppm NO, 5% O_2, 3% H_2O and N_2. N_2 spiked with 1% H_2 and 3% H_2O was used for desorption.

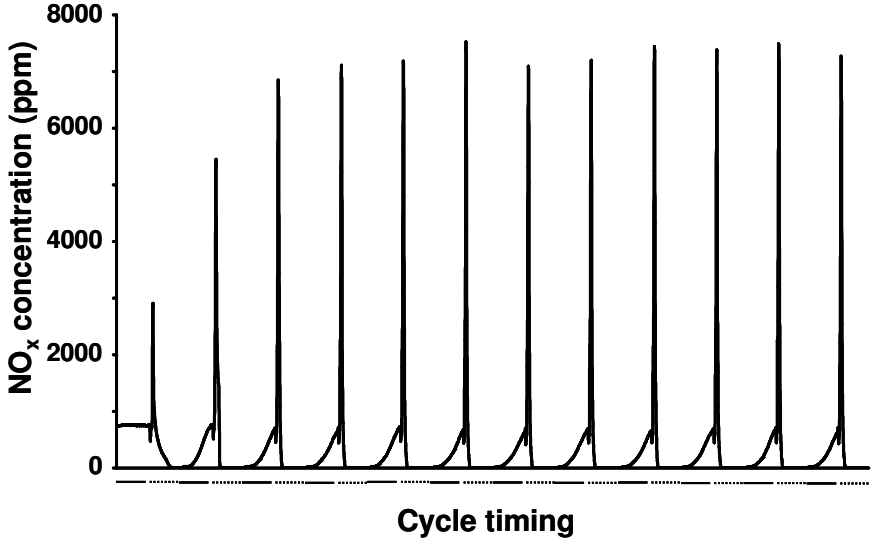

Figure 1: NO_x concentration traces at the adsorber outlet in cycles with 5 min. adsorption (—) and 5 min. desorption (·····) on a Ru(3%)/Na-Y zeolite at 250 °C. The Ru(3%)/Na-Y catalyst was pretreated at 450 °C for 1 h under a flow containing 5% O_2, 3% H_2O and balance N_2. Lean composition was 1000 ppm NO, 5% O_2, 3% H_2O and balance N_2 and regeneration of the adsorbent bed was done with 1% H_2, 3% H_2O and balance N_2.

It typically took around 4 to 5 cycles before stable and reversible NO_x adsorption-desorption cycles were obtained. In a representative later cycle shown in Figure 2, significant NO_x uptake was observed during the first minutes of the adsorption phase. From the beginning, the main compound in the NO_x outlet (i.e. unadsorbed NO_x) was NO_2 which revealed the strong oxidation activity of Ru(3%)/Na-Y. After switching to regeneration gas, sudden NO_x desorption was obtained which was completed within 1 minute. The NO_x adsorption capacity was 3.2 ± 0.1 mg NO_x/g. Part of the adsorbed NO_x was released (1.6 ± 0.1 mg NO_x/g), mainly as NO. Formation of only small

amounts of NH_3 and N_2O was detected revealing that a substantial part of the NO_x was reduced by hydrogen to N_2.

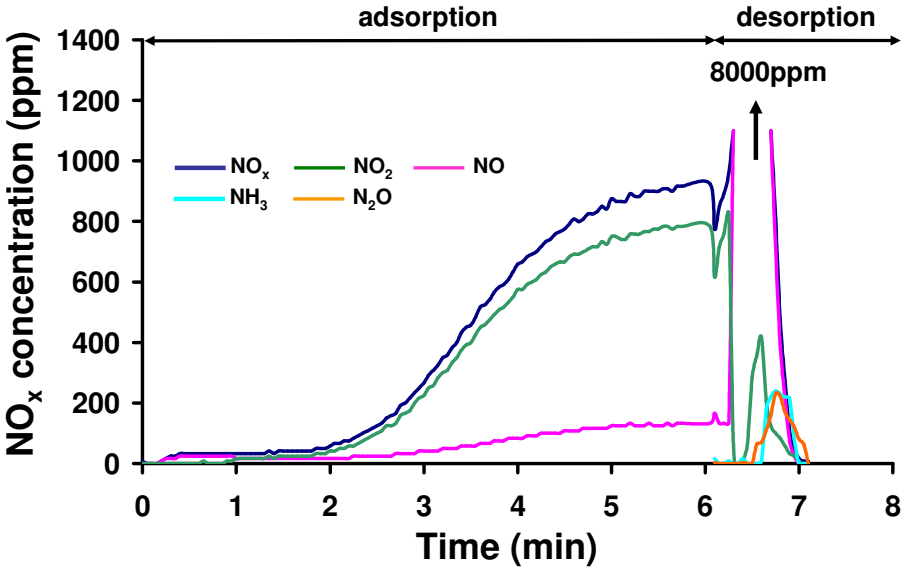

Figure 2: A detailed NO_x adsorption-desorption pattern recorded at the outlet of a Ru(3%)/Na-Y adsorbent bed at 250 °C. The catalyst was pretreated at 450 °C for 1 h under a flow of 5% O_2, 3% H_2O and balance N_2 before adsorption-desorption cycles started. Gas composition during lean phase was 1000 ppm NO, 5% O_2, 3% H_2O and balance N_2. Regeneration of the bed during rich phase was done with 1% H_2, 3% H_2O and balance N_2.

The use of Rh, Pt, Pd or Ir instead of Ru metal on the same Na-Y zeolite led to at least three times lower NO_x adsorption capacity, ill defined adsorption profiles (Pt) and low NO oxidation activity (Pd, Ir, Rh) as shown in Figure 3.

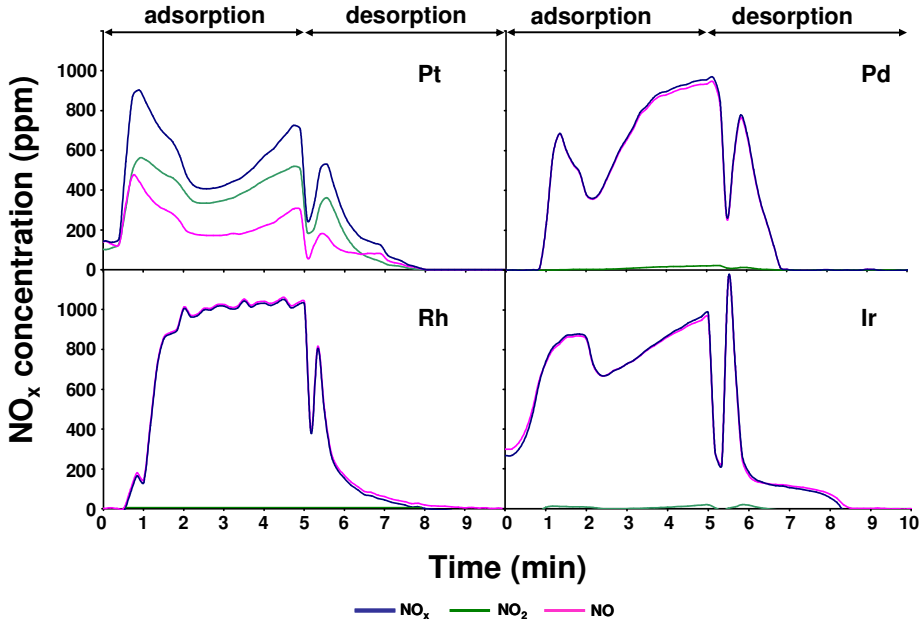

Figure 3: Detailed NO_x adsorption-desorption patterns recorded at the outlet of a Pt(3%)/Na-Y, Pd(3%)/Na-Y, Rh(3%)/Na-Y and Ir(3%)/Na-Y adsorbent bed at 250 °C. All the catalysts were pretreated at 450 °C for 1 h under a flow of 5% O_2, 3% H_2O and balance N_2. Shown are typical reproducible cycles after some time of operation. Gas composition during lean phase was 1000 ppm NO, 5% O_2, 3% H_2O and balance N_2. Regeneration of the bed during desorption phase was done with 1% H_2, 3% H_2O and balance N_2.

The incorporation of 3 wt.-% Ru in zeolites NaX, EMC-1 (both FAU), EMC-2 (EMT), ZSM-3 (FAU/EMT), LTL (LTL) and in the titanosilicate ETS-10 led to poor results. An overview is given in Table 1. All Ru loaded supports were first pretreated at 450 °C for 1 h under a flow of 5% O_2, 3% H_2O and balance N_2. Gas composition during lean phase was 1000 ppm NO, 5% O_2, 3% H_2O and balance N_2. Regeneration of the bed during desorption phase was done with 1% H_2, 3% H_2O and balance N_2. The NO_x adsorption-desorption cycles were performed at a temperature of 250 °C

Table 1: Overview of the NO_x adsorption-desorption behavior of other Ru exchanged adsorbents.

Adsorbent	Observation during NO_x adsorption-desorption cycles
Ru(3%)/Na-X	very irregular and non-reproducible NO_x adsorption-desorption behavior
Ru(3%)/EMC-1	very low adsorption capacity
Ru(3%)/EMC-2	ill-defined adsorption-desorption profile
Ru(3%)/ZSM-3	low adsorption capacity
Ru(3%)/LTL	no adsorption-desorption behavior
Ru(3%)/ETS-10	ill-defined profiles

Zeolites other than Na-Y presented either little adsorption capacity, or failed to produce reversible NO_x adsorption-desorption cycles. It was decided to focus the work on Ru/Na-Y zeolite.

The rapid NO_x release was a remarkable effect of loading ruthenium on Na-Y zeolite. The peak NO_x concentration amounted 8000 ppm (Figure 2). Ru/Na-Y adsorbent in absence of O_2 during the adsorption phase did not show any NO_x adsorption activity. Raising the O_2 content from 1 to 5% systematically increased the NO_x adsorption capacity. At higher O_2 concentrations up to 10%, there was quantitative oxidation of NO into NO_2 and no longer an influence of O_2 concentration on NO_x adsorption capacity. At all gas compositions with an oxygen content of 5% or more, Ru(3%)/Na-Y catalyst established the internal thermodynamic equilibrium of NO, O_2 and NO_2.[9] The thermodynamic NO/NO_2 ratio at 250 °C and in presence of 5% O_2 amounted 15/85; in presence of 10% O_2 it was 10/90. Feeding 500 ppm NO and 500 ppm NO_2 instead of 1000 ppm NO in presence of 5% O_2 did not alter the adsorption performance. Feeding 1000 ppm NO_2 in presence of 5% O_2 caused a decrease of the adsorption capacity to 2.1 ± 0.1 mg NO_x/g. The latter observation points at the necessity of NO being present in the NO_x mixture.

In another set of NO adsorption experiments the water content of the feed was varied. There was no NO_x adsorption in absence of water. In the presence of 3% up to 12% water, a similar NO_x adsorption behavior was observed. The peak NO_x concentrations during regeneration were however more irregular when more water was present in desorption gas composition. When the water supply was interrupted during the adsorption phase of a cycle, Ru(3%)/Na-Y immediately lost its NO_x adsorption property. Adding water restored quickly the NO_x adsorption activity as shown in Figure 4.

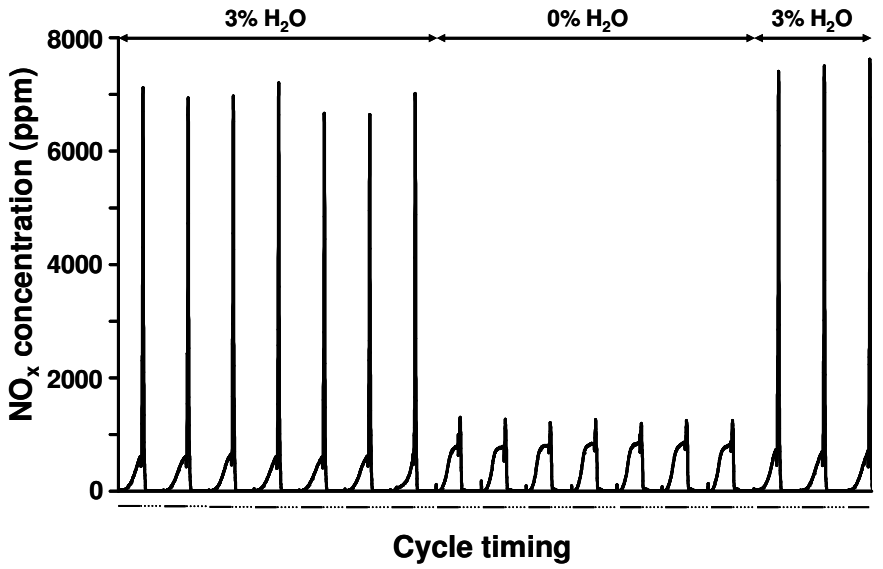

Figure 4: NO_x concentration traces at the adsorber outlet in cycles with 5 min. adsorption (—) and 5 min. desorption (·····) on a Ru(3%)/Na-Y zeolite at 250 °C in presence of different H_2O concentrations. The Ru(3%)/Na-Y catalyst was pretreated at 450 °C for 1 h under a flow containing 5% O_2, 3% H_2O and balance N_2. Lean composition was 1000 ppm NO, 5% O_2, 3% H_2O and balance N_2 and regeneration of the adsorbent bed was done with 1% H_2, 3% H_2O and balance N_2.

The NO_x adsorption capacity was investigated at different volumetric space velocities. In the VHSV range of 7,500 – 45,000 h^{-1}, the NO_x adsorption capacity was little dependent on space velocity (Figure 5). Increasing the VHSV to 75,000 and 100,000 h^{-1} caused a significant drop. Under those conditions the NO into NO_2 oxidation function was found to be limiting.

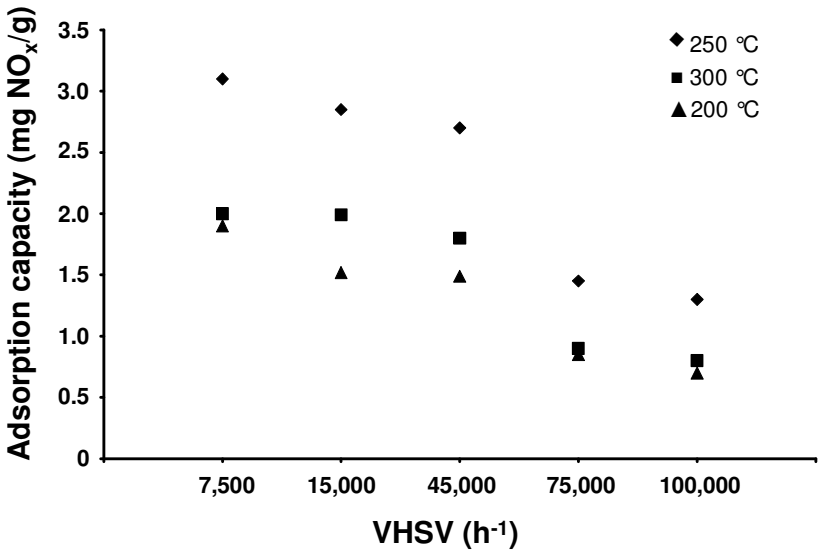

Figure 5: NO_x adsorption capacity of a Ru(3%)/Na-Y zeolite at different volumetric space velocities and different reaction temperatures (♦ 250 °C, ■ 300 °C, ▲ 200 °C). The NO_x adsorption capacities were calculated based on an average of 10 cycles. The standard deviation of the NO_x adsorption capacities was less than ± 0.1 mg NO_x/g in all data points.

Ru(3%)/Na-Y adsorbent after pretreatment at 450 °C for 1 h under 5% O_2 and 3% H_2O was characterized using powder X-ray diffraction in sealed capillaries. In addition to the diffraction patern of Na-Y, a crystalline anhydrous RuO_2 phase with characteristics diffraction peaks at 28.4, 35.3 and 54.4 ° 2θ was detected. After running several adsorption-desorption cycles at 250 °C, in the regenerated sample as well as in the NO_x saturated sample, no RuO_2 was detected by XRD. Instead, Ru metal was identified by a broadened diffraction peak around 44 ° 2θ (Figure 6).

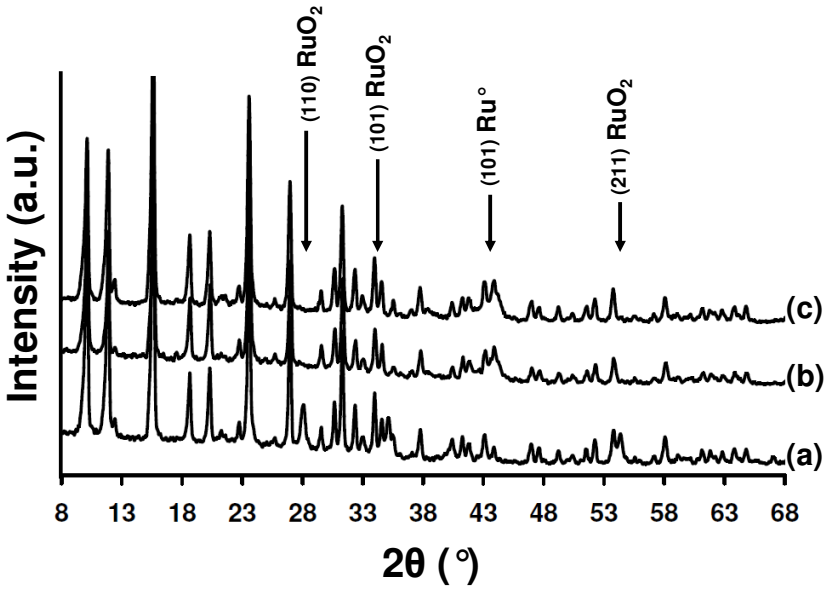

Figure 6: XRD pattern of Ru(3%)/Na-Y after (a) pretreatment, (b) NO_x saturation and after (c) NO_x release. Pretreatment was done at 450 °C for 1 h under a flow of 5% O_2, 3% H_2O and balance N_2 before adsorption-desorption cycles at 250 °C. Lean gas composition was 1000 ppm NO, 5% O_2, 3% H_2O and balance N_2. Rich composition was 1% H_2, 3% H_2O and balance N_2.

The presence of a segregated ruthenium phase was confirmed by TEM (Figure 7). The elongated particles measuring 30-150 nm observed outside of the zeolite crystals were ascribed to Ru metal.[35]

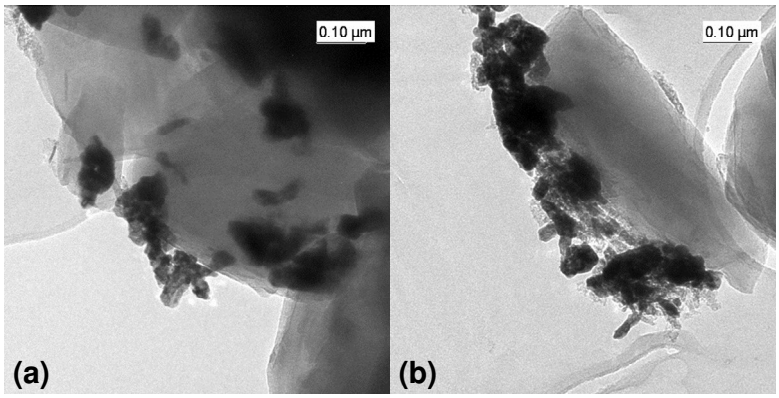

Figure 7: TEM images of a Ru(3%)/Na-Y zeolite after (a) NO_x saturation and (b) NO_x release.

NO_x saturated and regenerated adsorbent sample after 10 NO_x adsorption cycles under standard conditions (Figure 1) were sealed and investigated with EXAFS spectroscopy. The experimentally $\chi(k)$ EXAFS functions obtained for both samples were found to be similar as shown in Figure 8.

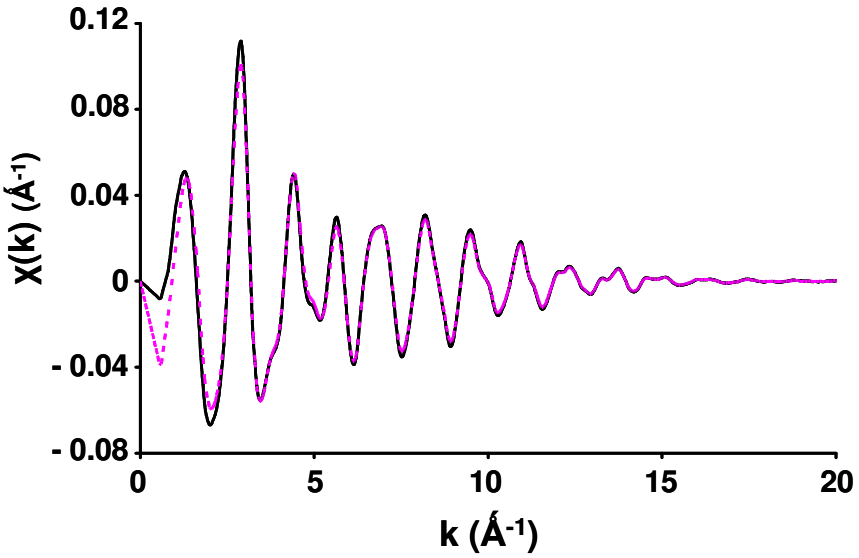

Figure 8: Experimentally $\chi(k)$ EXAFS function of the Ru(3%)/Na-Y sample after NO_x saturation (—) and after regeneration (----) at the Ru K-edge.

The experimentally determined and theoretically calculated k^3 $\chi(k)$ EXAFS function in k space and the Fourier transforms in real space, including the imaginary parts, for the NO_x saturated Ru(3%)/Na-Y sample, measured at the Ru K-edge are shown in Figure 9. The experimentally and calculated $\chi(k)$ EXAFS functions in k space for this NO_x saturated Ru(3%)/Na-Y sample are included in Appendix A.

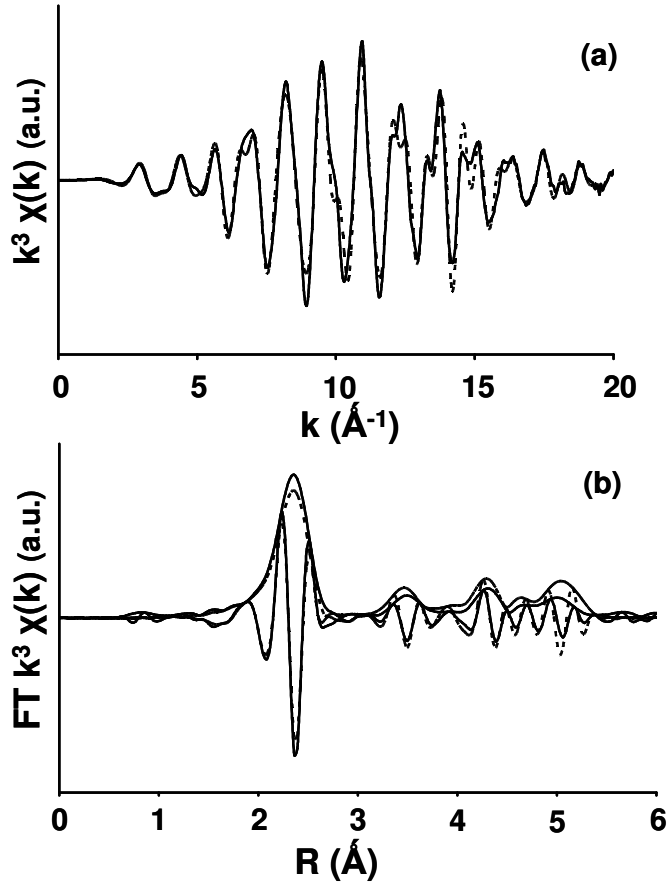

Figure 9: Experimental (—) and calculated (- - -) (a) k^3-weighted EXAFS function and (b) the corresponding Fourier transform plots including the imaginary part of the Ru(3%)/Na-Y sample at the Ru K-edge.

The data quality was excellent, allowing all Ru-Ru metal single shell contribution up to 5 Å, as well as the major multiple scattering contributions, to be included in the fit. Moreover, during the fit only one Debye-Waller factor and one delta R (i.e. difference in distance compared to the model) were fitted to all contributions (in addition to S_0^2 and E_0). This assumes the structure of the Ru particles is identical to the Ru metal, which was confirmed by the goodness of the fit (R = 5%). The corresponding structural parameters can be found in Table 2. The obtained large coordination numbers and multiple shells including multiple scattering present up to at least ~ 6 Å, suggest that the metal particles present at the surface of the zeolite structure are very large. EXAFS did not provide any evidence for the presence of other Ru species next to Ru metal. Considering detection limits of EXAFS, ruthenium species other than ruthenium metal, if present, should represent less than 10% of all ruthenium present.

Table 2: EXAFS fitting parameters at the Ru K-edge for the Ru(3%)/Na-Y sample.

Abs-Sca[1]	CN	R (Å)	$\Delta\ \sigma^2$ (Å^2)
Ru-Ru	6	2.70 ± 0.01	0.005 ± 0.001
Ru-Ru	6	3.78 ± 0.01	0.005 ± 0.001
Ru-Ru	2	4.28 ± 0.01	0.005 ± 0.001
Ru-Ru	12	4.65 ± 0.01	0.005 ± 0.001
Ru-Ru	6	4.68 ± 0.01	0.005 ± 0.001
Ru-Ru	12	5.06 ± 0.01	0.005 ± 0.001
Ru-Ru-Ru	24	4.00 ± 0.01	0.005 ± 0.001
Ru-Ru-Ru	24	5.00 ± 0.01	0.005 ± 0.001
Ru-Ru-Ru	24	5.04 ± 0.01	0.005 ± 0.001
Ru-Ru-Ru	12	5.06 ± 0.01	0.005 ± 0.001

[1]Abbreviations: Abs-Sca: Absorber – Scatterer, CN: coordination number,

R: interatomic distance, $\Delta\sigma^2$: Debye-Waller factor

Fit: R-space, 2.5 Å^{-1} < k < 19.2 Å^{-1} and 1.39 Å < R < 5.83 Å

S_0^2: 0.82 ± 0.05

ΔE_0: -7.0 ± 0.5 eV

R-factor: 0.05

^{99}Ru Mössbauer spectroscopy was run on NO_x saturated Ru(3%)/Na-Y zeolite. The spectrum exhibited a single-line centered at zero velocity (Figure 10), attributed to metallic ruthenium. The line width fit was 0.30 mm/s FWHM. In a non magnetic compound such as Na-Y zeolite, ^{99}Ru Mössbauer spectroscopy fails to discriminate among nano Ru metal particles, if any, from the larger Ru metal particles observed with TEM (Figure 7)

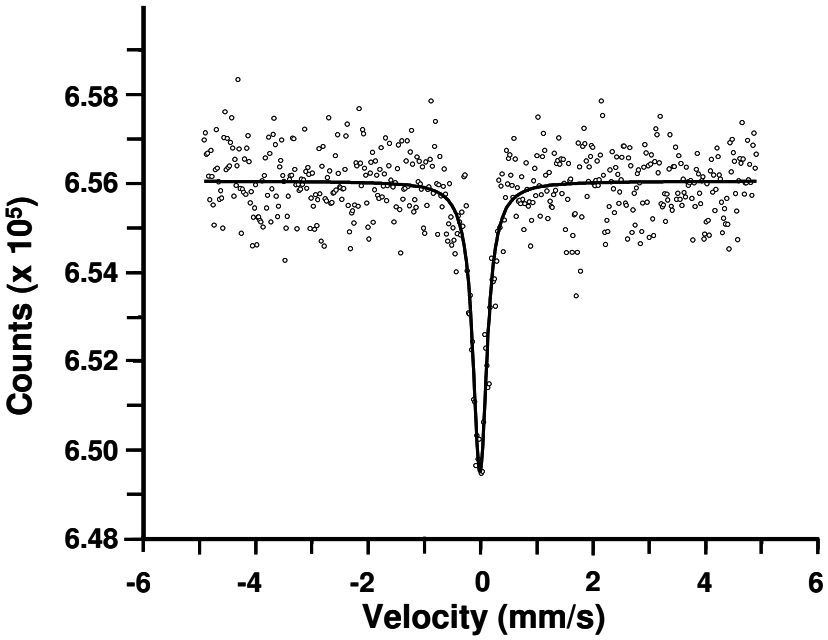

Figure 10: Mössbauer effect plot of the ^{99}Rh(Ru) source versus a ^{101}Ru(3%)/Na-Y zeolite after NO saturation measured at 25 K. The small circles represent the experimental data and the solid line is a single Lorentzian fit to the data.

Ruthenium is known to segregate easily from a faujasite zeolite towards large RuO_2 particles on exposure to oxygen at temperature above 250 °C.[35] These RuO_2 crystallites can be completely reduced to metal particles of comparable size. However this is no longer true for the oxidation of large Ru° particles. These metal particles can no longer be totally re-oxidized at temperatures around 300 °C. Oxygen will only attack the surface layers of the large metal particles to form an ultrathin Ru oxide surface layer covering the metallic core.[36]

In order to reduce the extensive sintering under oxidizing conditions, the pretreatment of the Ru(3%)/Na-Y zeolite was skipped. In the experiment shown in Figure 11, Ru(3%)/Na-Y was heated to 250 °C under a flow of 5% O_2, 3% H_2O and

balance N_2. After reaching temperature, NO_x adsorption-desorption cycles were started. Inlet gas composition during adsorption was 1000 ppm NO, 5% O_2, 3% H_2O and balance N_2. N_2 spiked with 1% H_2, and 3% H_2O was used for desorption.

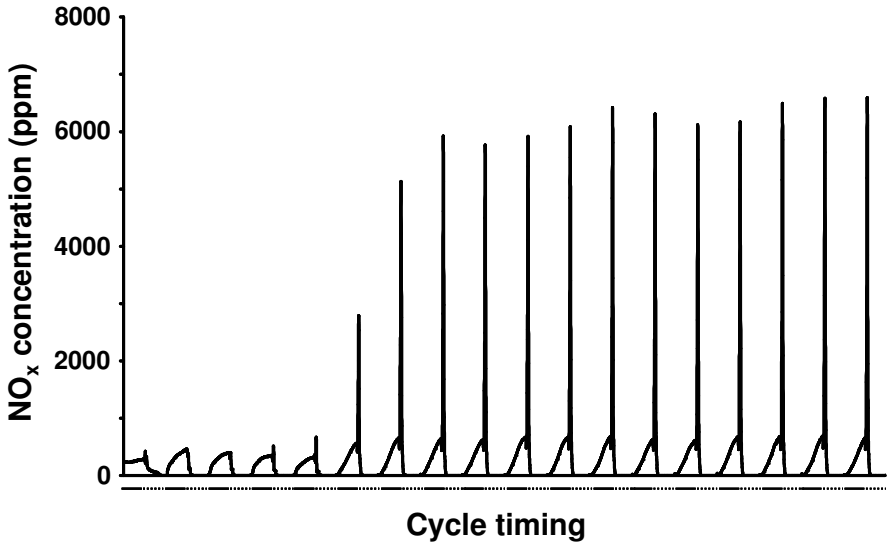

Figure 11: NO_x concentration traces at the adsorber outlet in cycles with 5 min. adsorption (—) and 5 min. desorption (·····) on a Ru(3%)/Na-Y zeolite at 250 °C. The Ru(3%)/Na-Y catalyst was not pretreated but heated to temperature under a flow containing 5% O_2, 3% H_2O and balance N_2. Lean composition was 1000 ppm NO, 5% O_2, 3% H_2O and balance N_2 and regeneration of the adsorbent bed was done with 1% H_2, 3% H_2O and balance N_2.

Without a pretreatment, it took more NO_x adsorption-desorption cycles before a stable and reversible behavior was observed. Although during the first cycles NO uptake was observed, no NO_x was released during regeneration. This can be explained by the presence of the NH_3 ligands of the exchanged Ru atoms. When a pretreatment was done, an amount of NO_x was observed during heating under a flow of 5% O_2, 3% H_2O and balance N_2. This release occured at a temperature around 330-350 °C and could be assigned to reaction (1).[37]

$$4NH_3 + 5O_2 \rightarrow 4NO + 6H_2O \qquad (1)$$

Integration of this NO_x concentration peak led to a Ru/NH_3 ratio of 2. This low value pointed out that there were also probably other reactions like the oxidation to N_2 (Eq.

2), reaction between formed NO_x and NH_3 (Eqs. 3 and 4)[38] and the release of unchanged NH_3 ligands.

$$4NH_3 + 3O_2 \rightarrow 2N_2 + 6\,H_2O \quad (2)$$

$$4NH_3 + 4NO + O_2 \rightarrow 4N_2 + 6H_2O \quad (3)$$

$$4NH_3 + 2NO + 2NO_2 \rightarrow 4N_2 + 6H_2O \quad (4)$$

When no pretreatment was done, these NH_3 ligands were still present and might explain the deceleration of stable and reversible NO_x adsorption-desorption behavior. Because of the considerable NO_x uptake during the first adsorption-desorption cycles, reactions (3) and (4) will probably occur. The absence of a pretreatment had no significant influence on the NO_x adsorption capacity nor on the desorption rate.

Rietveld refinement in combination with analysis of difference electron density charts of the corresponding powder X-ray patterns was done for a freshly Ru ion-exchanged sample and a at 450 °C pretreated Ru(3%)/Na-Y sample (Figure 12). The refinements obtained for both zeolite samples are excellent and are reflected in the Rietveld parameters and the small values of χ^2 (Table 3). The atomic coordinates, occupation parameters, isotropic type and displacements and symmetry multiplicities can be found in Appendix B.

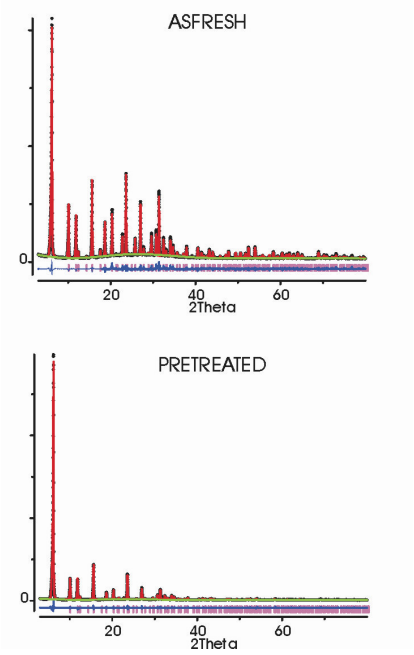

Figure 12: Refined XRD patterns of the Ru(3%)/Na-Y zeolite after Ru ion-exchange and after pretreatment at 450 °C.

Table 3: Rietveld parameters for the refined structures.

Rietveld parameters	Ru(3%)/Na-Y Ion exchanged	Ru(3%)/Na-Y After pretreatment
R_p	0.0488	0.0472
R_{wp}	0.0645	0.0720
R_e	0.0559	0.0434
R_F	0.19703	0.18967
χ^2	1.15	1.67

Rietveld refinement was used to minimize $\sum w_i (I_{0,i} - I_{c,i})^2$ where $I_{0,i}$ and $I_{c,i}$ are the observed and calculated powder diffraction intensities for the i^{th} point respectively. Weights, w_i are $1/ I_{0,i}$. Weighted and unweighted profile R-factors are defined as $R_{wp} = \{[\sum w_i (I_{0,i} - I_{c,i})^2]/[\sum w_i (I_{0,i})^2]\}^{1/2}$ and $R_p = \sum| I_{0,i} - I_{c,i}|/\sum I_{0,i}$. The structure R-factor is defined as $R_F = \sum[(F_0-F_c)^2]/[\sum(F_0)^2]$. The expected R-factor (the statistically best possible value for R_{wp}) is defined as $R_e = [(N-P)/(\sum w_i I_{0,i}^2)]^{1/2}$ where N is the number of observed powder diffraction data points and P is the number of refined parameters. χ^2 was calculated from $(R_{wp}/R_e)^2$

In the freshly Ru ion-exchanged sample, electron density was found on SV in an octahedral environment with bond lengths typically found between Ru^{+3} and NH_3 (Figure 13). Other electron density was found at position SII' in the sodalite cage and SII* and SIII, linked by water molecules in the supercages. After a pretreatment, electron density was found in the hexagonal prism at cation position SI (Figuur 13). The sodalite cages were crowded occupied by cations sitting at position SI'. Other electron density was found at position SII, linked to the 6-ring of the sodalite cage and to one water molecule, resulting in a tetrahedral environment. This indicates that after a pretreatment the NH_3 ligands have disappeared, resulting in a redistribution of the cations in the zeolite.

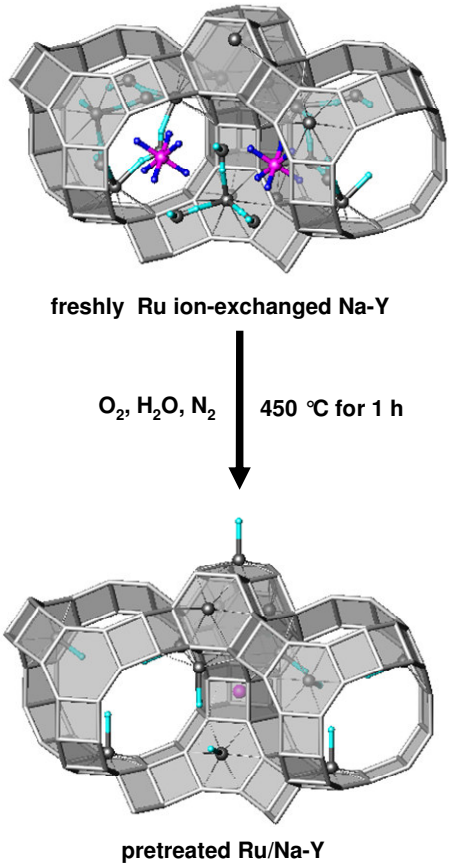

Figure 13: Representation of the cation distribution in a Ru (3%)/Na-Y zeolite after fresh Ru ion-exchange and after pretreatment. The Ru^{+3} cations are represented as the purple spheres and the Na^{+} cations as the grey spheres.

When a pretreatment was done at 250 °C for 1 h, the NO_x adsorption-desorption behavior was obtained gradually as shown in Figure 14. However, the NO_x adsorption capacity after 5 minutes adsorption decreased (2.3 ± 0.1 mg NO_x/g) and the NO_x concentration peak during regeneration was much lower.

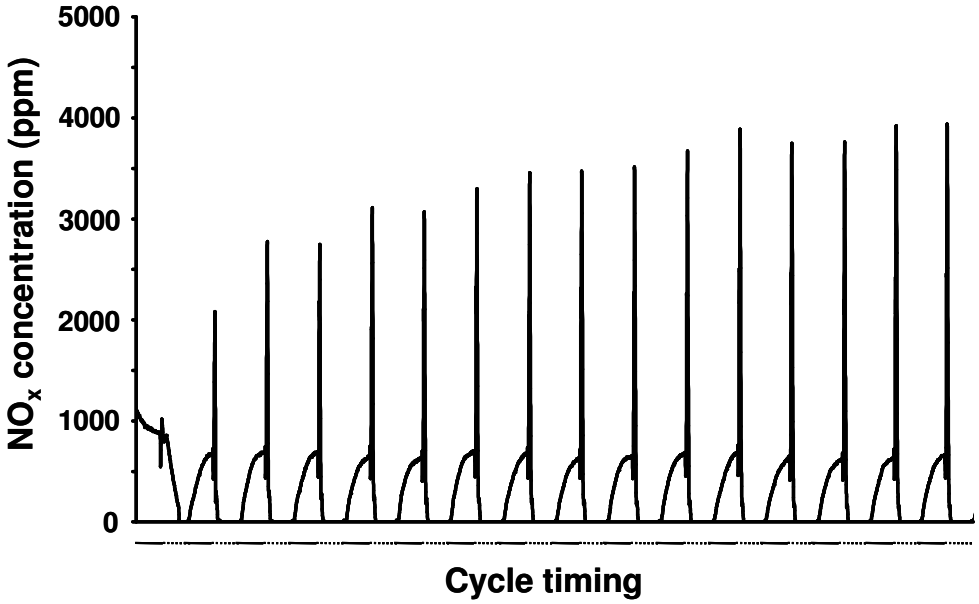

Figure 14: NO_x concentration traces at the adsorber outlet in cycles with 5 minutes adsorption (—) and 5 minutes desorption (·····) on a Ru(3%)/Na-Y zeolite at 250 °C. The Ru(3%)/Na-Y catalyst was first pretreated at 250 °C for 1 h under a flow containing 5% O_2, 3% H_2O and balance N_2. Lean composition was 1000 ppm NO, 5% O_2, 3% H_2O and balance N_2 and regeneration of the adsorbent bed was done with 1% H_2, 3% H_2O and balance N_2.

When a pretreatment was done at 450 °C for 1 h without O_2 in the gas flow, the stable and reversible NO_x adsorption-desorption behavior was obtained already after 1 cycle. However, NO_x adsorption capacity after 5 minutes adsorption was lower (2.2 ± 0.1 mg NO_x/g) compared to the standard pretreatment in presence of O_2 (2.8 ± 0.1 mg NO_x/g). During this pretreatment NH_3 ligands are decomposed into N_2 and H_2, resulting in the auto-reduction of the Ru ions. The exact degree of reduction for this case is not known. The lower NO_x adsorption capacity can be explained by the disturbance of the NO_x adsorption site by Ru metal clusters. Sintering of Ru is less pronounced in the absence of O_2 during pretreatment.

When a NO_x adsorption-desorption experiment was carried out after a pretreatment at 450 °C for 1 h in absence of H_2O, a poor NO_x adsorption-desorption behavior was observed. The presence of water during the pretreatment seems to have an important influence on the final NO_x adsorption-desorption behavior.

Besides the variations in time, temperature and gas flow composition during the pretreatment, the influence of the Ru source on the NO_x adsorption-desorption behavior was evaluated. Instead of $RuCl_3$, Ru-red ($[Ru(NH_3)_5\text{-}O\text{-}Ru(NH_3)_4\text{-}O\text{-}Ru(NH_3)_5]^{+6}$) and $Ru(NH_3)_6Cl_3$ were used. NO_x adsorption-desorption experiments were done after a pretreatment at 450 °C for 1 h in a flow of 5% O_2, 3% H_2O and balance N_2. Lean gas composition was 1000 ppm NO, 5% O_2, 3% H_2O and regeneration was done with 1% H_2, 3% H_2O and balance N_2. This resulted in similar NO_x adsorption-desorption patterns with comparable NO_x adsorption capacities. Therefore, the Ru source has no significant influence on the NO_x adsorption-desorption behavior nor on the NO_x adsorption capacity.

In subsequent experiments the ruthenium loading of Na-Y zeolite was decreased to 2, 1 and 0.5 wt.-%. NO_x adsorption cycles comprising 5 minutes adsorption and 5 minutes desorption were run using the standard gas compositions. NO_x release from all these catalysts with different Ru content was always very quick and achieved within 1 minute. Optimum adsorption temperature and NO_x adsorption capacities were estimated based on an average of 10 stable and reversible NO_x adsorption-desorption cycles. All samples showed an optimum adsorption temperature. On Ru(3%)/Na-Y the optimum temperature was 250 °C increasing gradually to 300 °C with decreasing Ru content to 0.5 wt.-% (Figure 15). Lowering the ruthenium content while increasing the adsorption temperature had a beneficial influence on the average NO_x adsorption capacity (Figure 15).

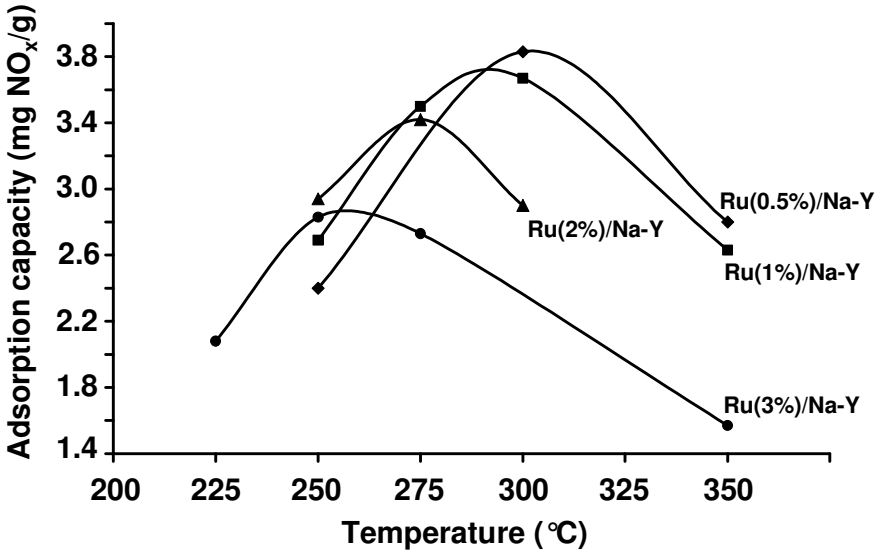

Figure 15: Adsorption capacity versus temperature for Ru/Na-Y catalysts loaded with different wt.-% Ru: ● Ru(3%)/Na-Y, ▲ Ru(2%)/Na-Y, ■ Ru(1%)/Na-Y, ♦ Ru(0.5%)/Na-Y. All the catalysts were pretreated at 450 °C for 1 h in a gasflow containing 5% O_2, 3% H_2O and balance N_2 before adsorption-desorption cycles started. Lean gas composition was 1000 ppm NO, 5% O_2, 3% H_2O and balance N_2. Rich gas composition was 1% H_2, 3% H_2O and balance N_2.

The NO_x adsorption capacity of Ru/Na-Y samples after 5 minutes operation at the optimum temperature decreased with increasing Ru content:
Ru(6%)/Na-Y (2.0 ± 0.1 mg NO_x/g) < Ru(3%)/Na-Y (2.8 ± 0.1 mg NO_x/g) < Ru(2%)/Na-Y (3.4 ± 0.1 mg NO_x/g) < Ru(1%)/Na-Y (3.6 ± 0.1 mg NO_x/g) < Ru(0.5%)/Na-Y (3.8 ± 0.1 mg NO_x/g).

At the beginning of an adsorption phase, some NO breakthrough occurred depending on the Ru content of the Na-Y zeolite. This NO breakthrough was most pronounced on Ru(0.5%)/Na-Y and was absent on Ru(3%)/Na-Y. Apparently at the lowest ruthenium loading, the oxidation function immediately after switching from rich to lean gas was insufficient. Assmann *et al.* assigned the catalytic oxidation activity of supported Ru nanoparticles to the ultrathin Ru oxide surface layer covering the metallic core.[36] Those core-shell RuO_2/Ru particles were reported to be stable under oxidizing conditions below 375 °C. Above 375 °C under oxidation conditions there is a transformation into the less active bulk RuO_2. Provided core-shell RuO_2/Ru

nanoparticles take the role of NO oxidation in Ru/Na-Y adsorbents and after each NO_x desorption in presence of hydrogen the active RuO_2 surface layer needs to be restored for reaching maximum NO oxidation activity. This could explain the observation of NO breakthrough at the beginning of NO_x adsorption observed with Na-Y zeolite samples with critically low amount of Ru particles.

The observation that the NO_x capacity increased with decreasing ruthenium loadings of the zeolite (Figure 15), suggested that NO_x adsorption did not occur on ruthenium and that an excess of ruthenium even eliminated or obstructed access to NO_x adsorption sites. Other evidence for the fact that NO_x adsorption did not occur on ruthenium was provided by NO_x adsorption-desorption experiments on pure RuO_2 powder (99.5+%, anhydrous, Acros). Lean gas composition was 1000 ppm NO, 5% O_2, 3% H_2O and N_2. Regeneration was done with N_2 in presence of 1% H_2 and 3% H_2O. Reaction temperature was 250 °C. During adsorption, RuO_2 was not able to adsorb NO_x and by pass value was reached instantly. During the first NO_x adsorption-desorption cycles, only NO was measured during the adsorption phase. From the 4^{th} cycle, quantitative oxidation to NO_2 was observed. This points out that a couple of reductive cycles are necessary to obtain NO oxidation.

The presence of H_2 was essential for obtaining fast desorption. In an experiment with desorption in the absence of H_2, the regeneration of Ru(3%)/Na-Y lasted more than 10 minutes (Figure 16a). Similar slow desorption kinetics were also observed on NO_x saturated Na-Y zeolite (without Ru-metal loading), using an equimolar mixture of NO and NO_2 (Figure 16b). The NO_x adsorption capacity after 5 minutes operation amounted 2.6 ± 0.1 mg NO_x/g for Na-Y and 2.7 ± 0.1 mg NO_x/g for Ru(3%)/Na-Y. The amount of NO_x released during regeneration was 2.5 ± 0.1 mg NO_x/g in the case of Na-Y and 2.6 ± 0.1 mg NO_x/g for Ru(3%)/Na-Y.

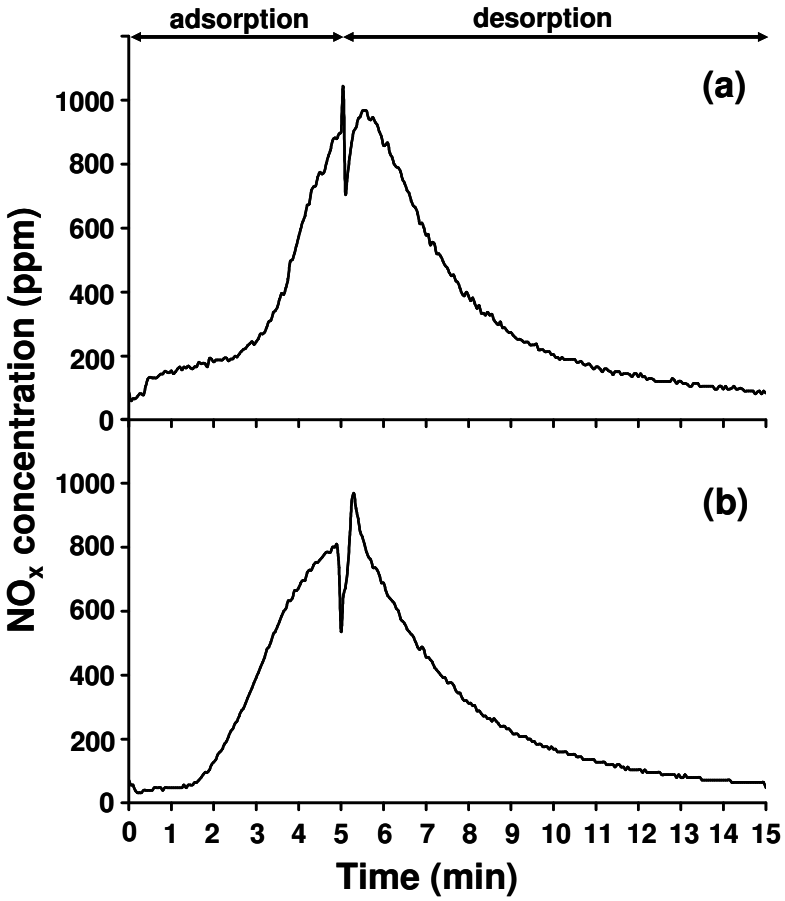

Figure 16: NO_x adsorption-desorption behavior of (a) a Na-Y zeolite and (b) a Ru(3%)/Na-Y zeolite at 250 °C. The Ru(3%)/Na-Y zeolite was first pretreated at 450 °C for 1 h under a gas flow of 5% O_2, 3% H_2O and balance N_2 before adsorption-desorption cycles were started. Lean gas composition was 1000 ppm NO_x (500 ppm NO + 500 ppm NO_2 for Na-Y and 1000 ppm NO for Ru(3%)/Na-Y), 5% O_2, 3% H_2O and balance N_2. Regeneration gas during rich phase was composed as 3% H_2O and balance N_2.

Provided that ruthenium particles loaded on the outside of the zeolite crystals (Figure 7) performed the NO oxidation and NO_x molecules were trapped inside the cavities of the Na-Y zeolite at locations typically distant from Ru, the question remained why the rate of NO_x release was so strongly dependent on the presence of hydrogen (Figure 2 and 16).

To better understand the NO_x adsorption site, Ru(1%)/Na-Y was subjected to NO_x adsorption-desorption cycles at the optimum temperature of 275 °C and investigated using ^{23}Na MAS NMR in NO_x saturated state and after regeneration (Figure 17). The ^{23}Na nucleus possesses a quadrupole moment, which interacts with the electric field gradient at the nuclear site.

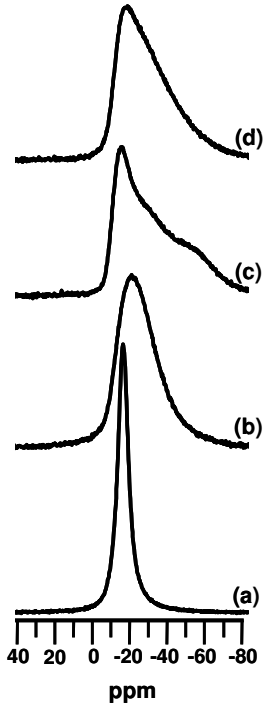

Figure 17: ^{23}Na MAS NMR spectra of a Ru(1%)/Na-Y zeolite after NO_x adsorption-desorption cycles with 1% H_2 during regeneration interrupted after (a) NO_x adsorption and (b) regeneration and after NO_x adsorption-desorption cycles without H_2 during regeneration interrupted after (c) NO_x adsorption and (d) regeneration.

When saturated with NO_x, the ^{23}Na MAS NMR signal consisted of a narrow signal with Gaussian line shape at ca. -16.5 ppm. Such a spectrum is typical for Na^+ cations in a symmetric environment like found in a well hydrated zeolite, where the cations do not directly interact with the framework.[39] In the regenerated sample, the ^{23}Na MAS NMR signal was broadened and extended to more negative chemical shifts (Figure 17). This spectral change implied that some of the Na^+ ions were more shielded and that their environment was less symmetric, like in a situation where Na^+ resides close to the zeolite framework. The ^{23}Na MAS NMR signal of the regenerated sample indeed strongly resembled a typical NMR pattern of partially dehydrated Na-

Y zeolite with Na^+ preferentially occupying sites close to 6-ring windows of the host.[39,40] Ru(1%)/Na-Y samples exposed to NO_x adsorption cycles in absence of hydrogen were also investigated (Figure 17). Different than in presence of hydrogen, the ^{23}Na MAS NMR signal of the NO_x saturated sample showed more asymmetry, typical of a partially hydrated zeolite with framework-sodium interaction. The ^{23}Na MAS NMR spectrum of the regenerated adsorbent hardly changed. Thus ^{23}Na MAS NMR revealed that the use of hydrogen for regeneration had a significant impact on the sodium cation distribution. For comparison, Na-Y zeolite (without ruthenium) was used in adsorption cycles at 250 °C using a gas mixture of N_2 with 500 ppm NO, 500 ppm NO_2, 5% O_2 and 3% H_2O during adsorption, and N_2 with 1% H_2 and 3% H_2O for regeneration (Figure 18).

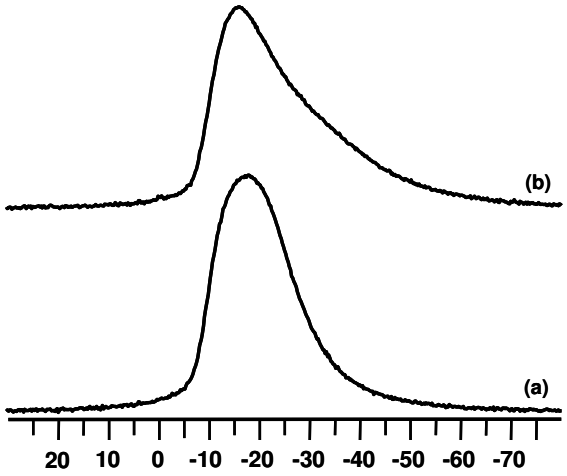

Figure 18: ^{23}Na MAS NMR spectra of a Na-Y zeolite after (a) NO_x saturation and after (b) NO_x release. NO_x adsorption-desorption cycles were done with the standard gas composition and at standard reaction conditions.

The ^{23}Na MAS NMR spectra of Na-Y saturated with NO_x and after regeneration (Figure 18) resembled those of Ru(1%)/Na-Y run in absence of hydrogen (Figure 17). Here too, the sodium ions show similar environments before and after NO_x desorption. The only species in the adsorbent which could be affected by a redox cycle was ruthenium. Therefore, it was concluded that the reduction of ruthenium caused a dramatic change in Na^+ cation environments and that the observed sudden NO_x release was directly linked to this Na^+ cation migration process.

A drastic change of the cation distribution in a known zeolite framework can be studied by Rietveld refinement in combination with analysis of difference electron density charts of the corresponding powder X-ray patterns. For the convenience of the reader the cation positions in FAU zeolite are shown in Figure 19.[41]

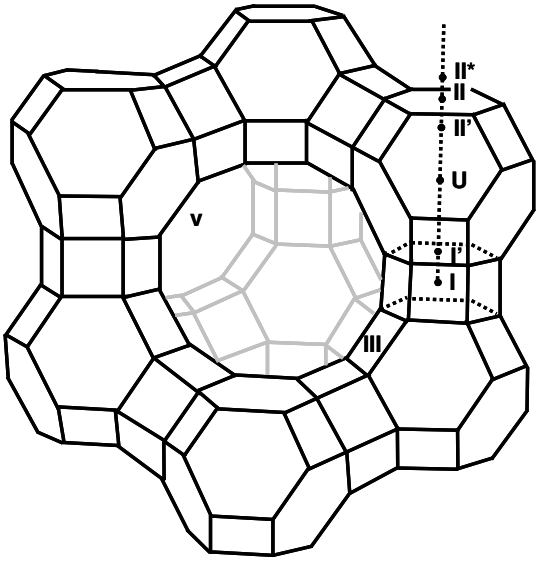

Figure 19: Schematic representation of the cation positions in FAU-type zeolites.[41]

The Ru(1%)/Na-Y adsorbent in different states was investigated. These refined XRD patterns are shown in Figure 20. The refinements obtained for the zeolite samples are excellent and are reflected in the Rietveld parameters and the small values of χ^2 (Table 4). The atomic coordinates, occupation parameters, isotropic type and displacements and symmetry multiplicities can be found in Appendix B.

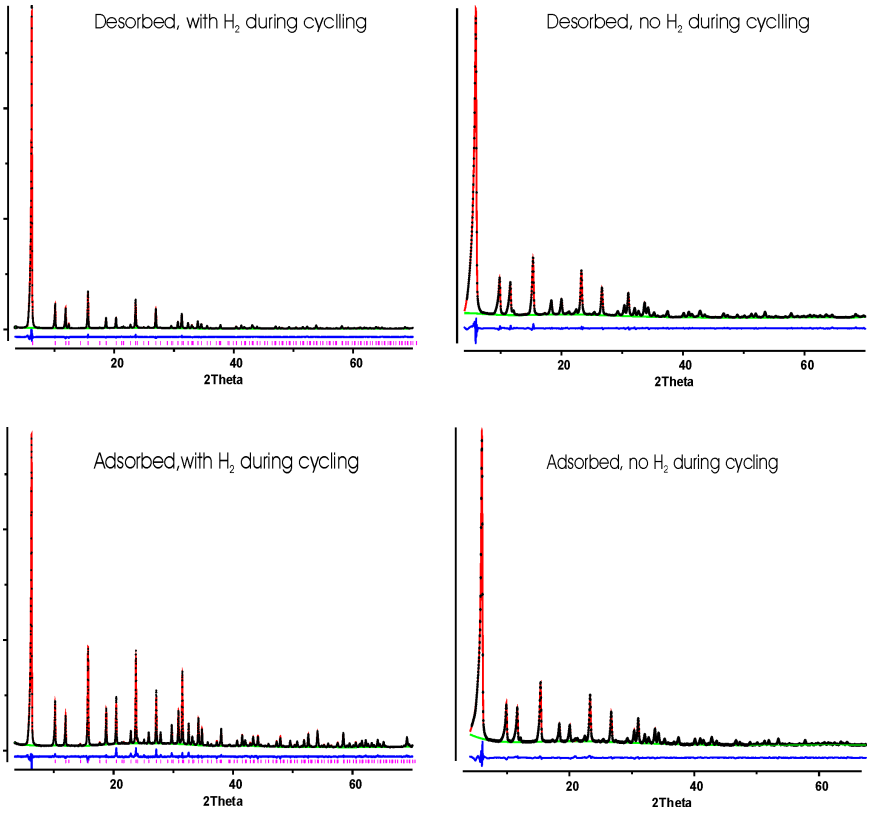

Figure 20: Refined XRD patterns of the Ru(1%)/Na-Y zeolite in different states.

Table 4: Rietveld parameters for the refined structures.

Rietveld parameters	Ru(1%)/Na-Y			
	With H_2 during cycling		No H_2 during cycling	
	NO_x saturated	regenerated	NO_x saturated	regenerated
R_p	0.0397	0.0378	0.0287	0.0285
R_{wp}	0.0522	0.0531	0.0394	0.0387
R_e	0.0512	0.0432	0.0066	0.0066
R_F	0.0655	0.1561	0.1205	0.1113
χ^2	1.03	1.23	6.01	2.91

Rietveld refinement was used to minimize $\sum w_i (I_{0,i} - I_{c,i})^2$ where $I_{0,i}$ and $I_{c,i}$ are the observed and calculated powder diffraction intensities for the i^{th} point respectively. Weights, w_i are $1/ I_{0,i}$. Weighted and unweighted profile R-factors are defined as $R_{wp} = \{[\sum w_i (I_{0,i} - I_{c,i})^2]/[\sum w_i (I_{0,i})^2]\}^{1/2}$ and $R_p = \sum| I_{0,i} - I_{c,i}|/\sum I_{0,i}$. The structure R-factor is defined as $R_F = \sum[(F_0-F_c)^2]/[\sum(F_0)^2]$. The expected R-factor (the statistically best possible value for R_{wp}) is defined as $R_e = [(N-P)/(\sum w_i I_{0,i}^2)]^{1/2}$ where N is the number of observed powder diffraction data points and P is the number of refined parameters. χ^2 was calculated from $(R_{wp}/R_e)^2$

As could be expected from the ^{23}Na MAS NMR experiments, the powder patterns after NO_x adsorption and release in absence of hydrogen very closely resembled each other. Indeed, the patterns could satisfactorily be fitted with the cation-water networks known from Na-Y without Ru. In this structure Na^+ ions on site SIII participate not only in network formation with SV and SII ions but also are in interaction with the zeolite framework which readily explained the asymmetry of the NMR signals. A slight displacement of the Na^+ ions on SIII was observed upon adsorption of NO_x, which caused the more emphasized asymmetry in the ^{23}Na MAS NMR signal in this condition. A representation of the sodium cation distribution in a Ru(1%)/Na-Y zeolite during NO_x adsorption-desorption cycles without using a reducing agent during regeneration is shown in Figure 21.

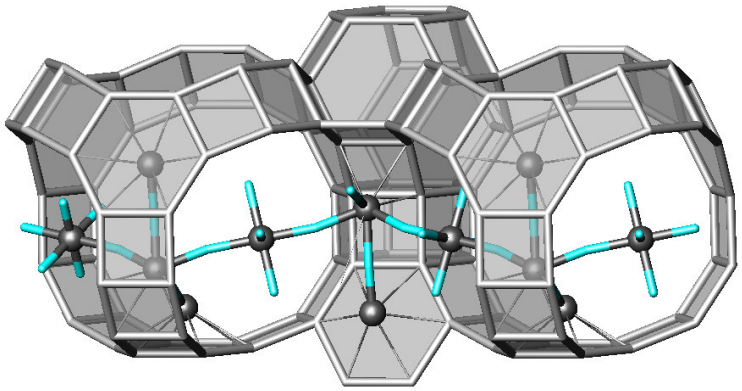

Figure 21: Representation of the sodium cation distribution in a Ru(1%)/Na-Y zeolite during NO_x adsorption-desorption cycles without using a reducing agent during regeneration. A close contact between the framework and Na^+ cations on position SIII is observed.

A very different situation was encountered comparing diffractograms of samples after NO_x saturation and release in presence of hydrogen (Figure 20). A drastic change in the patterns clearly indicated very different cation distributions present in the two states of the adsorbent. In NO_x saturated sample, the supercages contained water networks that link Na^+ cations at position SIII with Na^+ cations at position SV and SII, similar as observed in the Na-Y zeolite[21]. But in this structure, the cations on SIII

were removed exceptionally far from the framework so that almost linear SIII-SV chains with highly symmetric octahedral Na^+ environments were formed. Furthermore, the number of cations participating in this network formation, especially on sites III and V, was considerably higher compared to the situation in absence of hydrogen during cycling (Table 5).

Table 5: Representation of the occupation numbers received after Rietveld refinement of a Ru(1%)/Na-Y zeolite after adsorption-desorption cycles with and without H_2 during regeneration.

atom	site	no H_2 ads/des*	with H_2 des	with H_2 ads
Ru	U	0.0	1.1	0.0
Ru	SI	1.6	0.0	1.3
Na	SII'	0.0	0.0	16.1
Na	SI'	16.1	15.3	15.2
Na	SIII	8.9	3.2	8.6
Na	SV	3.8	2.0	8.6
Na	SII	20.6	28.0	2.0
Na	sum	49.4	48.5	50.4
water		84.6	85.6	83.1

* patterns of ad- and desorbed samples refined with identical occupation numbers

In total about half of the SV and SIII positions were occupied by linked sodium-water octahedra. About the same number of SII* ions was found, which in all probability also interacted with water molecules of the described SIII-SV chains. The refined number of water molecules was in excellent agreement with the thermogravimetrically determined amount of approximately 80 molecules per unit cell. As the maximum loading of the material with NO_x was relatively small (4.8 ± 0.1 mg NO_x/g) corresponding to about two NO_x molecules per unit cell, a free refinement of the position of the NO_x molecules was not feasible. However, inspection of observed and difference electron density suggested a highly probable site for adsorbed

N_2O_3 species located between an SV, SIII and SII Na^+ ion, replacing two water molecules and bridging SV and SIII octahedra. A slight improvement of the quality of refinement indicated this position indeed to be realistic.

In the sodalite cages electron density was found on sites II', I' and also on SI in the hexagonal prisms (Figure 22). Assignment of the type of ion located on these sites was postponed until the system after NO_x desorption was studied in detail. As already indicated by ^{23}Na MAS NMR, the cation distribution after NO_x desorption in presence of hydrogen was drastically changed, whereas it remained almost identical in the sample where no hydrogen was present during desorption (Figure 17). According to Rietveld refinement after reductive desorption, almost no Na^+ ions remained on SV and only very few SIII ions were localized. The approximately 3 SIII cations per unit cell now resided very close to the framework, at positions typical for SIII ions in dehydrated Na-Y frameworks and should give rise to asymmetry in the ^{23}Na MAS NMR signal but the low occupation of this site makes the failure to detect them via NMR plausible. The majority of cations were now found on SII positions close to the six rings of the sodalite cages. Similar as in the sample with adsorbed NO_x, some electron density was found on position SI'. Sites SII' in the sodalite cage and SI in the hexagonal prism were found empty (Figure 22). Instead, a significant electron density was detected in the center of the sodalite cage on site U. This position is not occupied by Na^+ ions as their favorite position always is in the vicinity of six-rings (SII, SII', SI', SII*).

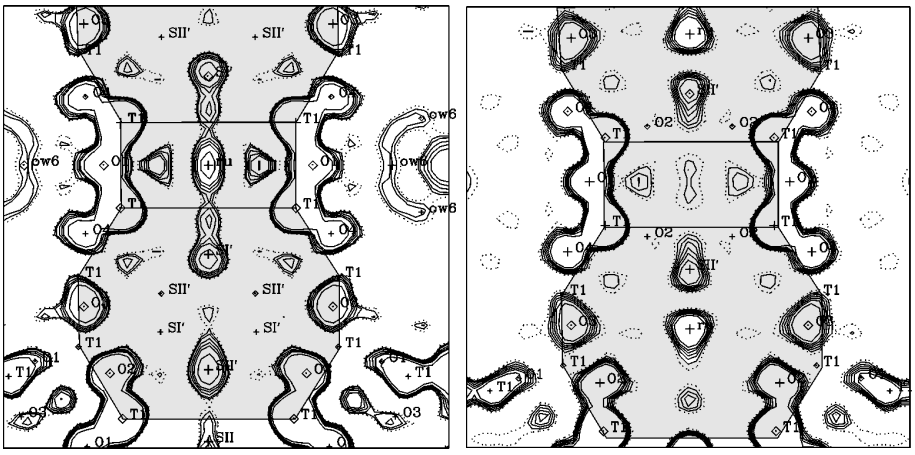

Figure 22: Electron density maps of NO_x saturated (left) and regenerated (right) Ru(1%)Na-Y zeolite. The electron density in the sodalite cage and the hexagonal prism is represented and the cation positions are indicated.

The only candidate for occupation of the SU position is, therefore, a reduced Ru atom. The refined number of Ru atoms on this site of 1.5 atoms per unit cell was in accordance with the chemical composition. With this information, the cation distribution in the sodalite cages of NO_x saturated Ru(1%)/Na-Y zeolite was revisited. No indication for electron density on SU was detected which indicated that after exposure to the oxidizing conditions during NO_x adsorption, the Ru atom changed place, presumably due to oxidation. As possible positions for Ru, now only site SII' and SI in the double six ring were in question as these were found unoccupied after desorption and the occupation number on SI' hardly changed. It turned out the best refinement result and the best match of refined and experimental cation content was achieved if Ru was assumed on site SI inside the hexagonal cavity. Moving the Ru from SU to SI and increasing its charge from 0 to presumably +3 has several significant consequences. This position is in proximity to SIII positions in the supercage so that cations on this side are pushed into the cage, making the adsorbent ready for NO_x adsorption. Furthermore, it can be assumed that in the now empty sodalite cages, Na^+ ions will occupy sites SII' and SI', again in accordance with the observation. An increase of positive charge in the small cavity system apparently causes a general trend for cations in the large cavities to move away from the framework which can explain the extended chain of sodium-water octahedra and the for Na-Y relatively small number of SII* ions. In turn, exposure to reducing conditions will have the opposite effect. A reduction of Ru in the hexagonal cage is impossible because of its large size. So the Ru ion has to migrate to the sodalite cage. The reduction reduces the charge in the small cage system and Na^+ ions now preferably occupy positions close to the framework on SII and SIII. This destroys the adsorption site for N_2O_3 which is released spontaneously rather than in a slow equilibration process when the water chain is retained in absence of reducing conditions.

This scenario implies that Ru not only assumes the role of catalyzing the oxidation of NO to NO_2 on Ru particles, but that mono-atomically dispersed Ru species in the framework cavities take an active role in creating and destroying a suitable adsorption site for N_2O_3. The presence of a bidisperse Ru distribution in Na-Y after redox cycles was already suggested by Verdonck *et al.*[35] However, the fact that this Ru inside the zeolites was not seen by EXAFS nor Mössbauer spectroscopy points out that this fraction indeed is very small. According to Rietveld refinement

and elemental analysis, at most 1-2 Ru atoms are present per 8 sodalite cages. However, as every sodalite cage is in direct contact with 4 of the 8 supercages, this small number of Ru atoms can nonetheless have drastic impact on the cation distribution in the whole unit cell. A schematic representation of the proposed mechanism is shown in Figure 23.

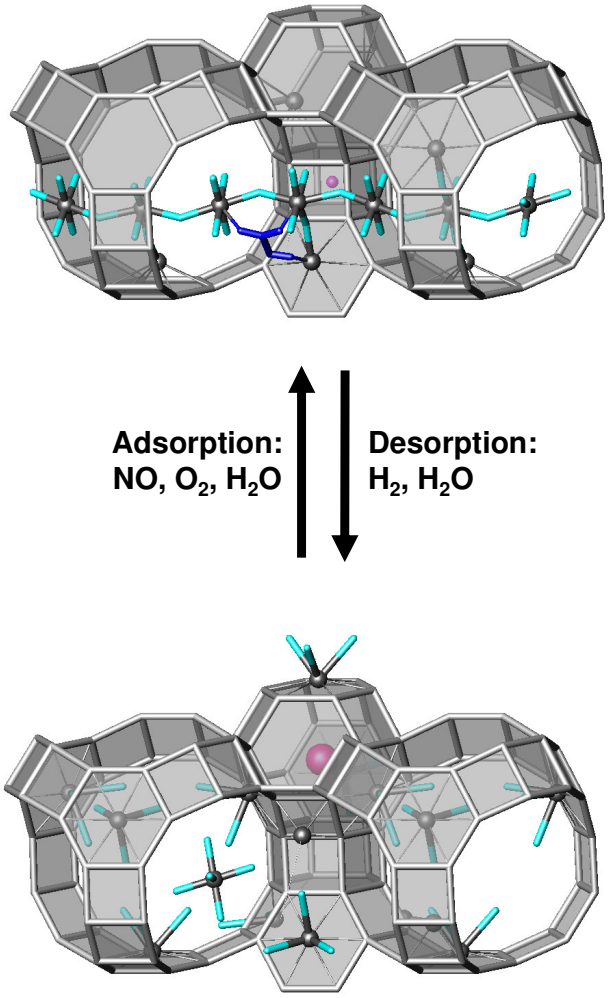

Figure 23: Representation of the cation distribution during NO_x adsorption-desorption in a Ru/Na-Y zeolite during lean/rich cycles based on Rietveld refinement. During lean phase NO_x is adsorbed as N_2O_3 (blue molecule) in the Na-H_2O network in the supercages of the zeolite. The Ru atom, represented as the purple sphere, is situated in the hexagonal prism. During rich phase, the Ru atom is reduced and takes place in the sodalite cage. This migration leads to a redistribution of the Na^+ cations in the supercage, resulting in a fast release of the adsorbed N_2O_3 molecules.

Sulfur poisoning is one of the most important causes leading to deactivation of NO_x adsorbents. In earlier work, Ru(3%)/Na-Y zeolite was evaluated using gases spiked with 50 ppm of SO_2 in the lean or in the rich phase.[42] The catalyst was first pretreated at 450 °C for 1 h under a gas stream of 5% O_2, 12% H_2O and balance N_2. After the pretreatment, the catalyst was cooled to 250 °C and adsorption-desorption cycles started. The lean gas composition was 1000 ppm NO, 5% O_2, 12% H_2O and balance N_2 and rich gas was composed with 1% H_2, 12% H_2O and balance N_2. Over this entire test, the Ru(3%)/Na-Y zeolite was exposed to 270 mg of SO_2/g, which should be sufficient to observe poisoning, if any. The adsorption capacity of Ru(3%)/Na-Y was unaltered in presence of SO_2 (Table 6). The sulfur tolerance previously observed with Na-Y[21-23] was now also observed with Ru/Na-Y.

Table 6: Average NO_x adsorption capacity of Ru(3%)/Na-Y zeolite after 5 minutes adsorption with and without SO_2 in lean or rich phases. The NO_x adsorption capacities were calculated over 10 stable and reversible NO_x cycles.

SO_2 in lean phase (ppm)	SO_2 in rich phase (ppm)	NO adsorption capacity (mg NO_x/g)
0	0	2.60 ± 0.03
0	50	2.70 ± 0.04
50	0	2.50 ± 0.04

During NO and NO_2 co-adsorption on Na-Y zeolite, CO_2 has been shown not to interfere with the N_2O_3 adsorption chemistry.[21] Although the experimental verification has not been made, NO adsorption on Ru/Na-Y zeolite can be expected to be insensitive to CO_2.

The influence of the presence of CO on the NO_x adsorption capacity of a Ru(3%)/Na-Y zeolite was already investigated in earlier work.[42] The amounts of 300 ppm and 3% were added to oxidizing and reducting gases respectively. The results of

that study can now be explained by the NO_x adsorption-desorption mechanism. The presence of CO did not alter the adsorption and fast desorption behavior, but the capacity of the material was affected in a peculiar way. Additions of CO to the rich reductive NO_x desorption had no negative impact on the NO_x capacity, while a noticeable reduction of the adsorption capacity was observed with CO present during the NO_x adsorption phase. This is in excellent support of the refined positions of the Ru species in the zeolite. After NO_x adsorption under oxidizing conditions, the Ru ion resides in the hexagonal prism where CO molecules can not access it. Reduction in the following rich phase can occur as usual; Ru migrates to the sodalite cages, the adsorption site in the large cages is destroyed and NO_x is released. Hence, the presence of CO during desorption does not affect the functioning of the material. However, under oxidizing conditions in the lean phase, Ru now residing in the sodalite cage, should be oxidized and then migrate to the hexagonal prism. But the sodalite cage shares a 6-ring window with the supercages of the zeolite so that interaction with CO could occasionally occur. This interaction now prevents Ru from entering the hexagonal prism, which in turn jeopardizes formation of the water network wherein NO_x can be adsorbed. The presence of CO during the lean oxidizing phase, therefore, drastically reduces the NO_x adsorption capacity of the material. In a practical application, the concentration of CO during lean operation of an engine is, however, expected to be kept as low as possible.

In view of the proposed mechanism (Figure 23) the influence of the Ru loading on the NO_x adsorption cycles (Figure 15) can be revisited. On the sample with lowest Ru content (0.5 wt.-%), the NO oxidation step is limiting, explaining why the temperature needs to be raised to 300 °C for reaching optimum NO_x adsorption capacity (Figure 15). On the sample with high ruthenium loading (3 wt.-%), the NO_x adsorption capacity is more limited because of the disturbance of sodium-water nets in presence of Ru clusters inside the zeolite cavities next to the external surface.

In the here reported NO_x adsorption-desorption cycles, isothermal conditions have been used for practical reasons. A practical NO_x trap can be subjected to important temperature fluctuations. The existence of a temperature optimum (Figure 15) does not necessarily imply that the adsorbent will spontaneously release NO_x upon a temperature excursion away from the optimum. In absence of reducing agent, the NO_x desorption kinetics merely based on competition with water vapor are slow.[21] Heating in presence of a wet NO_x containing gas to temperatures above 450 °C is

needed to evacuate the NO_x, on analogy with the behavior of Na-Y[18]. In practical NO_x traps based on Ru/Na-Y with temperatures fluctuating around the optimum, the NO_x adsorption capacity is expected to correspond to the maximum capacity determined in isothermal experiments. The only way of achieving fast desorption is under reducing gas mixture. NO_x desorption could then effectively be steered by the lean-rich cycle of the engine.

The curious observation that on Ru/Na-Y zeolite several NO_x adsorption cycles are needed before reaching stable behavior can also be explained. On a sample pretreated at 450 °C, bulk RuO_2 is present being an ineffective oxidation function. Several redox cycles are needed to establish the required division of the Na cations in the super- and sodalite cages on the one hand and the Ru over SU/SI sites and extraneous core-shell RuO_x/Ru clusters on the other. Likewise, a Ru(III) ion exchanged Na-Y adsorbent needs a couple of NO_x adsorption cycles before becoming effective.

3.3. Conclusion

In conclusion, Ru loaded Na-Y zeolite is a unique NO_x adsorbent in which NO_x is trapped as N_2O_3 in sodium-water networks extending in the supercages. Oxidation of NO into NO_2 using molecular oxygen is effectively performed at 250 °C by extraneous ruthenium metal particles. The presence of a small amount of Ru atoms corresponding to about one to two atoms per unit cell is crucial for obtaining reversible NO_x adsorption with high efficiency. Oxidized ruthenium atoms are positioned inside hexagonal prisms and push sodium cations into the supercages to generate NO_x adsorption sites. Upon regeneration through reduction, the ruthenium atom jumps to the sodalite cage, causing sodium cations to regain their positions on the framework and eliminating in this way the adsorption site for NO_x. Ru/Na-Y is a unique zeolite adsorbent where relocation of a reducible noble metal atom upon oxidation and reduction governs an adsorption cycle. Practically, the Ru/Na-Y adsorbent may find an application in periodic NO_x recirculation systems[19] or in combination with a downstream SCR catalyst[47].

3.4. References

[1] Gaffney J. S., Marley N. A., *Atmos. Environ.* 43, **2009**, 23-36.

[2] Crutzen P. J., Ramananthan V., *Science* 290, **2000**, 299-304.

[3] Seinfeld J. H., *Science* 243, **1989**, 745-752.

[4] Grosjean D, *Environ. Sci. Technol.* 17, **1983**, 13-19.

[5] Armor J. N., *Appl. Catal. B* 1, **1992**, 221-256.

[6] Kaspar J., Fornasiero P., Hickey N., *Catal. Today* 77, **2003**, 419-449.

[7] Gandhi H. S., Graham G. W., McCabe R. W., *J. Catal* 216, **2003**, 433-442.

[8] Roy S., Baiker A., *Chem. Rev.* 109, **2009**, 4054-4091.

[9] Epling W. S., Campbell L. E., Yezerets A., Currier N. W., Parks II J. E., *Catal. Rev.* 46, **2004**, 163-245.

[10] Sedlmair C., Seshan K., Jentys A., Lercher J. A., *J Catal.* 214, **2003**, 308-316.

[11] Scholz C. M. L., Maes B. H. W., de Croon M. H. J. M., Schouten J. C., *Appl. Catal. A* 332, **2007**, 1-7.

[12] Huang H. Y., Long R. Q., Yang R. T., *Energy Fuels* 15, **2001**, 205-213.

[13] Burch R., Watling T. C., *Appl. Catal. B* 17, **1998**, 131-139.

[14] Sedlmair C., Seshan K., Jentys A., Lercher J. A., *Catal. Today* 75, **2002**, 413-419.

[15] Elbouazzaoui S., Courtois X., Marecot P., Duprez D., *Top. Catal.* 30-31, **2004**, 493-496.

[16] Sedlmair C., Gill B., Seshan K., Jentys A., Lercher J. A., *Phys. Chem. Chem. Phys.* 5, **2003**, 1897-1905.

[17] Bentrup U., Brückner A., Richter M., Fricke R., *Appl. Catal. B* 21, **1999**, 215-220.

[18] Monticelli O., Loenders R., Jacobs P. A., Martens J. A., *Appl. Catal. B* 21, **1999**, 215-220.

[19] Chaize E., Webster D. E., Krutzsch B., Wenninger G., Weibel M., Hodjati Sh., Petit C., Pitchon V., Kiennemann A., Loenders R., Monticelli O., Jacobs P. A., Martens J. A., Kasemo B., *SAE982593*, **1998**.

[20] Hadjivanov K. I., *Catal. Rev. Sci. Eng.* 42 (1&2), **2000**, 71-144.

[21] Sultana A., Loenders R., Monticelli O., Kirschhock C., Jacobs P. A., Martens J. A., *Angew. Chem. Int. Ed.* 39, **2000**, 2934-2937.

[22] Kirschhock C. E. A., Sultana A., Godard E., Martens J. A., *Angew. Chem. Int. Ed.* 43, **2004**, 3722-3724.

[23] Sultana A., Habermacher D. D., Kirschhock C. E. A., Martens J. A., *Appl. Catal. B* 48, **2004**, 65-76.

[24] Brilhac J.-F., Sultana A., Gilot P., Martens J. A., *Environ. Sci. Technol.* 36, **2002**, 1136-1140.

[25] Villani K., Kirschhock C. E. A., Liang D., Van Tendeloo G., Martens J. A., *Angew. Chem. Int. Ed.* 25, **2006**, 3106-3109.

[26] Nijs H., Jacobs P. A., Uytterhoeven J. B., *J. C. S. Chem. Comm.* **1979**, 180.

[27] Verdonck J., Jacobs P. A., Uytterhoeven J. B., *J. C. S. Chem. Comm.* **1979**, 181.

[28] Cisneros M. D., Lunsford J. H., *J. Catal.* 141, **1993**, 191-205.

[29] Mahdi W., Sauerlandt U., Wellenbüscher J., Schütze J., Muhler M., Ertl G., Schlögl R., *Catal. Lett.* 14, **1992**, 339-348.

[30] Assmann J., Narkhede V., Khodeir L., Löffler E., Hinrichsen O., Birkner A., Over H., Muhler M., *J. Phys. Chem. B* 108, **2004**, 14634-14642.

[31] Denayer J. F. M., Depla A., Vermandel W., Gemoets F., van Buren F., Martens J., Kirschhock C., Baron G. V., Jacobs P. A., *Micropor. Mesopor. Mater.* 103, **2007**, 11-19.

[32] Calero S., Dubbeldam D., Krishna R., Smit B., Vlugt T. J. H., Denayer J. F. M., Martens J. A., Maesen T. L., *J. Am. Chem. Soc.* 126, **2004**, 11377-11386.

[33] Maurin G., Plant D. F., Henn F., Bell R. G., *J. Phys. Chem. B* 110, **2006**, 18447-18454.

[34] Uzunova E. L., Mikosch H., Hafner J., *J. Mol. Struct. (Theochem)* 912, **2009**, 88-94.

[35] Verdonck J. J., Jacobs P. A., *J. C. S. Faraday* 76, **1980**, 403-416.

[36] Assmann J., Crihan D., Knap M., Lundgren E., Löffler E., Muhler M., Narkhede V., Over H., Schmid M., Seitsonen A. P., Varga P., *Angew. Chem. Int. Ed.* 44, **2005**, 917-920.

[37] Kröcher O., Devadas M., Elsener M., Wokaun A., Söger N., Pfeifer M., Demel Y., Mussmann L., *Appl. Catal. B* 66, **2006**, 208-216.

[38] Tronconi E., Nova I., Ciardelli C., Chatterjee D., Weibel M., *J. Catal.* 245, **2007**, 1-10.

[39] Hu K.-N., Hwang L.-P., *Solid State Nucl. Magn. Reson.* 12, **1998**, 211-220.

[40] Engelhardt G., Hunger M., Koller H., Weitkamp J, *Studies in Surface Science and Catalysis*, Vol. 84, Weitkamp J., Karge H. G., Pfeifer H., Hölderich W., Eds., Elsevier, Amsterdam, **1994,** 421-428.

[41] Website International Zeolite Association, http://iza-structure.org, March **2010**

[42] Villani K., Development of Catalysts for the abatement of soot and NO_x emissions from Diesel Engines. Doctoraatsproefschrift nr 686, Faculteit Bio-Ingenieurswetenschappen, KUL, **2006**, 126p.

[43] Zukerman R., Vradman L., Herskowitz M., Liverts E., Liverts M., Massner A., Weibel M., Brilhac J. F., Blakeman P. G., Peace L. J., *Chem. Eng. J*. 155, **2009**, 419-426.

CHAPTER 4

4. Reversible NO_x storage over Ru/Ba,Na-Y zeolite

The introduction of ruthenium into Ba,Na-Y zeolite led to a different NO_x adsorption-desorption behavior. Instead of planar nitrate species which could only be removed by heating at high temperature, reversible NO_x adsorption-desorption behavior was observed.

The presence of a Ru phase outside the zeolite caused the equilibration of NO and NO_2 and the presence of some Ru atoms inside the zeolite cavities influenced drastically the occupation of the sodium cation positions in the sodalite and supercages creating thereby adsorption sites for N_2O_3.

Increasing the amount of Ba^{+2} cations in the Ru/Ba,Na-Y zeolite resulted in an increased NO_x adsorption capacity. A reduced number of Na^+ cations led to a severely fragmented Na^+-H_2O network with higher accessibility and presumably higher flexibility increasing significantly the capacity of the adsorbent.

4.1. Introduction

Controlling the exhaust NO_x emission is one of the most challenging aspects for lean-burn engine and diesel technology as the conventional three-way catalyst is not effective in reducing NO_x in a lean exhaust due to the high oxygen level. The most promising approach to the reduction of NO_x under lean-burn conditions is based on the concept of NO_x storage and reduction (NSR).[1,2] Base metal oxide adsorbers like BaO are highly effective for the removal of NO_x from oxygen rich exhaust gas mixtures. The most commonly used formulations includes Pt and BaO supported on a γ-Al_2O_3.[3-6] NO_x is stored as nitrates under lean conditions and regeneration takes place by introduction of a spike of rich gas produced by the engine, as injections of extra fuel cause decomposition of stored NO_x and subsequent reduction into N_2.

Recently, alkali and alkaline earth ion exchanged Y FAU zeolites were reported to have promising activities in the selective catalytic NO_x reduction with hydrocarbons in combination with non-thermal plasma.[7-12] They have a high activity at relatively low temperature (~ 473 K) and are resistant to water vapor.[13] Substitution of Na^+ cations by Ba^{+2} cations markedly increased the NO_x reduction activity of the catalyst.[7,8]

The use of alkali and alkaline earth ion exchanged Y FAU zeolites as NO_x adsorbent in the NO_x storage and reduction concept was studied by Monticelli *et al.*.[14] Alkali and alkaline earth exchanged Y zeolites stored NO_x mainly as nitrate in the temperature window 100-177 °C and in presence of H_2O. The adsorption capacity was dependent on the type of exchanged cation and the zeolite showed no affinity for NO at these temperatures.[14] Ba-Y zeolites have been proven to have high affinity for NO_2.[8,14,13,16]

In this chapter, it is demonstrated how the introduction of reducible Ru^{+3} cations rendered the Ba,Na-Y zeolite a reversible NO_x adsorbent characterized by trapping of pure NO, high NO_x adsorption capacity and with fast desorption kinetics. The presence of a small amount of Ru in a Ba,Na-Y zeolite caused a totally different adsorption mechanism compared to the nitrate formation which was observed in Ba,Na-Y zeolite. Characterization of this Ru/Ba,Na-Y adsorbent was done using ^{23}Na MAS NMR, XRD and Rietveld refinement in combination with analysis of difference electron density charts.

4.2. Results and Discussion

A Ba,Na-Y zeolite, prepared as in Monticelli *et al.*[14] and with unit cell composition $Ba_{17.3}Na_{17.3}Al_{52}Si_{140}O_{384}$, was subjected to a NO_2 adsorption-desorption cycle at 300 °C (Figure 1). Lean gas was composed as 1500 ppm NO_2, 3% H_2O, 5% O_2 and balance N_2. At first, regeneration was done with 3% H_2O in a N_2 stream. After 10 minutes desorption, 1% H_2 was added to the regeneration gas flow.

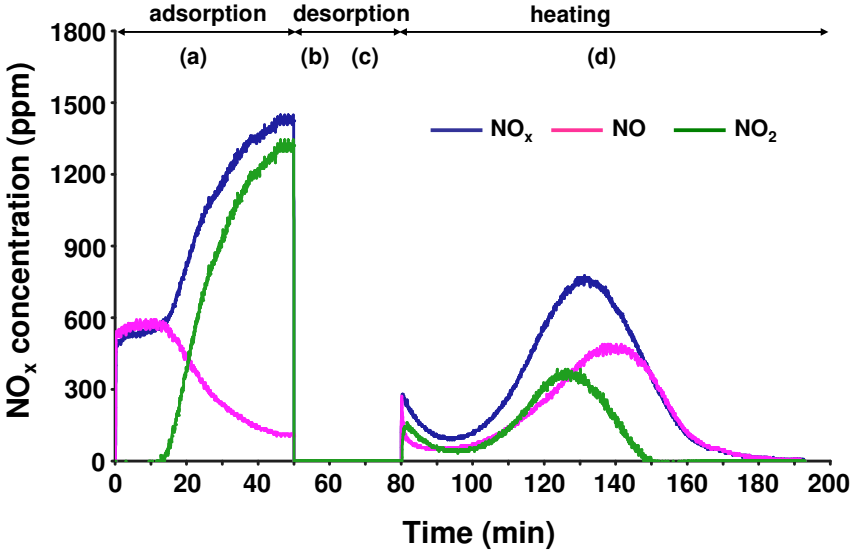

Figure 1: NO_x concentration traces during a NO_x adsorption-desorption cycle of a Ba,Na-Y zeolite at 300 °C. The Ba,Na-Y zeolite was heated to the reaction temperature under a flow of 5% O_2, 3% H_2O and balance N_2. During adsorption (a), gas flow was composed as 1500 ppm NO_2, 5% O_2, 3% H_2O and balance N_2. Desorption of the adsorbent bed was done with 3% H_2O and balance N_2 (b). After 10 min. desorption, 1% H_2 was added to the gas composition (c). After 30 min. desorption, the Ba,Na-Y zeolite was heated under N_2 to 450 °C with a ramp of 5 °C/min (d).

During adsorption, NO_2 uptake together with the release of an amount of NO was observed (Figure 1a). The amount of NO gradually decreased while the NO_2 concentration increased. After 50 minutes of NO_2 adsorption, NO_2 bypass value was reached. During regeneration, no NO_x was released (Figure 1b), even when 1% H_2 was added to the regeneration gas flow (Figure 1c). Only after further heating to 450

°C under a flow of N_2, 20.95 mg NO_x/g of stored NO_x was released from the adsorbent (Figure 1d). The detection of the NO trace during lean phase and the release of NO_x at higher temperatures indicated the formation of nitrates by equation (1):

$$3NO_2 + H_2O \rightarrow 2HNO_3 + NO \qquad (1)$$

The cation distributions and the structures of the nitrate saturated and regenerated Ba,Na-Y zeolite were determined by a combination of Rietveld refinement and difference electron density analysis. The refined XRD patterns are shown in Figure 2 and the corresponding Rietveld refinement parameters can be found in Table 1. In Appendix B, the atomic coordinates, occupation parameters, isotropic type and displacements and symmetry multiplicities are given.

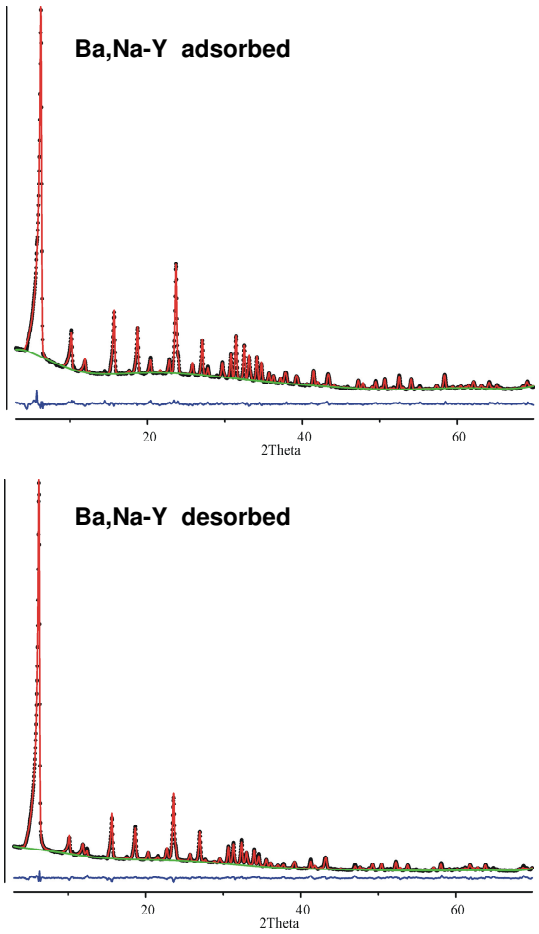

Figure 2: Refined XRD patterns of the Ba,Na-Y zeolite after NO_x saturation and after regeneration.

Table 1: Rietveld parameters of the refined structures.

Rietveld parameters	Ba,Na-Y	
	NO_x saturated	regenerated
R_p	0.0164	0.0179
R_{wp}	0.0214	0.0256
R_e	0.0078	0.0048
R_F	0.0976	0.0942
χ^2	1.75	1.41

Rietveld refinement was used to minimize $\sum w_i (I_{0,i} - I_{c,i})^2$ where $I_{0,i}$ and $I_{c,i}$ are the observed and calculated powder diffraction intensities for the i^{th} point respectively. Weights, w_i are $1/ I_{0,i}$. Weighted and unweighted profile R-factors are defined as $R_{wp} = \{[\sum w_i (I_{0,i} - I_{c,i})^2]/[\sum w_i (I_{0,i})^2]\}^{1/2}$ and $R_p = \sum| I_{0,i} - I_{c,i}|/\sum I_{0,i}$. The structure R-factor is defined as $R_F = \sum[(F_0-F_c)^2]/[\sum(F_0)^2]$. The expected R-factor (the statistically best possible value for R_{wp}) is defined as $R_e = [(N-P)/(\sum w_i I_{0,i}^2)]^{1/2}$ where N is the number of observed powder diffraction data points and P is the number of refined parameters. χ^2 was calculated from $(R_{wp}/R_e)^2$

The Ba^{+2} cations were located on position SI' en SII' in the zeolite blocking access of sodalite cages and SII sites for Na^+ cations. The presence of one Ba^{+2} in each sodalite cage SI' hindered occupation of 3 SII* positions nearby. The still accessible SII* sites were found occupied by the remaining Ba^{+2}. This compelled the Na^+ cations to locate on SIII and SV. Each sodium ion was surrounded by six water molecules resulting in corner sharing sodium-water octahedra. After saturation with NO_x electron density matching planar nitrate species, was found between the Na^+ cations. Their position suggested interaction with the zeolite framework by H-bonds (Figure 3). Interaction with cations and with framework pinpointed this as a very stable location for the nitrate species which could explain why the regeneration of the adsorbent bed only occurred at high temperature.

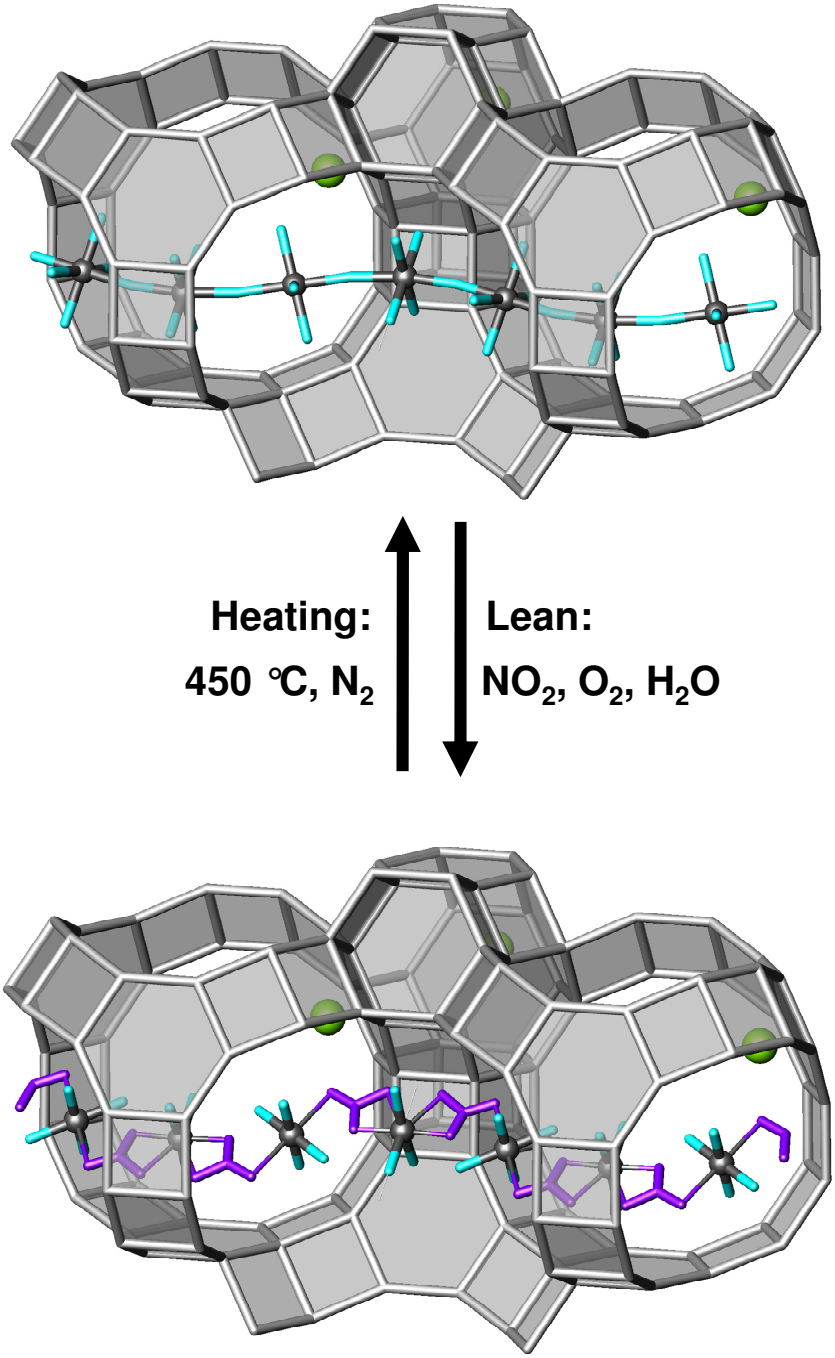

Figure 3: Representation of the nitrate species and the cation distribution in the supercages of a NO_x saturated Ba,Na-Y zeolite. The small grey spheres represent the Na^+ cations; the big green spheres are the Ba^{+2} cations and the planar nitrate species are reproduced by the blue molecules.

Previously it was observed that the presence of Ru in Na-Y zeolite adsorbent led to a fast, reversible adsorption mechanism for NO (Chapter 3). During adsorption-desorption cycles, Ru reversibly changed oxidation state and position, generating and destroying the sodium-water network in the pores which served as N_2O_3 adsorption site. Incorporation of even small amounts of Ru (0.5 wt.-%) into the present Ba,Na-Y zeolite also led to a totally different and especially reversible NO_x adsorption (Figure 4a).

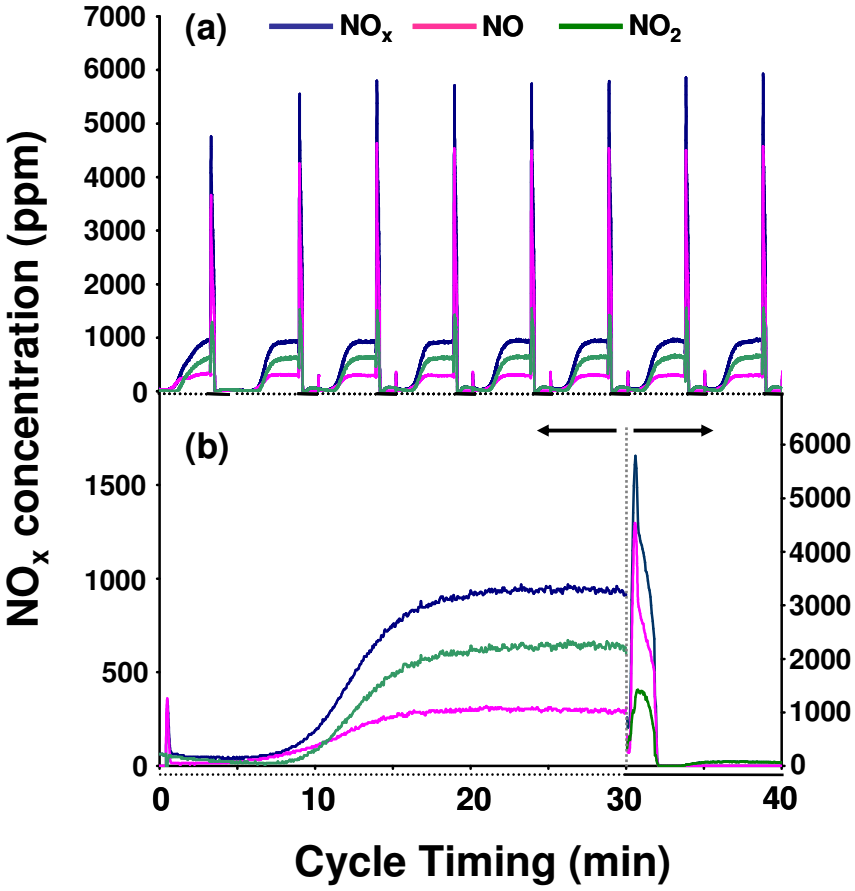

Figure 4: NO_x concentration traces at the adsorber outlet in (a) cycles with 30 min. adsorption (••••) and 10 min. desorption (—) on a Ru(0.5%)/Ba,Na-Y zeolite at 300 °C. A detailed NO_x adsorption-desorption pattern of these cycles is given in (b). Lean gas was composed as 1000 ppm NO, 5% O_2, 3% H_2O and balance N_2. Regeneration of the adsorbent bed was done with 1% H_2, 3% H_2O and balance N_2.

A representative NO_x adsorption-desorption cycle is shown in Figure 4b. A significant NO_x uptake was observed during the first 10 minutes of an adsorption phase.

Saturation was reached after 30 minutes. The main NO_x compound in the adsorber outlet was NO_2, revealing the strong oxidation activity of ruthenium under oxidizing conditions. After switching to reducing conditions, regeneration of the adsorbent bed was complete after 3 minutes. The NO_x adsorption capacity was 10.1 ± 0.3 mg NO_x/g. About half of the adsorbed NO_x was released as NO and NO_2. Formation of negligible amounts of NH_3 and N_2O was detected suggesting that a substantial part of the released NO_x was reduced by hydrogen to N_2. Increasing the Ru content to 1 and 3 wt.-% had no significant influence on the NO_x adsorption-desorption behavior or the NO_x capacity.

Changing the NO_x composition from NO in presence of 5% O_2 to NO_2 in presence of 5% O_2 did not alter the NO_x adsorption-desorption behavior nor the adsorption capacity. The NO/NO_2 ratio during lean phase was in both cases 31/69 indicating that the internal equilibrium was almost established by the ruthenium catalytic function. When H_2O was left out of the gas stream in lean or rich phase, the adsorption behavior disappeared and the NO_x bypass value was reached instantly.

^{23}Na MAS NMR on Ru(3%)/Ba,Na-Y samples saturated with NO_x (Figure 5a) showed a single narrow Gaussian-like line around -22 ppm. After regeneration the signal broadened with a slight shoulder to the right around -24 ppm (Figure 5b).

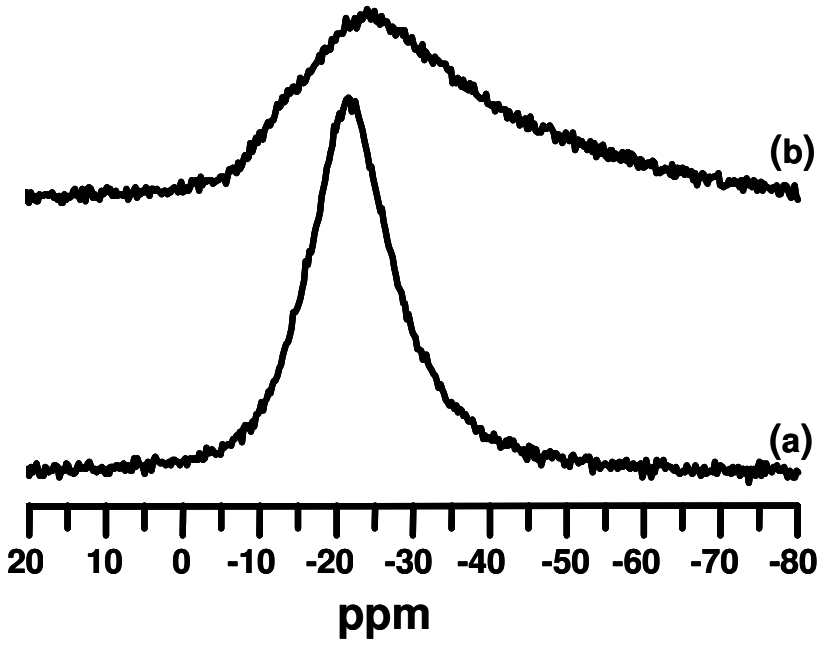

Figure 5: ^{23}Na MAS NMR spectra of a Ru(3%)/Ba,Na-Y zeolite after (a) NO_x adsorption and after (b) regeneration.

Similar spectra were earlier observed with the Ru/Na-Y zeolite. The narrow line observed in the saturated sample corresponded to a symmetric environment of the Na^+ cations like in a well hydrated zeolite, where the cations do not directly interact with the framework.[17] The expression of the shoulder was caused by changed electron density around some Na nuclei after desorption. Such a broadening typically is observed for partially dehydrated Na-Y zeolite with Na^+ preferentially occupying sites close to the framework of the host.[17,18]

Like for analysis of the Ba,Na-Y, Rietveld analysis of powder X-ray diffraction data served to explore the structure of the Ru(0.5%)/Ba,Na-Y. Samples were taken after NO_x saturation and after regeneration at 300 °C. The unit cell composition was determined via ICP-AES and corresponded to $Ru_{0.7}Ba_{17}Na_{15.8}Al_{52}Si_{140}O_{384}$. The refined XRD patterns are shown in Figure 6 and the corresponding R-factors can be found in Table 2. The atomic coordinates, occupation parameters, isotropic type and displacements and symmetry multiplicities are placed in Appendix B.

Table 2: Rietveld parameters for the refined structures.

Rietveld parameters	Ru(0.5%)/Ba,Na-Y 15.8 Na^+/uc	
	NO_x saturated	regenerated
R_p	0.0154	0.0164
R_{wp}	0.0209	0.0229
R_e	0.0049	0.0064
R_F	0.0915	0.0974
χ^2	1.33	1.62

Rietveld refinement was used to minimize $\sum w_i (I_{0,i} - I_{c,i})^2$ where $I_{0,i}$ and $I_{c,i}$ are the observed and calculated powder diffraction intensities for the i^{th} point respectively. Weights, w_i are $1/ I_{0,i}$. Weighted and unweighted profile R-factors are defined as $R_{wp} = \{[\sum w_i (I_{0,i} - I_{c,i})^2]/[\sum w_i (I_{0,i})^2]\}^{1/2}$ and $R_p = \sum| I_{0,i} - I_{c,i}|/\sum I_{0,i}$. The structure R-factor is defined as $R_F = \sum[(F_0-F_c)^2]/[\sum(F_0)^2]$. The expected R-factor (the statistically best possible value for R_{wp}) is defined as $R_e = [(N-P)/(\sum w_i I_{0,i}^2)]^{1/2}$ where N is the number of observed powder diffraction data points and P is the number of refined parameters. χ^2 was calculated from $(R_{wp}/R_e)^2$.

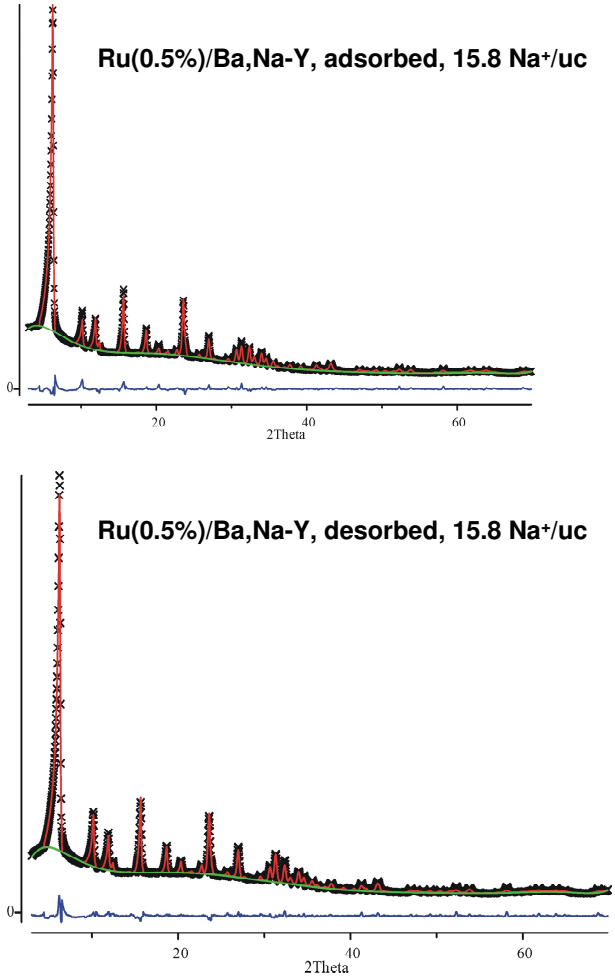

Figure 6: Refined XRD patterns of the Ru(0.5%)/Ba,Na-Y zeolite.

Ba^{+2} cations were found at position SI' and SII* in the sodalite cages during the NO_x adsorption phase. This again forced the Na^+ cations to take positions in the supercages on positions SIII and SV. However, less SI' positions were occupied by Ba^{+2} compared to the Ba,Na-Y zeolite allowing Na^+ cations to occupy also some few SII* positions. This way, construction of a complex H_2O network involving SII*, SIII and SV Na^+ cations in the supercages was possible. The organization of the Na^+ cations and H_2O molecules in the supercages was very similar to what was found in the Na-Y[15] and the Ru/Na-Y zeolites (Chapter 3). However, the SII-SIII-SV clusters with highly symmetric octahedral Na^+ environments were less extended and more strongly branched at the SV cations. Position and occupation of the water positions clearly indicated no extended chains of SIII and SV ions occurred in this sample. Electron density between an SV, SIII and SII Na^+ cation, could be assigned to adsorbed N_2O_3,

replacing H_2O molecules and bridging SV, SIII and SII* octahedra (Figure 7). Similar as in Ru/Na-Y, Ru^{+3} cations were found at position SI in the hexagonal prism. During regeneration the Ru^{+3} cations were reduced to Ru° and moved from cation position SI to cation position SU. This caused the sodium ions on SIII to shift close to the framework, therewith disrupting the H_2O network necessary for NO_x adsorption and causing a rapid release of the adsorbed NO_x.

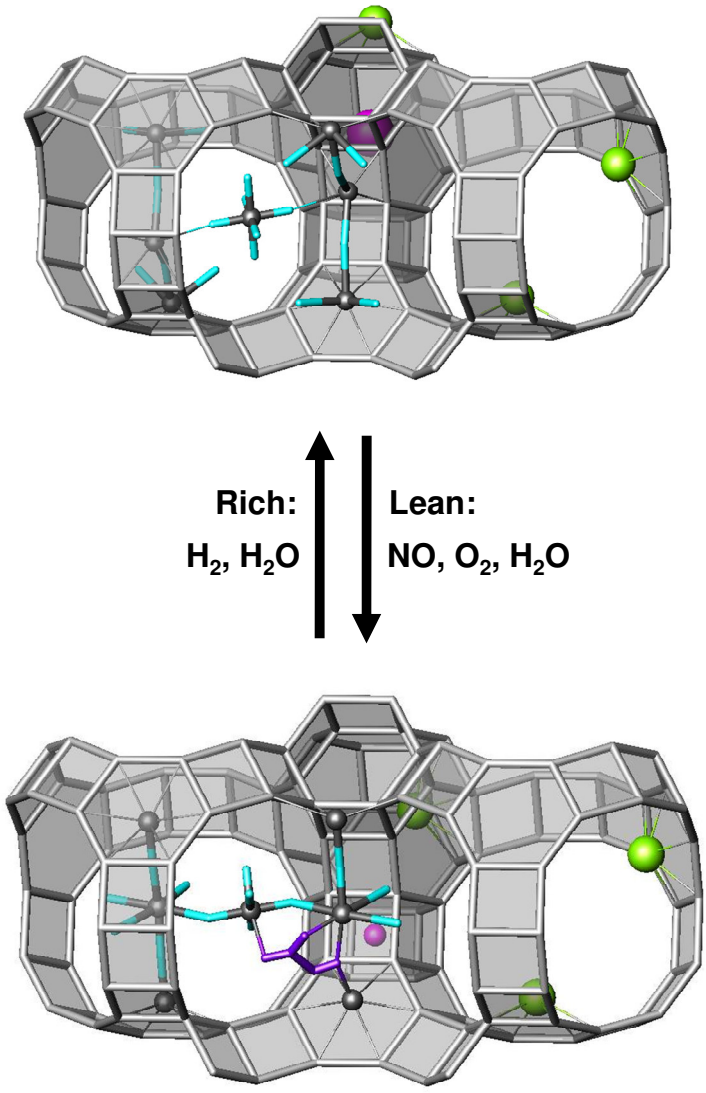

Figure 7: Representation of the cation distribution in a Ru/Ba,Na-Y zeolite (15.8 Na^+ cations per unit cell) during lean-rich NO_x adsorption-desorption cycles based on Rietveld refinement. The Na^+ cations are represented as the grey spheres, the Ba^{+2} cations as the green spheres and the Ru^{+3} atom is shown as the purple sphere. The adsorption of NO_x as N_2O_3 during lean phase is represented as the blue molecule.

To study the effect of the Ba^{+2} concentration in the material, the amount of Ba was increased by an additional ion exchange from 67% to 90% of the CEC. Before the second ion exchange the Ba,Na-Y zeolite was first calcined at 500 °C for 4 h. Elemental analysis resulted in a unit cell composition of $Ba_{23.5}Na_{5.0}Al_{52}Si_{140}O_{384}$. The zeolite was further exchanged with Ru (0.5 wt.-%) resulting in a unit cell composition of $Ru_{0.76}Ba_{22.8}Na_4Al_{52}Si_{140}O_{384}$. As before, NO_x adsorption-desorption cycles were done at 300 °C following the standard procedure. During the first 15 minutes of the adsorption phase, a significant NO_x uptake was observed. Saturation of the adsorbent was reached after 30 minutes and regeneration was complete after 3 minutes. The NO_x adsorption-desorption behavior was similar to Ru(0.5%)/Ba,Na-Y zeolite with lower Ba content. However, the NO_x adsorption capacity was significantly increased to 16.1 ± 0.4 mg NO_x/g. This was rather surprising. A similar NO_x adsorption-desorption behavior pointed at a similar NO_x adsorption mechanism. However, the amount of Na^+ cations in the Ru(0.5%)/Ba,Na-Y zeolite was drastically decreased by the second Ba exchange. It appeared strange such a small amount of Na^+ cations could offer so many NO_x adsorption sites to explain the high capacity.

As before, Rietveld refinement in combination with difference electron density analysis was applied to analyse the structure of the adsorbent and determine the cation distributions. Samples were taken after NO_x saturation and after regeneration at 300 °C. The corresponding refined XRD patterns are shown in Figure 8 and the R-factors are represented in Table 3. The atomic coordinates, occupation parameters, isotropic type and displacements and symmetry multiplicities are placed in Appendix B.

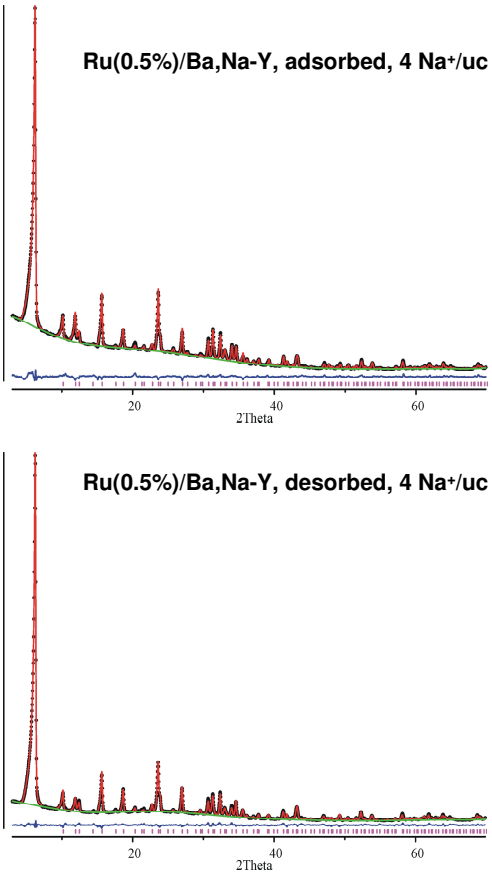

Figure 8: Refined XRD patterns of the Ru(0.5%)/Ba,Na-Y after NO_x saturation and after regeneration.

Table 3: Rietveld parameters for the refined structures.

Rietveld parameters	Ru(0.5%)/Ba,Na-Y 4 Na+/uc	
	NO_x saturated	regenerated
R_p	0.0450	0.0302
R_{wp}	0.0694	0.0410
R_e	0.0370	0.0468
R_F	0.1040	0.0931
χ^2	1.88	0.88

Rietveld refinement was used to minimize $\sum w_i (I_{0,i} - I_{c,i})^2$ where $I_{0,i}$ and $I_{c,i}$ are the observed and calculated powder diffraction intensities for the i^{th} point respectively. Weights, w_i are $1/ I_{0,i}$. Weighted and unweighted profile R-factors are defined as $R_{wp} = \{[\sum w_i (I_{0,i} - I_{c,i})^2]/[\sum w_i (I_{0,i})^2]\}^{1/2}$ and $R_p = \sum| I_{0,i} - I_{c,i}|/\sum I_{0,i}$. The structure R-factor is defined as $R_F = \sum[(F_0-F_c)^2]/[\sum(F_0)^2]$. The expected R-factor (the statistically best possible value for R_{wp}) is defined as $R_e = [(N-P)/(\sum w_i I_{0,i}^2)]^{1/2}$ where N is the number of observed powder diffraction data points and P is the number of refined parameters. χ^2 was calculated from $(R_{wp}/R_e)^2$.

The same positions for Na^+ and Ba^{+2} were found in the structure but massive extra electron density on position SII' was also observed (Figure 9). Assuming this position to be occupied by Ba^{+2}, refinement of the occupation numbers on SII*, SII' and SI' yielded the correct number of Ba^{+2} per unit cell. Refinement of Na^+ occupation on SV and SIII resulted in one and two Na^+, respectively. The occupation of Na^+ on SII* was at first fixed to two Na^+ next to Ba^{+2} and proved stable, later in the refinement. Despite the very low occupation numbers of water, refinement of their position was attempted. The best results were obtained by 3 corner sharing octahedra of Na^+ on SIII-SV-SIII, with each SIII linked to one SII* position each (Figure 9). Compared to the corresponding structure in Na-Y[15] this fragment on the water network appeared more flexible as the octahedra around the SIII ions were no longer fixed by interaction with two SV positions. Introduction of N_2O_3 molecules as rigid bodies into the refinement resulted in a very satisfactory fit of the powder pattern so that the adsorption of 2 N_2O_3 molecules one on each side of the SV ion appeared feasible (Figure 9). This occupation was in full agreement with the measured capacity of the material. It seemed that by heavily fragmenting the sodium water networks their accessibility and affinity for N_2O_3 is increased so that optimum loading of these sites can occur in the twice exchanged framework. A representation of the cation occupation in the Ru/Ba,Na-Y is shown in Figure 9.

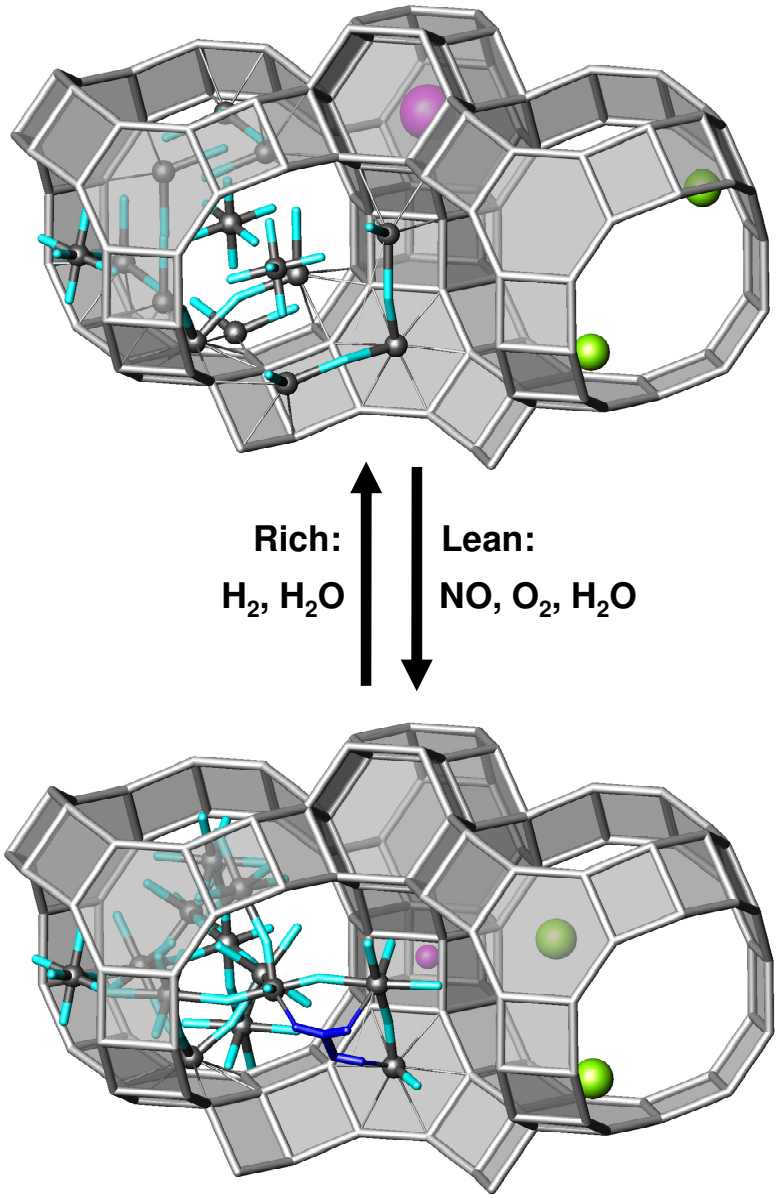

Figure 7: Representation of the cation distribution in a Ru(0.5%)/Ba,Na-Y zeolite (4 Na^+ cations per unit cell) during lean-rich NO adsorption-desorption cycles at 300 °C based on Rietveld refinement. The adsorption of NO_x as N_2O_3 during lean phase is represented as the blue molecule. The Na^+ cations are represented as the grey spheres which coordinate the N_2O_3 molecule. The Ba^{+2} cations are massively found in the sodalite cages. The Ru^{+3} atom is shown as the purple sphere.

4.3. Conclusion

The incorporation of Ru into Ba,Na-Y led to different NO_x adsorption behavior/mechanism compared to the nitrate formation in Ba,Na-Y zeolite. This was caused by the equilibration of NO and NO_2 by the Ru phase outside the zeolite and by Ru in the zeolite which directly influenced occupation of cation positions in the sodalite and the supercages. In absence of Ru, Na^+ cations preferred to take place at position SIII and SV in the supercages of the zeolite. Between these cations, planar nitrate species adsorbed at a stable position. Regeneration of the saturated adsorbent bed only occurred at high temperature. In presence of Ru, some Na^+ cations were able to take place on position SII* besides SIII and SV. This occupation allowed formation of a H_2O network linking the Na^+ cations in the supercages. N_2O_3 molecules could adsorb in this H_2O-Na^+ network competing with the H_2O molecules. The reduction and replacement of Ru during regeneration shuffled the cation positions; Na^+ cations moved closer to the framework giving them a more asymmetric coordination as was seen from the ^{23}Na MAS NMR spectrum of the Ru/Ba,Na-Y zeolite after regeneration. Only a small amount of Ru was required to receive this reversible NO_x adsorption-desorption behavior. Increasing the amount of Ba^{+2} cations in the Ru/Ba,Na-Y zeolite, led also to an increase of the NO_x adsorption capacity. The reduced number of sodium cations led to a severely fragmented Na-H_2O network with higher accessibility and presumably higher flexibility increasing significantly the capacity of the adsorbent. Finally, compared to the maximum NO_x uptake of the Ru(1%)/Na-Y zeolite (4.8 ± 0.1 mg NO_x/g) and single Ba-exchanged Ru(0.5%)/Ba,Na-Y (10.1 ± 0.1 mg NO_x/g) the capacity in the twice exchanged material has tripled (16.1 ± 0.4 mg NO_x/g) while the mechanism still is reversible and release easily could be triggered in reducing conditions.

4.4. References

[1] Roy S., Baiker A., *Chem. Rev.* 109, **2009**, 4054-4091.

[2] Epling W. S., Campbell L. E., Yezerets A., Currier N. W., Parks II J. E., *Catal. Rev.* 46, **2004**, 163-245.

[3] Sedlmair C., Seshan K., Jentys A., Lercher J. A., *J Catal.* 214, **2003**, 308-316.

[4] Mahzoul H., Brilhac J. F., Gilot P., *Appl. Catal. B* 20, **1999**, 47-55.

[5] Lietti L., Forzatti P., Nova I., Tronconi E., *J. Catal.* 204, **2001**, 175-191.

[6] Lesage T., Verrier C., Bazin P., Saussey J., Daturi M., *Phys. Chem. Chem. Phys.* 5 **2003**, 4435-4440.

[7] Kwak J. H., Szanyi J., Peden C. H. F., *Catal. Today* 89, **2004**, 135-141.

[8] Kwak J. H., Szanyi J., Peden C. H. F., *J. Catal.* 220, **2003**, 291-298.

[9] Wen B., Yeom H. H., Weitz E., Sachtler W. M. H., *Appl. Catal. B* 48, **2004**, 125-131.

[10] Yeom Y. H., Wen B., Sachtler W. M. H., Weitz E., *J. Phys. Chem. B* 108, **2004**, 5386-5404.

[11] Sung C.-Y., Broadbelt L. J., Snurr R. Q., *Catal. Today* 136, **2008**, 64-75.

[12] Sung C.-Y., Snurr R. Q., Broadbelt L. J., *J. Phys. Chem. A* 113, **2009**, 6730-6739.

[13] Szanyi J., Kwak J. H., Peden C. H. F., *J. Phys. Chem. B* 108, **2004**, 3746-3753.

[14] Monticelli O., Loenders R., Jacobs P. A., Martens J. A., *Applied Catalysis B* 21, **1999**, 215-220.

[15] Sultana A., Loenders R., Monticelli O., Kirschhock C., Jacobs P. A., Martens J. A, *Angew. Chem. Int. Ed.* 39, **2000**, 2934-2937.

[16] Sedlmair C., Gil B., Seshan K., Jentys A., Lercher J. A., *Phys. Chem. Chem. Phys.* 5, **2003**, 1897-1905.

[17] Hu K.-N., Hwang L.-P., *Solid State Nucl. Magn. Reson.* 12, **1998**, 211-220.

[18] Engelhardt G., Hunger M., Koller H., Weitkamp J., *Studies in Surface Science and Catalysis*, Vol. 84, J. Weitkamp, H. G. Karge, H. Pfeifer, W. Hölderich, Eds.; Elsevier: Amsterdam, 1994, 421-428

GENERAL CONCLUSIONS

NO_x adsorbents are important elements of modern automotive internal combustion aftertreatment. The present generation of NO_x adsorbents are based on barium compounds and are gradually poisoned by SO_x formed from combustion of sulphur containing fuel. Regeneration of sulphur poisoned NO_x traps is technically demanding and is associated by a fuel penalty for generating the rich gas mixture for regeneration.The goal of this work was the development of new zeolite based NO_x adsorbents potentially overcoming this shortcoming of the present generation of NO_x traps.

The starting point of this work was the observation in literature that Na-Y zeolite is sulfur tolerant. Na-Y zeolite exhibits a unique NO_x adsorption-desorption mechanism corresponding to the trapping of N_2O_3 molecules in networks of sodium cations and water molecules extending in the zeolite supercages. Drawbacks of Na-Y zeolite compared to present day NO_x traps are the low NO_x adsorption capacity, slow NO_x desorption kinetics during regeneration and the necessity of having equimolar amounts of NO and NO_2 in the exhaust gas mixture for achieving NO_x adsorption.

As NO is the main NO_x compound of engine exhaust gas, NO_x adsorption on Na-Y is critically dependent on NO into NO_2 oxidation. In a first part of the work, a noble metal was introduced in the Na-Y zeolite as a possible solution for the oxidation of NO. Out of a selection of noble metals, the introduction of ruthenium in the Na-Y zeolite resulted in a remarkable adsorption behavior characterized by trapping of pure

NO from a synthetic exhaust gas mixture and accelerated desorption kinetics. An optimum temperature with respect to the NO_x adsorption capacity of Ru/Na-Y existed in the temperature range of 250-300 °C, depending on the Ru content. By decreasing the ruthenium content, the NO oxidation function became limiting and the temperature needed to be raised for reaching optimum NO_x adsorption capacity. When increasing the ruthenium content, the NO_x adsorption capacity was reduced. This optimum Ru content was tentatively explained by the need of a minimum quantity of ruthenium for catalyzing NO oxidation and an interference of an excess of ruthenium with the networks of sodium cations and water needed for trapping N_2O_3.
The Ru/Na-Y zeolite was characterized using EXAFS, ^{23}Na MAS NMR, ^{99}Ru Mössbauer spectroscopy, TEM, XRD and Rietveld refinement in combination with analysis of difference electron density charts. Ruthenium particles observed using TEM outside of the zeolite crystals were assumed to perform the oxidation of NO into NO_2. A small amount of Ru atoms detected in the zeolite cavities using Rietveld refinement underwent reversible oxidation and reduction during NO_x adsorption-desorption cycles. This redox cycle of Ru atoms had a strong impact on framework charge compensation. It caused a massive migration of sodium cations. During NO_x adsorption, oxidized ruthenium atoms were located inside the hexagonal prisms on position SI, pushing sodium cations into the supercages and generating NO_x adsorption sites in complex sodium-water networks in supercages. During regeneration under reducing conditions, ruthenium migrated to the sodalite cages (position SU), causing sodium cations to regain their positions on oxygen atoms of the framework eliminating in this way the adsorption site for NO_x, resulting in a fast NO_x release. In absence of reducing agent, the NO_x desorption kinetics merely based on competition of N_2O_3 with water molecules for coordination with sodium cations were very slow. The Ru/Na-Y zeolite was found to be sulfur tolerant.

The NO_x adsorption capacity of the Ru/Na-Y zeolite remained rather low compared to current NO_x adsorbents. The exchange of part of the sodium cations with barium resulted in a Ba,Na-Y zeolite with an enhanced adsorption capacity. The Ba,Na-Y zeolite selectively adsorbs NO_2 but is inert to NO. Rietveld refinement of NO_x saturated Ba,Na-Y zeolite revealed the formation of planar nitrate anions bridging sodium cations in the supercages. Regeneration of the Ba,Na-Y zeolite adsorbent bed can only be achieved via decomposition of these nitrates at high temperatures.

Introduction of a small amount of ruthenium in a Ba,Na-Y zeolite altered the adsorption mechanism. Instead of operating via nitrate formation, the Ba,Na-Y zeolite was found to trap N_2O_3 molecules in nets of water molecules linking sodium cations, similar to Na-Y zeolite. A limited number of residual sodium cations in Ru/Ba,Na-Y zeolite is responsible for the NO_x adsorption sites. The highest NO_x adsorption capacity was obtained at 4 Na^+ cations per unit cell. Characterization of this fascinating Ru/Ba,Na-Y adsorbent was done using ^{23}Na MAS NMR, XRD and Rietveld refinement in combination with analysis of difference electron density charts. Similar as in the Ru/Na-Y zeolite, NO_x adsorption occurred as N_2O_3 in the supercages but the reduced number of Na^+ cations led to a severely fragmented Na^+-H_2O network with higher accessibility and presumably higher flexibility increasing significantly the NO_x capacity of the Ru/Ba,Na-Y adsorbent. The NO_x adsorption capacity of Ru/Ba,Na-Y adsorbent is similar to state-of-the-art Ba-based adsorbents.

The new Ru/Na-Y and Ru/Ba,Na-Y zeolite systems developed in this work present because of their unique NO_x adsorption-desorption mechanism a significant innovation in the area of NO_x adsorption technology. The cooperation of reducible and non-reducible cations allowed switching of the cation distribution in the framework cavities. This mechanism reversibly generated and destroyed the adsorption site for NO_x. Fast NO_x desorption can be achieved under reducing conditions. It is expected that using Ru/Ba,Na-Y adsorbent, the regeneration can effectively be steered by lean-rich management of the engine. The concentrated NO_x stream desorbing from the Ru/Ba,Na-Y zeolite trap may find an application in periodic NO_x recirculation systems or in combination with a downstream SCR catalyst. From economical point of view, Ru is one of the cheapest noble metals compared to the commonly used Pd, Ir, Pt and Rh in environmental catalysis.

APPENDIX A

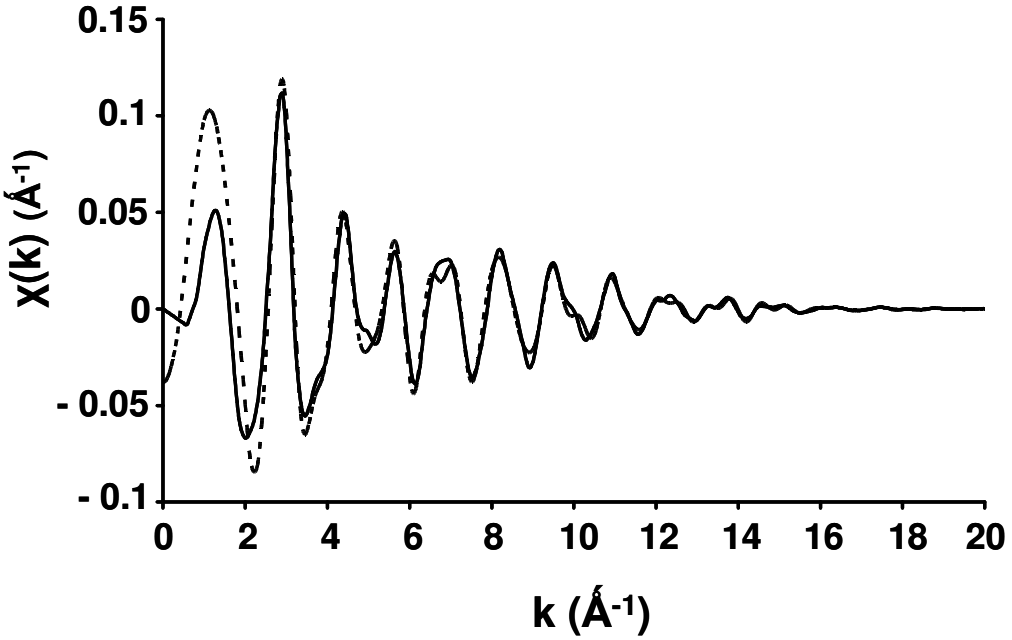

Figure A1: Experimentally (—) and calculated (– – –) $\chi(k)$ EXAFS function of the NO_x saturated Ru(3%)/Na-Y sample at the Ru K-edge.

APPENDIX B

Table B1: Atomic coordinates, occupation parameters, isotropic type and displacements ($Å^2$) and symmetry multiplicity for Ru(3%)/Na-Y zeolite after ion exchange.

Atom		x/a	y/b	z/c	Occupancy	thermal parameter type	u_{iso} or u_{equiv}	symmetry multiplicity
O	O1	0.89175(17)	0.10826(17)	0	1	Uiso	0.0045(24)	96
O	O2	0.96946(20)	0.07997(15)	0.07997(15)	1	Uiso	0.0426(17)	96
O	O3	1.00037(18)	0.14284(21)	1.00037(18)	1	Uiso	0.0102(27)	96
O	O4	0.93064(25)	0.17876(20)	0.07124(20)	1	Uiso	0.0372(32)	96
Si	T1	0.94664(9)	0.12646(9)	0.03651(9)	1	Uiso	0.01776	192
Na	SII'	-0.17581	-0.17581	-0.17581	0.2938(25)	Uiso	0.059(6)	32
Na	SII	0.26162	0.26162	0.26162	0.6083(33)	Uiso	0.295(14)	32
O	ow2	0.3379(5)	0.3379(5)	0.2393(5)	0.6083(33)	Uiso	0.251(13)	96
Na	SIII	0.375	0.375	0.5439(7)	0.6083(33)	Uiso	0.198(10)	48
Ru	Ru15	0.5	0.5	0.5	0.1480(18)	Uiso	0.02854	16
N	NH3	0.5	0.5	0.4086	0.1480(18)	Uiso	0.02792	96

Table B2: Atomic coordinates, occupation parameters, isotropic type and displacements ($Å^2$) and symmetry multiplicity for Ru(3%)/Na-Y zeolite after pretreatment at 450 °C for 1 h under a flow of 5% O_2, 3% H_2O and N_2.

Atom		x/a	y/b	z/c	Occupancy	thermal parameter type	u_{iso} or u_{equiv}	symmetry multiplicity
O	O1	0.89146(32)	0.10854(32)	0	1	Uani	0.0702	96
O	O2	0.9670(4)	0.08008(31)	0.08008(31)	1	Uani	0.01893	96
O	O3	0.99910(28)	0.1468(4)	0.99910(28)	1	Uani	0.05696	96
O	O4	0.92874(32)	0.18016(25)	0.06984(25)	1	Uani	0.00743	96
Si	T1	0.94445(21)	0.12702(18)	0.03481(17)	1	Uani	0.03297	192
Na	SII	-0.2370(4)	-0.2370(4)	-0.2370(4)	0.61689	Uiso	0.025(8)	32
Na	SII*	-0.06774(27)	-0.06774(27)	-0.06774(27)	0.97804	Uiso	0.100(5)	32
O	ow	0.3046(11)	0.3046(11)	0.3046(11)	0.6169	Uiso	0.71(5)	32
Ru	Ru	0	0	0	0.09508	Uiso	0.272(33)	16

Table B3: Atomic coordinates, occupation parameters, isotropic type and displacements ($Å^2$) and symmetry multiplicity for Ru(1%)/Na-Y zeolite after NO_x saturation.

Atom		x/a	y/b	z/c	Occupancy	thermal parameter type	u_{iso} or u_{equiv}	symmetry multiplicity
O	O1	0.89306(1)	0.10694(1)	0	1	Uiso	0.00041	96
O	O2	0.96580(8)	0.07526(4)	0.07526(4)	1	Uiso	0.00041	96
O	O3	0.99598(5)	0.14237(7)	0.99598(5)	1	Uiso	0.00041	96
O	O4	0.92628(8)	0.17841(4)	0.07159(4)	1	Uiso	0.00041	96
Si	T1	0.94578(7)	0.12757(7)	0.03568(7)	1	Uiso	0.00131	192
O	ow1	0.3088(2)	0.3088(2)	0.540(4)	0.17835	Uiso	0.09611	96
Na	SII'	0.17312(3)	0.17312(3)	0.17312(3)	0.50259	Uiso	0.09786	32
Na	SI'	0.07359(3)	0.07359(3)	0.07359(3)	0.47561	Uiso	0.05981	32
Na	SIII	0.375	0.375	0.5098(5)	0.17835	Uiso	0.10225	48
Na	SV	0.5	0.5	0.5	0.53506	Uiso	0.0544	16
Ru	Ru	0	0	0	0.03452	Uiso	0.07575	16
O	ow2	0.3166(8)	0.3166(8)	0.2262(5)	0.1784	Uiso	0.08583	96
N	n1	0.247(9)	0.398(9)	0.454(8)	0.02224	Uiso	0.025	192
N	n2	0.299(10)	0.346(7)	0.437(11)	0.02224	Uiso	0.025	192
N	on1	0.270(6)	0.438(7)	0.456(9)	0.02224	Uiso	0.025	192
N	on2	0.345(7)	0.363(8)	0.432(8)	0.02224	Uiso	0.025	192
N	on3	0.282(8)	0.300(11)	0.432(7)	0.02224	Uiso	0.025	192
O	ow3	0.375	0.375	0.422(4)	0.1784	Uiso	0.09052	48
O	ow4	0.375	0.375	0.6002(3)	0.1784	Uiso	0.09052	48
O	ow5	0.2453(20)	0.2453(20)	0.5903(3)	0.1784	Uiso	0.09052	96
O	ow6	0.4404(22)	0.5596(22)	0.5	0.1784	Uiso	0.09052	96
Na	SII	0.250(4)	0.250(4)	0.250(4)	0.0363	Uiso	0.09	32

Table B4: Atomic coordinates, occupation parameters, isotropic type and displacements ($Å^2$) and symmetry multiplicity for Ru(1%)/Na-Y zeolite after NO_x regeneration.

Atom		x/a	y/b	z/c	Occupancy	thermal parameter type	u_{iso} or u_{equiv}	symmetry multiplicity
O	O1	0.89622(1)	0.10378(1)	0	1	Uiso	0.03077	96
O	O2	0.98130(6)	0.07780(1)	0.07780(1)	1	Uiso	0.01926	96
O	O3	1.00601(3)	0.13223(2)	1.00601(3)	1	Uiso	0.08381	96
O	O4	0.92767(3)	0.17870(1)	0.07130(1)	1	Uiso	0.02119	96
Si	T1	0.94822(7)	0.12365(7)	0.03872(8)	1	Uani	0.03798	192
O	ow1	0.4454(7)	0.4454(7)	0.5377(3)	0.125	Uiso	0.01012	96
Na	SII	0.23215(4)	0.23215(4)	0.23215(4)	0.87573	Uiso	0.0868	32
Na	SI'	0.06887(2)	0.06887(2)	0.06887(2)	0.47947	Uani	0.01129	32
Na	SIII	0.375	0.375	0.6408(2)	0.0657	Uiso	0.01421	48
Na	SV	0.5	0.5	0.5	0.125	Uiso	0.08489	16
Ru	Ru	0.125	0.125	0.125	0.1401	Uani	0.29237	8
O	ow2	0.31340(34)	0.31340(34)	0.2086(4)	0.66	Uiso	0.32924	96
O	ow3	0.2781(1)	0.2781(1)	0.2781(1)	0.21182	Uiso	0.09556	32

Table B5: Atomic coordinates, occupation parameters, isotropic type and displacements ($Å^2$) and symmetry multiplicity for Ru(1%)/Na-Y zeolite after NO_x saturation. No H_2 was used during regeneration.

Atom		x/a	y/b	z/c	Occupancy	thermal parameter type	u_{iso} or u_{equiv}	symmetry multiplicity
O	O1	0.89302(17)	0.10697(17)	0	1	Uiso	0.00136	96
O	O2	0.96632(30)	0.07871(21)	0.07871(21)	1	Uiso	0.00899	96
O	O3	1.00021(19)	0.14201(25)	1.00021(19)	1	Uiso	0.00492	96
O	O4	0.92694(24)	0.17759(20)	0.07241(20)	1	Uiso	0.01353	96
Si	T1	0.94645(12)	0.12571(12)	0.03617(10)	1	Uiso	0.00406	192
Na	SII	0.23502(18)	0.23502(18)	0.23502(18)	0.91422	Uiso	0.00998	32
Na	SI'	0.0637(7)	0.0637(7)	0.0637(7)	0.25603	Uiso	0.09	32
Na	SIII	0.375	0.375	0.2100(29)	0.18484	Uiso	0.17115	48
Na	SV	0.5	0.5	0.5	0.24448	Uiso	0.14537	16
Ru	Ru	0	0	0	0.10726	Uiso	0.07178	16
O	ow1	0.3196(8)	0.3196(8)	0.5207(14)	0.2445	Uiso	0.11001	96
O	ow2	0.3087(20)	0.3087(20)	0.2169(23)	0.3423	Uiso	0.65423	96
O	O14	0.375	0.375	0.6020(31)	0.18547	Uiso	0.14569	48
O	O15	0.375	0.375	0.4635(18)	0.18579	Uiso	0.05784	48
O	O16	0.3011(8)	0.3011(8)	0.3011(8)	0.5535	Uiso	0.25989	32
N	N16	0.2662	0.4	0.42	0.01	Uiso	0.025	192
N	N17	0.3018	0.3476	0.4623	0.01	Uiso	0.025	192
N	on1	0.2939	0.4376	0.4233	0.01	Uiso	0.025	192
N	on2	0.3448	0.3616	0.4817	0.01	Uiso	0.025	192
N	on3	0.2784	0.3045	0.4654	0.01	Uiso	0.025	192

Table B6: Atomic coordinates, occupation parameters, isotropic type and displacements ($Å^2$) and symmetry multiplicity for Ru(1%)/Na-Y zeolite after NO_x regeneration. No H_2 was used during regeneration.

Atom		x/a	y/b	z/c	Occupancy	thermal parameter type	u_{iso} or u_{equiv}	symmetry multiplicity
O	O1	0.89334(17)	0.10666(17)	0	1	Uiso	0.00012	96
O	O2	0.96717(30)	0.07927(20)	0.07927(20)	1	Uiso	0.00979	96
O	O3	0.99998(19)	0.14289(24)	0.99998(19)	1	Uiso	0.00331	96
O	O4	0.92849(24)	0.17741(20)	0.07259(20)	1	Uiso	0.01662	96
Si	T1	0.94662(11)	0.12501(12)	0.03594(9)	1	Uiso	0.00455	192
Na	SII	0.23495(17)	0.23495(17)	0.23495(17)	0.91422	Uiso	0.00319	32
Na	SI'	0.0639(7)	0.0639(7)	0.0639(7)	0.25603	Uiso	0.09	32
Na	SIII	0.375	0.375	0.2101(28)	0.18484	Uiso	0.16343	48
Na	SV	0.5	0.5	0.5	0.24448	Uiso	0.07127	16
Ru	Ru	0	0	0	0.10726	Uiso	0.05609	16
O	ow1	0.3195(9)	0.3195(9)	0.5204(16)	0.2445	Uiso	0.15949	96
O	ow2	0.3087(20)	0.3087(20)	0.2180(24)	0.3423	Uiso	0.69893	96
O	O14	0.375	0.375	0.6020(30)	0.18484	Uiso	0.14854	48
O	O15	0.375	0.375	0.4636(19)	0.18579	Uiso	0.07326	48
O	O16	0.3015(8)	0.3015(8)	0.3015(8)	0.5535	Uiso	0.20908	32

Table B7: Atomic coordinates, occupation parameters, isotropic type and displacements ($Å^2$) and symmetry multiplicity for Ba,Na-Y zeolite after NO_x saturation.

Atom		x/a	y/b	z/c	Occupancy	thermal parameter type	u_{iso} or u_{equiv}	symmetry multiplicity
O	O1	0.89441(25)	0.10559(25)	0	1	Uiso	0.01547	96
O	O2	0.9685(4)	0.07665(28)	0.07665(28)	1	Uiso	0.00278	96
O	O3	0.99736(27)	0.1422(4)	0.99736(27)	1	Uiso	0.01745	96
O	O4	0.9274(4)	0.17722(32)	0.07278(32)	1	Uiso	0.02485	96
Si	T1	0.94731(18)	0.12469(16)	0.03571(19)	1	Uani	0.01485	192
Ba	SII Ba	0.25867(17)	0.25867(17)	0.25867(17)	0.2479	Uiso	0.03402	32
Ba	SI' Ba	0.08135(20)	0.08135(20)	0.08135(20)	0.2501	Uiso	0.04698	32
Na	SIII	0.375	0.375	0.5234(19)	0.166	Uiso	0.0561	48
Na	SV	0.5	0.5	0.5	0.498	Uiso	0.06042	16
O	on1	0.4698(11)	0.4698(11)	0.5930(16)	0.1655	Uiso	0.0932	96
O	on2	0.431(4)	0.431(4)	0.520(5)	0.1655	Uiso	0.0875	96
O	on3	0.407(6)	0.407(6)	0.603(6)	0.1655	Uiso	0.0674	96
N	N	0.4381(16)	0.4381(16)	0.5693(21)	0.1655	Uiso	0.0186	96
O	ow	0.4544(14)	0.4544(14)	0.4544(14)	0.1687	Uiso	0.0286	32
O	ow2	0.4501(11)	0.5499(11)	0.5	0.165	Uiso	0.0527	96
O	ow4	0.375	0.375	0.4371(26)	0.1589	Uiso	0.02573	48
O	ow5	0.4336(13)	0.3164(13)	0.5332(18)	0.164	Uiso	0.0026	96

Table B8: Atomic coordinates, occupation parameters, isotropic type and displacements ($Å^2$) and symmetry multiplicity for Ba,Na-Y zeolite after NO_x regeneration at 450 °C under N_2.

Atom		x/a	y/b	z/c	Occupancy	thermal parameter type	u_{iso} or u_{equiv}	symmetry multiplicity
O	O1	0.8913(5)	0.1087(5)	0	1	Uiso	0.20222	96
O	O2	0.9694(4)	0.07872(28)	0.07872(28)	1	Uiso	0.00344	96
O	O3	0.9953(4)	0.1425(4)	0.9953(4)	1	Uiso	0.0384	96
O	O4	0.9296(5)	0.1765(4)	0.0735(4)	1	Uiso	0.0281	96
Si	T1	0.94924(26)	0.12342(16)	0.03469(23)	1	Uani	0.05572	192
Ba	SII Ba	0.25325(19)	0.25325(19)	0.25325(19)	0.24794	Uiso	0.00275	32
Ba	SI' Ba	0.08801(18)	0.08801(18)	0.08801(18)	0.25103	Uiso	0.01168	32
Na	SIII	0.375	0.375	0.5326(7)	0.1569	Uiso	0.0821	48
Na	SV	0.5	0.5	0.5	0.497	Uiso	0.0512	16
O	ow	0.4386(10)	0.4386(10)	0.5245(18)	0.5	Uiso	0.06056	96
O	ow4	0.375	0.375	0.4375(20)	0.1569	Uiso	0.0761	48
O	ow5	0.4334(12)	0.3166(12)	0.5342(16)	0.1569	Uiso	0.0621	96
O	ow6	0.375	0.375	0.6221(11)	0.1569	Uiso	0.01673	48

Table B9: Atomic coordinates, occupation parameters, isotropic type and displacements ($Å^2$) and symmetry multiplicity for Ru(0.5%)/Ba,Na-Y zeolite after NO_x saturation (15.8 Na^+ cations per unit cell).

Atom		x/a	y/b	z/c	Occupancy	thermal parameter type	u_{iso} or u_{equiv}	symmetry multiplicity
O	O1	0.17251(32)	0.17251(32)	0.9706(5)	1	Uiso	0.0364	96
O	O2	0.1788(4)	0.1788(4)	0.3236(5)	1	Uiso	0.03037	96
O	O3	0.25118(33)	0.25118(33)	0.1419(4)	1	Uiso	0.00919	96
O	O4	0.10530(28)	-0.10530(28)	0	1	Uiso	0.00485	96
Si	T1	0.94548(19)	0.12467(15)	0.03521(21)	1	Uiso	0.00833	192
Ba	SII Ba	0.24514(24)	0.24514(24)	0.24514(24)	0.31	Uiso	0.02387	32
Ba	SI' Ba	0.08052(25)	0.08052(25)	0.08052(25)	0.215	Uiso	0.00438	32
Na	SIII	0.375	0.375	0.5273(2)	0.21738	Uiso	0.06966	48
O	ow	0.375	0.375	0.4354(2)	0.21638	Uiso	0.06291	48
Na	SV	0.5	0.5	0.5	0.20055	Uiso	0.09905	16
Ru	Ru	0	0	0	0.04874	Uiso	0.01002	16
O	ow1	0.3068(1)	0.3068(1)	0.2198(2)	0.217	Uiso	0.05032	96
O	ow3	0.4430(3)	0.4430(3)	0.5337(2)	0.2006	Uiso	0.01961	96
O	ow4	0.375	0.375	0.619(5)	0.21738	Uiso	0.06138	48
Na	SII	0.235(3)	0.235(3)	0.235(3)	0.079	Uiso	0.09812	32
N	n18	0.4885	0.34147	0.46966	0.01	Uiso	0.14524	192
N	n19	0.47164	0.40438	0.43205	0.01	Uiso	0.14524	192
N	n20	0.44823	0.31989	0.47567	0.01	Uiso	0.14524	192
N	n21	0.42417	0.41026	0.42168	0.02	Uiso	0.14524	192
N	n22	0.50981	0.43321	0.42168	0.02	Uiso	0.14524	192

Table B10: Atomic coordinates, occupation parameters, isotropic type and displacements ($Å^2$) and symmetry multiplicity for Ru(0.5%)/Ba,Na-Y zeolite after NO_x regeneration (15.8 Na^+ cations per unit cell).

Atom		x/a	y/b	z/c	Occupancy	thermal parameter type	u_{iso} or u_{equiv}	symmetry multiplicity
O	O1	0.17389(24)	0.17389(24)	0.9679(4)	1	Uiso	0.03149	96
O	O2	0.17927(33)	0.17927(33)	0.3231(4)	1	Uiso	0.01218	96
O	O3	0.25278(28)	0.25278(28)	0.14354(34)	1	Uiso	0.01792	96
O	O4	0.10554(29)	-0.10554(29)	0	1	Uiso	0.01955	96
Si	T1	0.94663(17)	0.12547(16)	0.03624(19)	1	Uiso	0.0024	192
Ba	SII Ba	0.24472(28)	0.24472(28)	0.24472(28)	0.30968	Uiso	0.04191	32
Ba	SI' Ba	0.08465(20)	0.08465(20)	0.08465(20)	0.21772	Uiso	0.02943	32
Na	SIII	0.375	0.375	0.5942(21)	0.2137	Uiso	0.0631	48
O	ow	0.4490(2)	0.4490(2)	0.5318(9)	0.21641	Uiso	0.04896	96
Na	SV	0.5	0.5	0.5	0.0485	Uiso	0.0921	16
Na	SII	0.2394(21)	0.2394(21)	0.2394(21)	0.0712	Uiso	0.0891	32
Ru	Ru12	0.125	0.125	0.125	0.0974	Uiso	0.09398	8
O	ow2	0.3117(2)	0.3117(2)	0.2210(7)	0.09813	Uiso	0.0312	96

Table B11: Atomic coordinates, occupation parameters, isotropic type and displacements ($Å^2$) and symmetry multiplicity for Ru(0.5%)/Ba,Na-Y zeolite after NO_x saturation (4 Na^+ cations per unit cell).

Atom		x/a	y/b	z/c	Occupancy	thermal parameter type	u_{iso} or u_{equiv}	symmetry multiplicity
O	O1	0.1727(7)	0.1727(7)	0.9627(15)	1	Uiso	0.07122	96
O	O2	0.1769(10)	0.1769(10)	0.3383(17)	1	Uiso	0.18932	96
O	O3	0.2508(10)	0.2508(10)	0.1424(11)	1	Uiso	0.05979	96
O	O4	0.1037(7)	-0.1037(7)	0	1	Uiso	0.03773	96
Si	T1	0.9476(5)	0.1273(4)	0.0359(6)	1	Uiso	0.02559	192
Ba	SII Ba	0.2530(6)	0.2530(6)	0.2530(6)	0.2814	Uiso	0.0951	32
Ba	SI' Ba	0.0763(9)	0.0763(9)	0.0763(9)	0.20913	Uiso	0.06644	32
Na	SIII	0.375	0.375	0.48961(16)	0.0408	Uiso	0.0832	48
O	ow	0.4036(7)	0.4036(7)	0.4036(7)	0.063	Uiso	0.078	32
Na	SV	0.5	0.5	0.5	0.0625	Uiso	0.0729	16
O	ow2	0.301(2)	0.199(2)	0.5	0.02063	Uiso	0.03231	96
Ru	Ru	0	0	0	0.09874	Uiso	0.0957	16
O	ow1	0.3103(26)	0.3103(26)	0.245(4)	0.0425	Uiso	0.03269	96
O	ow3	0.4434(3)	0.4434(3)	0.5340(2)	0.042	Uiso	0.019	96
O	ow4	0.426(3)	0.426(3)	0.534(2)	0.041	Uiso	0.019	96
Na	SII	0.239(6)	0.239(6)	0.239(6)	0.0625	Uiso	0.0234	32
N	n18	0.49(12)	0.34(5)	0.47(9)	0.02	Uiso	0.05121	192
N	n19	0.47(6)	0.40(7)	0.43(8)	0.02	Uiso	0.05121	192
N	n20	0.45(9)	0.32(6)	0.48(7)	0.02	Uiso	0.05121	192
N	n21	0.42(8)	0.41(16)	0.42(9)	0.02	Uiso	0.05121	192
N	n22	0.51(6)	0.43(11)	0.42(10)	0.02	Uiso	0.05121	192
Ba	SII' Ba	0.1846(15)	0.1846(15)	0.1846(15)	0.21	Uiso	0.03449	32

Table B12: Atomic coordinates, occupation parameters, isotropic type and displacements ($Å^2$) and symmetry multiplicity for Ru(0.5%)/Ba,Na-Y zeolite after NO_x regeneration (4 Na^+ cations per unit cell).

Atom		x/a	y/b	z/c	Occupancy	thermal parameter type	u_{iso} or u_{equiv}	symmetry multiplicity
O	O1	0.17166(26)	0.17166(26)	0.9705(4)	1	Uiso	0.03595	96
O	O2	0.1762(4)	0.1762(4)	0.3251(5)	1	Uiso	0.04079	96
O	O3	0.25174(22)	0.25174(22)	0.13947(30)	1	Uiso	0.04882	96
O	O4	0.10660(21)	-0.10660(21)	0	1	Uiso	0.05184	96
Si	T1	0.94565(16)	0.12403(13)	0.03456(16)	1	Uiso	0.02424	192
Ba	SII Ba	0.25660(16)	0.25660(16)	0.25660(16)	0.2877	Uiso	0.03615	32
Ba	SI' Ba	0.08005(20)	0.08005(20)	0.08005(20)	0.20899	Uiso	0.03352	32
Na	SIII	0.375	0.375	0.6243(4)	0.0408	Uiso	0.0821	48
Na	SV	0.5	0.5	0.5	0.0625	Uiso	0.09254	16
O	ow2	0.283(3)	0.283(3)	0.424(2)	0.0225	Uiso	0.0731	96
Ru	Ru	0.125	0.125	0.125	0.15783	Uiso	0.01059	8
O	ow1	0.354(2)	0.354(2)	0.272(2)	0.025	Uiso	0.07997	96
O	ow3	0.294(7)	0.206(7)	0.5	0.0206	Uiso	0.0219	96
O	ow4	0.189(8)	0.189(8)	0.432(6)	0.026	Uiso	0.0322	96
Na	SII	0.2377(23)	0.2377(23)	0.2377(23)	0.0625	Uiso	0.0342	32
Ba	SIII Ba	0.18594(34)	0.18594(34)	0.18594(34)	0.21287	Uiso	0.01456	32

LIST OF CHEMICALS, SUPPORT MATERIALS & GASES

Chemicals

$RuCl_3$	99+%, anhydrous	Acros
RuO_2	99.5+%, anhydrous	Acros
$Ru(NH_3)_6Cl_3$	98%	Acros
Ruthenium red	pure	Acros
$Pt(NH_3)_4Cl_2.H_2O$	-	Alfa Aesar
$Pd(NH_3)_4Cl_2.H_2O$	Pd 39% min.	Alfa Aesar
$IrCl_3.H_2O$	99.9%	Alfa Aesar
$Rh(NH_3)_5Cl_3$	34.5% min	Alfa Aesar
Ammonia solution	25% NH_3	Riedel-de Haën
$BaCl_2.2H_2O$	≥ 99+%	Acros
Sdoium Aluminate	54% Al_2O_3	Riedel-de Haën
	41% Na_2O	
Ludox® HS-40	40% SiO_2	Sigma-Aldrich
	60% H_2O	
15-crown-5 ether	98%	Acros
18-crown-6 ether	99%	Acros
NaOH	purum 99%	Riedel-de Haën
Gibbsite	64-66% Al_2O_3	Fluka

Support Materials

Na-Y	Si/Al 2.7	Zeocat
Na-X	Si/Al 1.2	Vetikon
LTL	Si/Al 3	Vetikon
ETS-10	Si/Ti 5	Engelhard

Gases

All gases were supplied by Air Liquide

N_2	N50
O_2	N25
H_2	N30
NO (5% in He)	N30/N45
NO_2 (2% in He)	N20/N50
CO (2.5% in He)	N37/N50
SO_2 (2.5% in He)	N30/N50

LIST OF PUBLICATIONS

Sylvia Smeekens, Steven Heylen, Kenneth Villani, Kristof Houthoofd, Eric Godard, Moniek Tromp, Jin Won Seo, Michaël DeMarco, Christine E. A. Kirschhock, Johan A. Martens, Reversible NO_x storage over Ru/Na-Y zeolite, *Accepted by Chemical Science*, **2010**.

Steven Heylen, Sylvia Smeekens, Christine E. A. Kirschhock, Tatjana Parac-Vogt, Johan A. Martens, Temperature Swing Adsorption of NO_x over Keggin and Wells-Dawson Type Heteropolyacids, *Accepted by Energy Environ. Sci.* ***2010*** *DOI: 10.1039/b923160a*.

Madona Labaki, May Issa, Sylvia Smeekens, Steven Heylen, Christine E. A. Kirschhock, Kenneth Villani, Mejdi Jeguirim, David Habermacher, Jean-Francois Brilhac, Johan A. Martens, Modeling of NO_x adsorption-desorption-reduction cycles on a Ruthenium loaded Na-Y zeolite, *Appl. Catal. B* 97, **2010**, 13-20.